OCS Study
MMS 2009-050

Coastal Marine Institute

Observation of the Deepwater Manifestation of the Loop Current and Loop Current Rings in the Eastern Gulf of Mexico

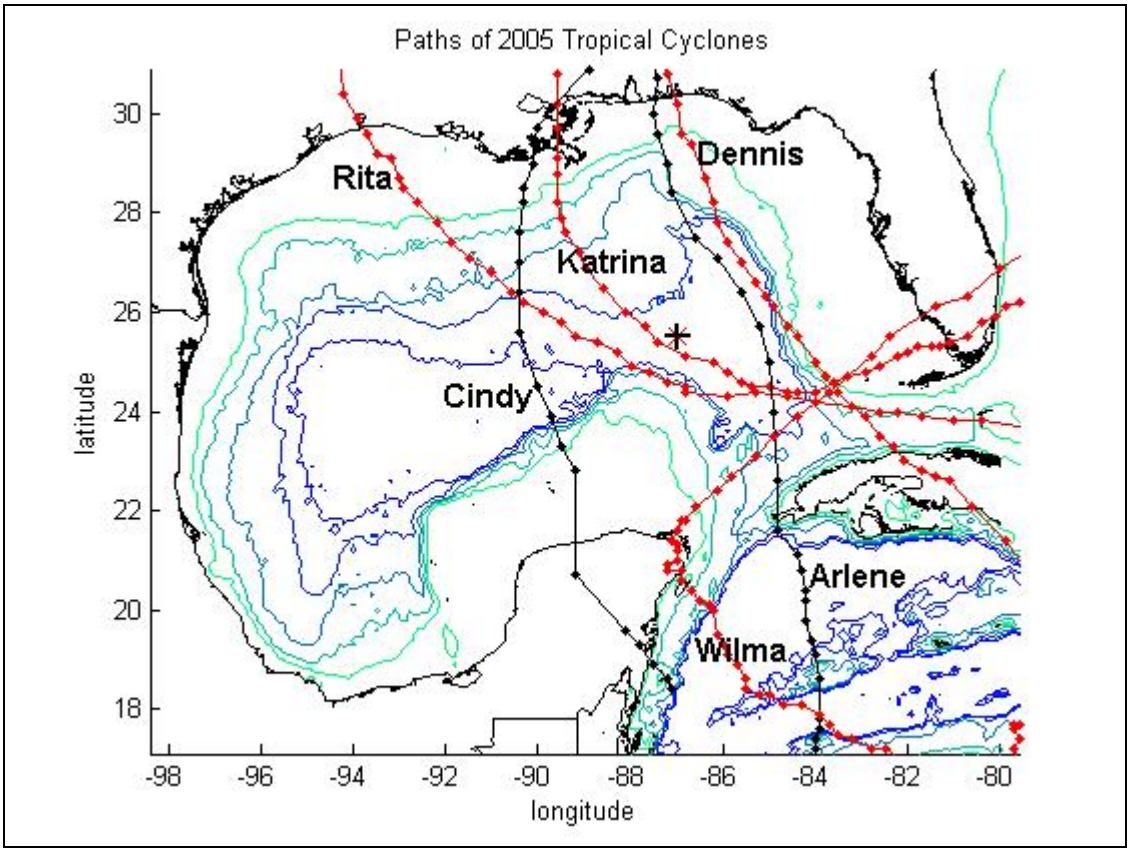

U.S. Department of the Interior
Minerals Management Service
Gulf of Mexico OCS Region

Cooperative Agreement
Coastal Marine Institute
Louisiana State University

OCS Study
MMS 2009-050

Coastal Marine Institute

Observation of the Deepwater Manifestation of the Loop Current and Loop Current Rings in the Eastern Gulf of Mexico

Authors

Susan E. Welsh
Masamichi Inoue
Lawrence J. Rouse, Jr.
Eddie Weeks

October 2009

Prepared under MMS Contract
1435-01-04-CA-32806-36189 (M05AZ10669)
by
Louisiana State University
Coastal Marine Institute
Baton Rouge, Louisiana 70803

Published by

U.S. Department of the Interior
Minerals Management Service
Gulf of Mexico OCS Region

Cooperative Agreement
Coastal Marine Institute
Louisiana State University

DISCLAIMER

This report was prepared under contract between the Minerals Management Service (MMS) and Louisiana State University (LSU). This report has been technically reviewed by the MMS, and it has been approved for publication. Approval does not signify that the contents necessarily reflect the view and policies of the MMS, nor does mention of trade names or commercial products constitute endorsement or recommendation for use. It is, however, exempt from review and compliance with the MMS editorial standards.

REPORT AVAILABILITY

This report is available only in compact disc format from the Minerals Management Service, Gulf of Mexico OCS Region, at a charge of $15.00, by referencing OCS Study MMS 2009-050. The report may be downloaded from the MMS website through the Environmental Studies Program Information System (ESPIS). You will be able to obtain this report also from the National Technical Information Service in the near future. Here are the addresses. You may also inspect copies at selected Federal Depository Libraries.

Minerals Management Service
Gulf of Mexico OCS Region
Public Information Office (MS 5034)
1201 Elmwood Park Boulevard
New Orleans, Louisiana 70123-2394
Telephone requests may be placed at
(504) 736-2519, 1-800-200-GULF, or
Rush Orders: 1-800-553-6847
Fax: (504) 736-2620

U.S. Department of Commerce
National Technical Information Service
5285 Port Royal Road
Springfield, Virginia 22161
Phone: (703) 605-6040
Fax: (703) 605-6900
Email: bookstore@ntis.gov

CITATION

S.E. Welsh, M. Inoue, L.J. Rouse, Jr., and E. Weeks. 2009. Observation of the deepwater manifestation of the Loop Current and Loop Current rings in the Eastern Gulf of Mexico. U.S. Dept. of the Interior, Minerals Management Service, Gulf of Mexico OCS Region, New Orleans, LA. OCS Study MMS 2009-050. 110 pp.

ABSTRACT

Following the previous successful observations involving three deployments covering the periods June 2000 – June 2002 and April 2003 – June 2004, two additional years of deployment of a deep water mooring at the center of the eastern Gulf of Mexico produced additional observations of deep water manifestations of the Loop Current and Loop Current rings. These deployments placed an emphasis on observing the interface between the upper- and lower-layers and variability of water mass properties in deep water. The interface between the upper and lower layers appears to be located close to the sill depth (~800 m) at Strait of Florida. In the modeling component of this project, very high horizontal (.075º) and vertical (100 levels) resolution allowed more realistic representation of the bottom topography including the gentle rise and the steep escarpments. Consequently, it resulted in more realistic simulation of deep water currents in the eastern Gulf of Mexico, i.e., more energetic deep water and more chaotic eddy field in deep water, consistent with the observations at the mooring site. It appears that the Loop Current and Loop Current rings drive deep water currents in the eastern Gulf of Mexico. A modon pair forms underneath the Loop Current when the Loop Current extends northward prior to the formation of a Loop Current ring. However, deep water eddy-eddy and eddy-topography interaction due to the topographic constriction in the central gulf and the limited size of the eastern basin make clear identification of "a modon pair" problematic. The observations of currents and water mass characteristics at the mooring site appear to be consistent with the Cushman-Roisin et al. (1990) mechanism for the generation of the deep anticyclone-cyclone pair beneath the Loop Current. Another mechanism to transmit significant energy to deep water in the Gulf of Mexico is the barotropic oceanic response to the elevated sea surface near the center of tropical and extra-tropical storms often observed in the Gulf of Mexico. Due to frequent occurrences of these storms within the Gulf of Mexico, this could represent another important forcing mechanism to transmit significant energy to deep water in the Gulf of Mexico, thus contributing to deep water energetics and its well-mixed deep water conditions below the Yucatan sill depths.

TABLE OF CONTENTS

LIST OF FIGURES

LIST OF FIGURES
(continued)

LIST OF FIGURES
(continued)

Page

LIST OF FIGURES
(continued)

Page

LIST OF FIGURES
(continued)

Page

LIST OF FIGURES
(continued)

Page

LIST OF TABLES

Page

ACKNOWLEDGMENTS

We would like to acknowledge the essential role of the Coastal Marine Institute at Louisiana State University which is funded by the Minerals Management Service and the LSU Office of Research and Economic Development and who provided the necessary funding for this project. This project, unprecedented in its objective and scope, would not have been possible without the funding provided by the Minerals Management Services and the continuing support and encouragement provided by the contracting officer's technical representative, Dr. Alexis Lugo-Fernandez. As a result, we were able to observe for the first time deepwater currents at the middle of the eastern Gulf of Mexico underneath the Loop Current for a total of five yearly deployments. We would like to thank the CSI Field Support Group for designing and building the mooring and for carrying out the field program for this project, and the Coastal Studies Institute faculty and staff for providing the necessary support for this project. We would like to thank the crew of *Pelican* for helping us service the mooring during Deployments 4 and 5.

CHAPTER 1

INTRODUCTION

The first three successful deployments using a deepwater mooring deployed at the center of the eastern Gulf of Mexico (GOM) (25.5^{o}N and 87^{o}W) (Figure 1-1) at a water depth of 3356 m to observe deep water manifestation of the Loop Current (LC) and the Loop Current rings (or Loop Current Eddies, LCEs) were carried out and the results were reported previously (Inoue et al. 2008). This particular location turned out to be an ideal location not only to monitor the LC in the eastern GOM but also to observe deepwater currents under the LC and LC rings away from the rough topography of the northern slope water region. The mooring data suggest the dominance of a two-layer flow system at the mooring site with the interface located near 700-1000 m. The upper-layer currents are dominated by the LC and LCEs while the lower-layer currents appear to be manifestation of eddies in deep water. The upper- and lower-layer currents in general appear to be decoupled except occasional establishments of coupling between the two layers. Deepwater at the mooring site appears to be barotropic throughout the lower layer and relatively energetic characterized by 40-50 day variability with 10-30 cm s^{-1} currents. Short-duration energetic events lasting a few days could result in strong deepwater currents reaching 30-50 cm s^{-1} all the way to the bottom. These energetic events in deepwater appear to take place when the LC makes notable northward extension preceding the formation of LCEs. Deepwater currents at mooring site appear to be manifestations of a modon pair which forms underneath a Loop Current ring in the eastern GOM. Shorter time scales associated with deepwater flow at the mooring site is a reflection of smaller deepwater eddies resulting from deepwater eddies interacting with the bottom topography including the topographic constriction located between the eastern and the central GOM. So far, every one of the three deployments turns out to be unique, confirming the previous observation that every Loop Current ring formation is unique with predominant time scales of 6, 9, and 11 months (Sturges and Leben 2000; Leben 2005) and a long-term measurement is required in order to establish basic statistics of ocean dynamics in the eastern Gulf of Mexico.

Despite the success of the first three deployments to observe deepwater currents below the LC in the eastern GOM, a couple of important questions remained unanswered. The first was related to details of the interface between the upper- and lower-layers. Due to the paucity of the instrumentation near the depths of the interface, great details of the interface were not captured. The second question is related to detailed variability of water mass characteristics in deepwater. Again due to the paucity of the instrumentation used in deep water to measure temperature and salinity, detailed variability of temperature and salinity in deep water was not measured. This is an important question, as it is related to the dynamics of the LC and LCEs, and ultimately to the mixing of water masses in deep water below the sill depths in the eastern GOM. For example, even though the basic idea of "a modon pair" in deep water appears to fit the observations at the mooring site, deep water currents driven by the vertical excursion of the interface between the upper- and lower-layers should exhibit corresponding variability in temperature and salinity in deep water. Moreover, there is simply a great value to extend the time series at the center of the eastern GOM where significant energy peak is found close to annual cycle. In order to address these

questions, two additional years of deployment extension were proposed, approved and implemented. In order to sample not only currents but also water mass characteristics throughout the water column, additional current measurements were attempted near the interface and additional Microcats were deployed in deep water.

1.1 Water Mass Characteristics at the Mooring Site

The vertical profiles of T and S at the mooring site are presented in Figures 1-2 and 1-3, respectively. The corresponding T-S relationships are presented in Figure 1-4. These are based on the CTD profiles taken during the first three cruises for this project. A prominent feature of the salinity profile is a strong sub-surface salinity maximum found near 150 m. This sub-surface salinity maximum corresponds to the salty Subtropical Underwater (SUW) (Wust 1964; Worthington 1971). This is a remnant of the salty water annually produced in the western tropical Atlantic Ocean due to excess evaporation taking place in that region. Salinity values associated with the SUW are typically >36.6 at the mooring site. However, actual values vary from cruise to cruise. Below the SUW, salinity decreases monotonically toward a minimum located near 710 m. This salinity minimum corresponds to the remnants of the Sub-Antarctic Intermediate Water (SAIW) (Gordon 1967; Elliott 1982). Salinity values at the core of the SAIW can vary, often displaying some scatter near 710 m. Corresponding temperature decreases with depth from the surface down to approximately 1850 m, below which it increases gradually with depth. Increasing salinity with depth below 1850 m more than compensates for the impact of increasing temperature, thus resulting in statically stable density profile.

The observed tightness in the temperature-salinity relationships between the salty SUW near 150 m and a salinity minimum near 710 m associated with the remnants of the SAIW (Figure 1-4) is probably due to the dominance of salt fingers first suggested by Stern (1967) and later examined in more detail by Schmitt (1981; 1990) and recently observed (Schmitt et al. 2002) in the Caribbean Sea.

Below SAIW, salinity values appear to increase gradually all the way to the bottom (Figure 1-3), though below the sill depth at Yucatan Channel (1900 m), rate of increase becomes much less. A puzzling feature is that below the sill depth, salinity values continue to increase toward the bottom while the deep water below the sill depths is completely isolated (McLellan and Nowlin 1963). Despite the paucity of reliable historical hydrographic data in deep water in GOM, this feature appears to be present even in the western GOM (based on the Levitus climatology). Salt coming from some of the hyper-saline basins (e. g., Orca Basin) and/or ubiquitous salt domes on the bottom of GOM could be the source of high salinity water at the bottom in addition to sinking of the inflowing salty and cold water from the deep Caribbean Basin over the sill at Yucatan Channel. Concurrent increases in temperature (nearly density compensating) with depth below the sill depth (Figure 1-2) appears to be the manifestation of compressibility of seawater. Considering the weak stratification in deep water, a potentially important process for mixing is the role of eddies in deep water.

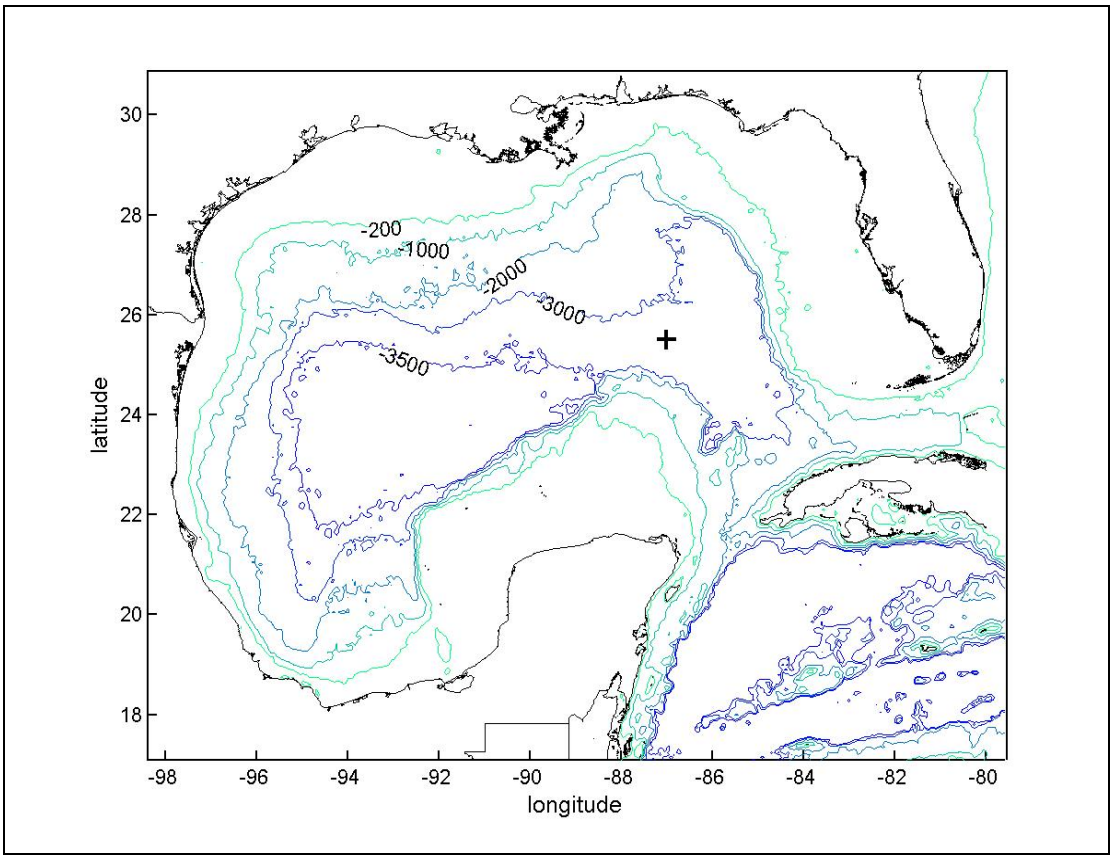

Figure 1-1. Bottom bathymetric contours (in meters) in the Gulf of Mexico. The mooring site at 25.5°N and 87°W is indicated (+) (From Figure 1-1 of Inoue et al. (2008)).

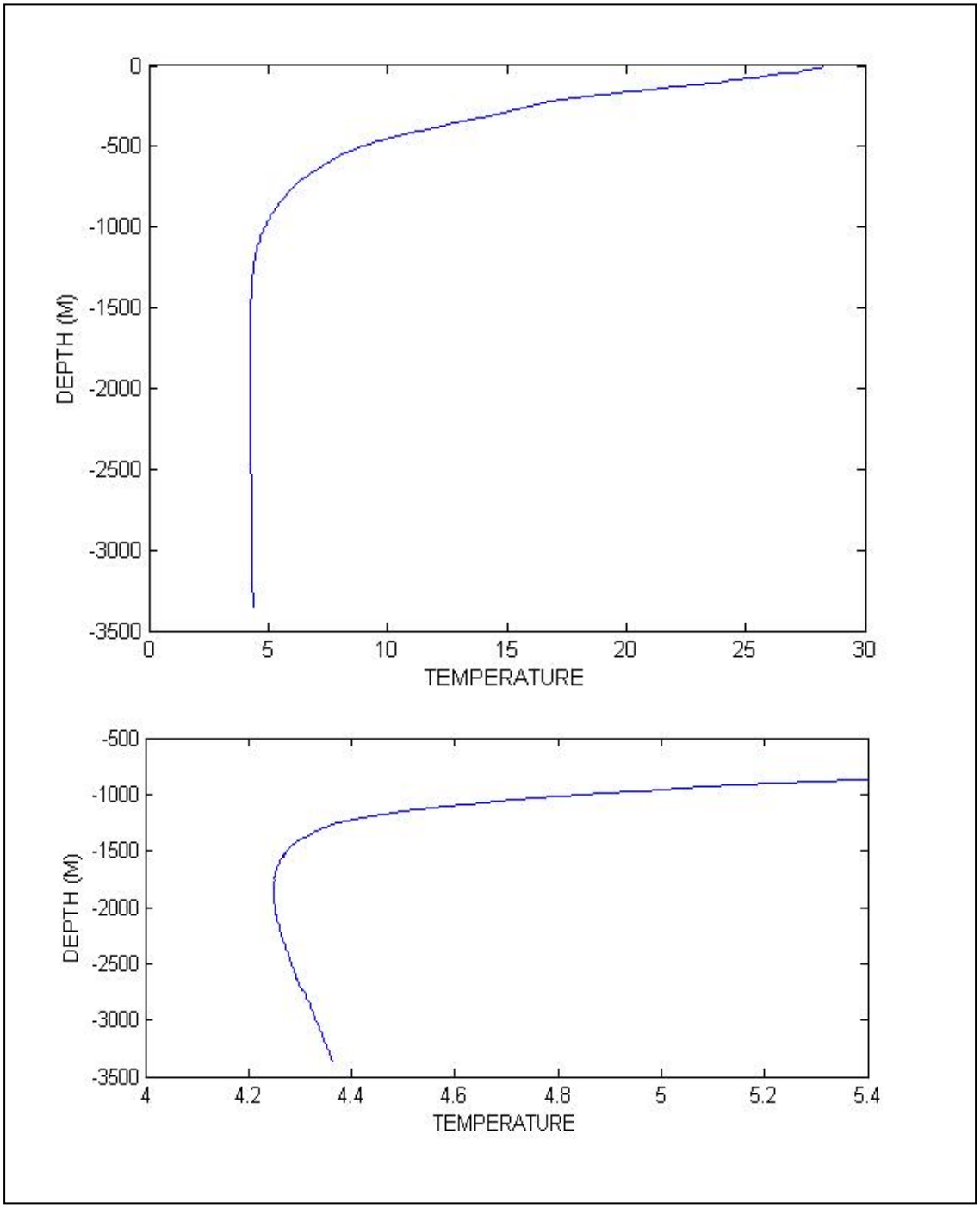

Figure 1-2. Vertical temperature profile at the mooring site estimated for the mean CTD profile based on the first three cruises. Values were extrapolated below 2870 m.

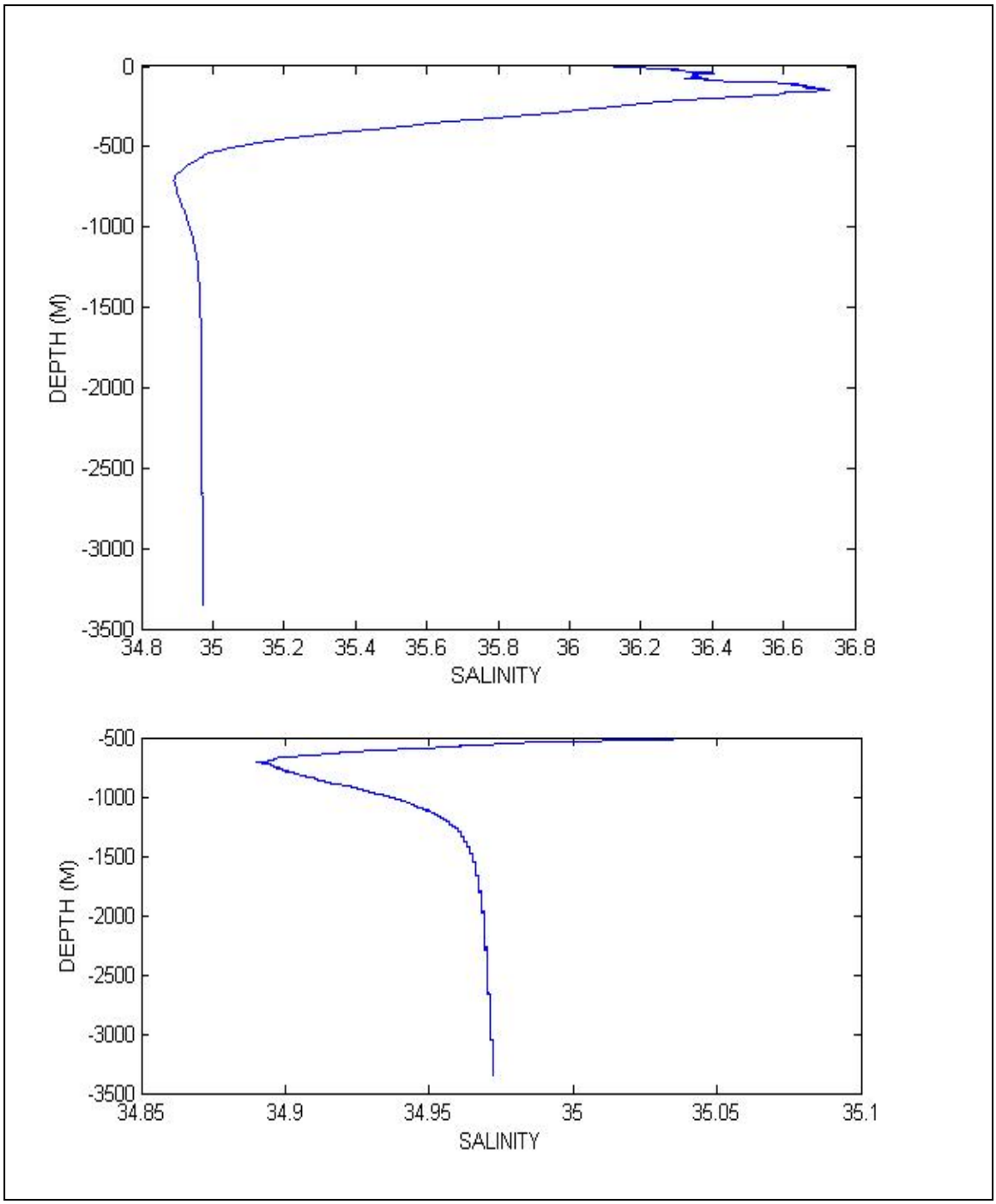

Figure 1-3. Vertical salinity profile at the mooring site estimated for the mean CTD profile based on the first three cruises. Values were extrapolated below 2870 m.

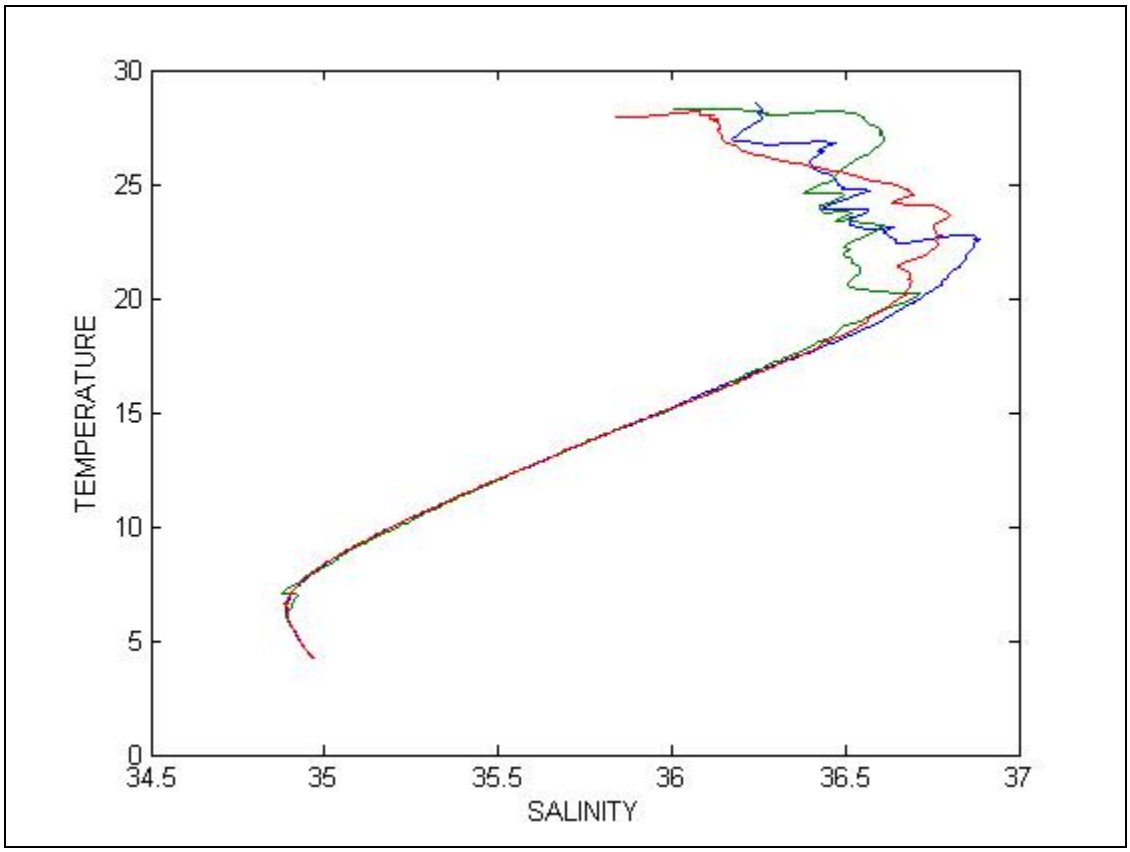

Figure 1-4. Temperature-salinity relationship at the mooring site. Lines represent CTD profiles taken during the first three cruises for the project.

CHAPTER 2

MOORING DEPLOYMENT

2.1 Deployment

Under the continuation funding, two additional deployments were completed. Although the detailed final configuration of the mooring differed between the two deployments, the primary objective remained the same, namely, to sample currents and temperature and salinity throughout the water column from near-surface all the way to near-bottom. Starting from the mooring configuration used in the first three deployments, additional current measurements were attempted near the interface depth and additional Microcats were deployed in deep water. Both deployments used two ADCPs, one upward-looking set at 140 m and the other downward-looking set at 3200 m, in order to measure currents near-surface and near-bottom, respectively, and nine Aanderaa current meters were set at 250, 350, 450, 600, 1500, 2000, 2500, 3000, and 3186 m in order to sample the entire water column. Additional current measurements were made between 700 m and 1200 m in order to catch the interface between the upper- and lower-layers. Specifically, Deployment 4 used four additional Aanderaa current meters set at 750, 875, 1000, and 1200 m, while Deployment 5 used a third ADCP set downward looking at 750 m. Compared to the previous three deployments with a total of five Microcats, significantly more detailed measurements of water mass properties (temperature and salinity) were accomplished with the use of eleven Microcats. They were set at 145, 351, 749, 1000, 1501, 1800, 2001, 2500, 3001, 3187, and 3297 m. Unfortunately, the bottom two Microcats failed. Due to the relatively flat bottom in the vicinity of the target site, each deployment was successful in targeting the design depth of 3340 m.

Deployment 4 extended from May 29, 2005, to June 15, 2006. Deployment 5 covered the period from June 17, 2006, to July 10, 2007. Detailed information on the mooring configuration and deployment for each deployment can be found in Tables 2-1 and 2-2, respectively. Despite the loss of the top part of the mooring during Deployment 5 (see Appendix C) and additional failure of a few Aanderaa meters, nearly continuous two-year measurements of currents and water mass properties throughout the water column at the mooring site were collected.

All raw data records were downloaded, and underwent quality control to flag bad and suspicious data values. Current meter records were corrected for declination, Earth's changing magnetic field, by correcting for a declination value at mid-way point during each deployment. The original current meter data were recorded at 60-minute intervals by Aanderaa current meters while Microcats recorded data at 30-minute intervals. However, all ADCP were erroneously set to sample at 4.5-hour intervals. The current velocity records were aligned along east-west (U-component) and north-south (V-component). Unlike the previous three deployments where there were hardly any data gaps, several Aanderaa meters, especially those deployed near mid-depth, did not work properly, resulting in significant data gaps. Interpolation was not attempted for those data gaps.

Table 2-1

Information during Deployment 4 Deployed at 25°30.456”N and 86°58.063”W

	S/N	Design Depth	Start	End	Days	
ADCP 300		140	5/29/05 18:30	6/14/06 17:30	381.0	99%
Microcat	2447	145	5/29/05 18:30	6/15/06 17:00	381.9	100%
Aanderaa	10191	250	5/29/05 20:00	6/15/06 15:51	381.8	100%
Aanderaa	10193	350	5/29/05 19:00	6/15/06 16:02	381.9	100%
Microcat	1332	351	5/29/05 18:30	6/15/06 17:00	381.9	100%
Aanderaa	10194	450	5/29/05 18:59	6/15/06 15:58	381.9	100%
Aanderaa	10196	600	5/29/05 20:00	3/11/06 20:00	286.0	75%
Microcat	2452	749	5/29/05 18:30	6/15/06 17:30	382.0	100%
Aanderaa	12058	750	5/29/05 18:59	6/15/06 16:00	381.9	100%
Aanderaa	10260	875	5/29/05 18:59	2/12/06 9:52	258.6	68%
Microcat	1334	1000	5/29/05 18:30	6/15/06 17:00	381.9	100%
Aanderaa	12700	1001	5/29/05 19:00	6/15/06 16:01	381.9	100%
Aanderaa	12701	1200	5/29/05 19:00	6/15/06 16:01	381.9	100%
Aanderaa	12702	1500	5/29/05 19:00	5/29/05 19:00	0.0	0%
MicroCat	1335	1501	5/29/05 18:30	6/15/06 17:30	382.0	100%
MicroCat	1338	1800	5/29/05 18:30	6/15/06 17:30	382.0	100%
Aanderaa	12768	2000	5/29/05 19:00	6/15/06 15:58	381.9	100%
MicroCat	1337	2001	5/29/05 18:30	6/15/06 17:30	382.0	100%
Aanderaa	12703	2500	5/29/05 20:00	6/15/06 17:05	381.9	100%
MicroCat	1336	2500	5/29/05 19:00	6/15/06 17:30	381.9	100%
Aanderaa	12750	3000	5/29/05 19:00	6/15/06 16:56	381.9	100%
MicroCat	1693	3001	5/29/05 18:30	6/15/06 17:30	382.0	100%
Aanderaa	180	3186	5/29/05 19:00	6/15/06 16:55	381.9	100%
MicroCat	1691	3187	5/29/05 18:30	5/29/05 18:30	0.0	0%
ADCP 300		3190	5/29/05 0:00	6/14/06 4:30	381.2	100%
MicroCat	37	3297	Lost	Lost	0.0	0%
Bottom		3340				

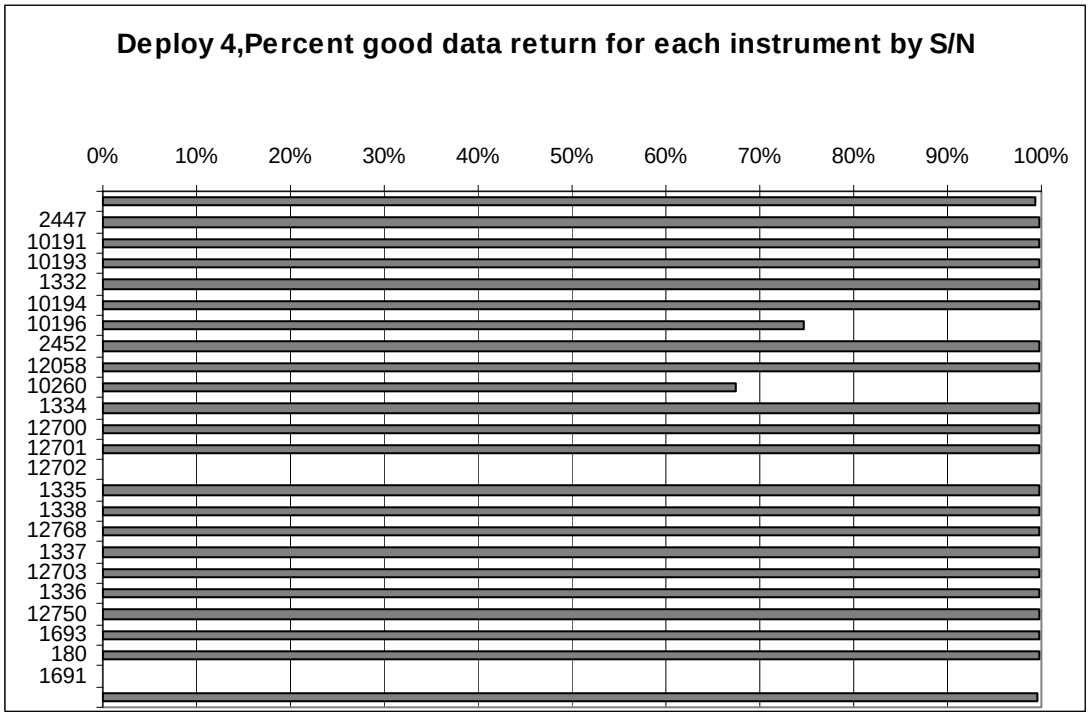

Table 2-2

Information during Deployment 5 Deployed at 25°30.534”N and 86°57.804”W

	S/N	Design Depth	Start	End	Days	
ADCP 300					0.0	0%
Microcat	1691				0.0	0%
Aanderaa	10260	250	6/17/06 19:59	3/25/07 3:52	280.3	72%
Aanderaa	10258	350	6/17/06 18:59	3/25/07 3:52	388.0	72%
Microcat	1332	350	6/17/06 20:00	3/25/07 20:00	281.0	72%
Aanderaa	12701	450	6/17/06 19:00	3/25/07 3:52	388.0	72%
Aanderaa	12700	600	6/17/06 18:55	7/10/07 19:54	388.0	100%
Microcat	2425	750	6/17/06 20:00	7/10/07 20:00	388.0	100%
ADCP 75	ADCP	752	6/17/06 20:00	7/10/07 20:00	388.0	100%
Microcat	1334	1000	6/17/06 20:00	7/10/07 20:00	388.0	100%
Aanderaa	12702	1500	6/17/06 19:00	7/10/07 19:58	388.0	100%
MicroCat	1335	1500	6/17/06 20:00	7/10/07 20:00	388.0	100%
MicroCat	1338	1800	6/17/06 20:00	7/10/07 20:00	388.0	100%
MicroCat	1337	2000	6/17/06 20:00	7/10/07 20:00	388.0	100%
Aanderaa	12768	2000	6/17/06 19:00	7/10/07 18:58	388.0	100%
Aanderaa	12703	2500	6/17/06 19:00	7/10/07 20:06	388.0	100%
MicroCat	1336	2500	6/17/06 20:00	7/10/07 20:00	388.0	100%
Aanderaa	12750	3000	6/17/06 18:52	7/10/07 20:49	388.1	100%
MicroCat	1693	3000	6/17/06 20:00	7/10/07 20:00	388.0	100%
Aanderaa	180	3186	6/17/06 18:51	7/10/07 19:46	388.0	100%
MicroCat					0.0	0%
ADCP 300	ADCP		6/17/06 20:00	7/10/07 20:00	388.0	100%
MicroCat					0.0	0%
Bottom		3340				

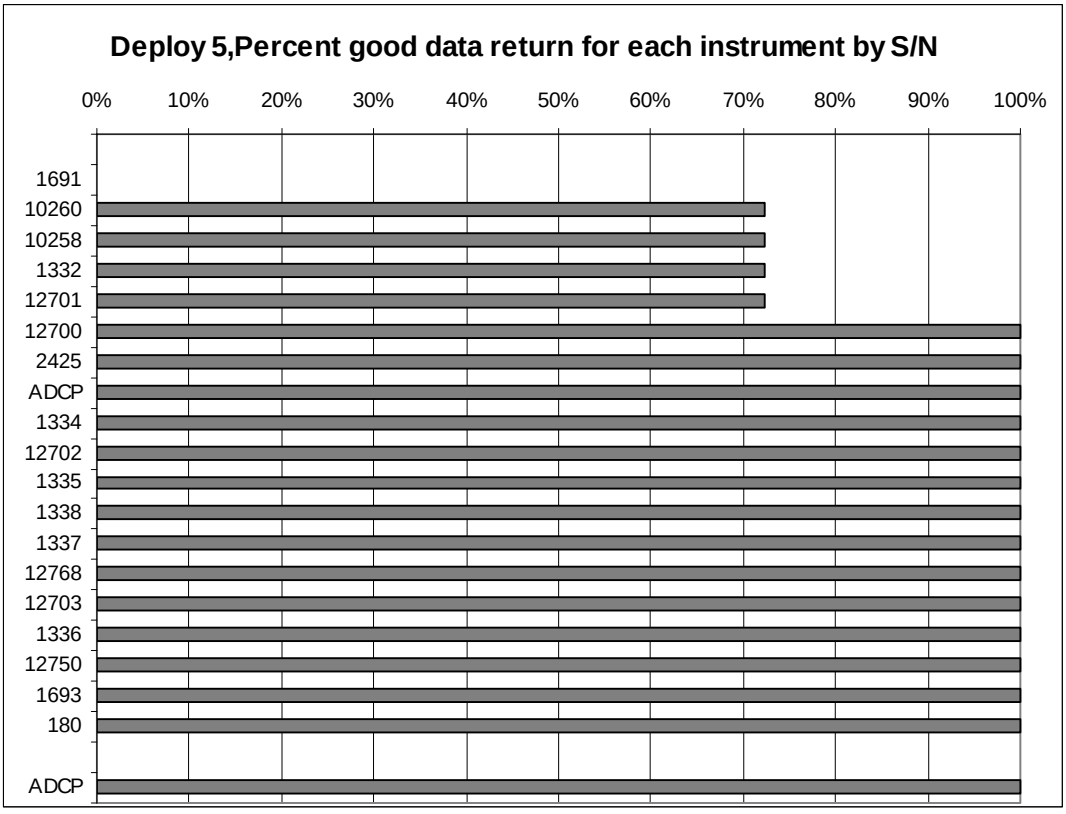

2.2 Basic Statistics

In order to examine low-frequency current variability that excludes dominant semi and diurnal tides and inertial oscillations, the original current meter data (sampled either at hourly or at 4.5-hour intervals) were low pass filtered with a 40-hour low-pass (40-HRLP) filter (specifically 6th degree Butterworth filter). Statistics of currents during the two deployments for both raw hourly-sampled data and 40-HRLP are presented in Table 2-3.

Current vector plots of 40-HRLP current meter data are presented in Figures 2-1 and 2-2 for Deployments 4 and 5, respectively. As was evident for the first three deployments, currents at the mooring site can be approximated by a two-layer system. The upper-layer flow is dominated by the LC and the LC rings with characteristic surface-intensified flow pattern. The lower-layer currents appear to be nearly barotropic, i. e., current magnitude and direction do not change with depth. Although the lower-layer flow appears to be related to the upper-layer flow on many occasions, decoupling of the upper- and lower-layers takes place frequently.

Record-length statistics of current speed including mean, maximum and one standard deviation around the mean are graphically presented in Figures 2-3 and 2-4 for the two deployments. In both deployments, the observed currents generally display vertical profile that can be approximated by a combination of the barotropic mode and the first baroclinic mode (Figure 2-5). It is interesting that the depth of the interface between the upper- and lower-layer appears to be close to the zero crossing of the first baroclinic mode estimated at the mooring site. The very strong near-surface currents were difficult to measure due to the blow-over experienced by the top ADCP. However, maximum currents of 175 cm s^{-1} were recorded during Deployment 4, comparable to maximum currents captured by the first three deployments. During Deployment 5, strongest surface currents were not recorded due to the loss of the top current meters (see Appendix C). Maximum deep water currents were 39-43 cm s^{-1} in Deployment 4 while Deployment 5 shows 42-43 cm s^{-1}. These values are comparable to those during Deployments 1 and 2. Deployment 3 remains as the most energetic deployment in deep water with maximum currents of slightly more than 50 cm s^{-1}. In deep water, mean currents were 11 to 13 cm s^{-1} during Deployment 4 and 10 to 11 cm s^{-1} in Deployment 5. Standard deviation of current speeds in deep water were in the range of 6 to 9 cm s^{-1}, similar to what were observed during the first three deployments.

The resulting mean velocity vectors and standard deviation ellipses from raw hourly sampled data and from 40-HRLP current data are presented in Figures 2-6 and 2-7 for each of the two deployments. Corresponding table is found in Table 2-3. Apparently, location of the mooring relative to the LC shifted from deployment to deployment, thus resulting in the slight differences in the direction of the mean currents. During Deployment 4, the mooring was located primarily on the eastern side of the LC while during Deployment 5, the mooring shifted to the western side of the LC. In contrast, mean currents in deep water exhibit long-term northward drift in both deployments, similar to what was observed during the first three deployments.

Table 2-3

Basic Statistics of Observed Currents for Deployments 4 and 5.
(Depth refers to nominal design depth.)

Deploy 4	Mean Raw			Maximum Raw			Standard Deviation Raw			Standard Deviation 40HLP			Ratio KE40: KEraw	Principal Axis Direction
Depth(m)	U	V	Speed	U	V	Speed	U	V	Speed	U	V	Speed	(%)	(True)
-54	24.6	3.1	50.7	132.0	136.6	153.1	35.3	35.3	35.1	32.6	39.2	35.6	84	25
-102	20.6	-4.4	44.2	106.9	108.3	128.9	31.7	31.7	28.7	30.8	35.6	28.9	96	30
-250	12.6	-2.2	31.8	86.4	88.0	175.2	23.1	23.1	19.1	22.1	25.2	18.7	93	24
-350	9.0	-0.3	26.0	82.8	70.8	83.9	19.8	19.8	15.4	18.5	19.9	14.2	90	26
-450	6.6	-1.3	20.0	57.9	63.0	69.1	15.5	15.5	12.3	14.3	15.3	11.3	88	27
-600	4.4	-1.9	14.3	57.6	40.6	60.1	13.0	13.0	11.4	11.9	10.6	10.2	83	164
-750	1.0	1.9	13.3	39.7	53.2	54.0	10.7	10.7	8.3	9.6	10.0	7.2	81	6
-875	0.6	1.2	9.5	34.4	43.6	46.4	9.2	9.2	8.6	8.1	7.7	7.4	77	149
-1200	-1.1	3.1	12.0	29.2	37.2	40.3	9.7	9.7	7.0	9.1	8.6	6.2	86	152
-1500	-1.2	3.9	12.4	36.3	42.3	42.9	10.1	9.3	7.3	9.8	9.0	6.8	94	166
-2000	-2.1	3.8	11.9	28.4	36.3	39.0	9.2	9.2	6.4	9.0	8.7	6.2	96	148
-2500	-1.9	3.6	13.3	32.6	40.6	42.7	10.6	10.6	7.1	10.4	9.7	6.9	97	153
-3004	-2.4	4.3	13.4	27.4	37.5	39.7	10.5	10.5	7.5	10.3	9.8	7.3	97	154
-3186	-2.0	2.8	11.1	26.5	35.6	37.0	8.9	8.9	6.0	8.7	8.1	5.9	96	162
-3240	-2.2	3.3	11.9	27.7	36.2	38.7	9.2	9.2	6.4	9.1	8.8	6.3	97	154
-3248	-2.4	3.3	12.5	27.8	37.1	39.7	10.0	10.0	6.5	9.8	8.9	6.4	97	168
-3256	-2.5	3.3	12.6	27.5	37.6	40.1	10.1	10.1	6.5	9.9	9.0	6.4	97	169
-3264	-2.5	3.3	12.7	28.0	36.3	39.4	10.1	10.1	6.6	9.9	9.0	6.4	97	170
-3272	-2.5	3.4	12.8	27.4	36.5	39.1	10.1	10.1	6.6	10.0	9.1	6.5	96	170
-3280	-2.5	3.3	12.9	27.6	38.2	41.8	10.2	10.2	6.6	10.0	9.2	6.5	96	169
-3288	-2.5	3.4	13.0	28.3	40.2	43.2	10.3	10.3	6.7	10.1	9.2	6.5	95	171
-3296	-2.5	3.3	13.2	27.5	44.6	45.7	10.4	10.4	6.8	10.1	9.2	6.6	93	168
-3304	-2.5	3.1	13.7	28.6	45.8	49.2	10.8	10.8	7.0	10.3	9.6	6.7	90	160

Deploy 5	Mean Raw			Maximum Raw			Standard Deviation Raw			Standard Deviation 40HLP			Ratio KE40:	Principal Axis
Depth(m)	U	V	Speed	U	V	Speed	U	V	Speed	U	V	Speed	KEraw	
-250	10.4	13.2	27.6	78.0	86.2	86.5	14.9	23.4	17.0	13.8	22.5	16.6	93	175
-350	6.6	3.2	16.1	48.6	58.2	63.9	12.2	14.7	12.7	11.0	14.0	12.0	89	1
-450	3.0	10.8	18.6	58.6	66.0	66.2	12.7	15.3	13.3	12.1	14.8	12.8	94	179
-600	2.9	5.1	11.7	42.1	50.8	55.7	9.0	11.9	10.9	8.2	11.1	10.1	88	166
-786	1.9	4.3	11.8	29.0	40.0	43.5	8.3	10.4	7.6	7.7	9.9	7.4	88	166
-826	1.4	4.4	12.1	28.0	38.0	38.1	8.8	10.3	7.6	8.2	9.8	7.5	90	159
-866	1.2	4.4	11.9	30.0	33.0	38.6	8.8	10.1	7.6	8.2	9.6	7.3	90	158
-906	0.8	4.2	11.6	26.0	33.0	35.1	8.8	9.5	7.2	8.2	9.1	7.1	90	151
-954	0.5	4.0	11.1	27.0	33.0	36.7	8.7	9.0	7.1	8.2	8.6	6.9	91	143
-994	0.2	3.8	10.9	27.0	34.0	37.7	8.7	8.9	7.1	8.2	8.4	6.8	91	141
-1034	-0.1	3.7	10.9	27.0	34.0	39.9	8.8	8.8	7.0	8.3	8.3	6.8	91	136
-1500	-0.4	2.9	10.2	30.2	37.0	43.5	10.3	8.4	9.0	10.1	8.2	8.7	96	173
-2000	-0.7	1.6	10.7	28.4	31.9	42.2	10.4	8.4	8.2	10.2	8.2	8.1	97	173
-3001	-1.4	4.2	11.5	26.8	38.2	44.4	10.5	9.1	8.9	10.3	8.9	8.7	97	164
-3186	-1.0	2.6	9.8	28.0	30.5	41.4	8.9	7.6	7.0	8.8	7.4	7.0	96	167
-3216	-2.3	3.1	10.9	22.2	37.6	42.9	9.1	8.9	7.6	8.9	8.8	7.7	97	143
-3224	-2.6	3.2	11.3	23.3	37.5	42.5	9.5	9.0	7.7	9.3	8.8	7.8	97	157
-3232	-2.6	3.2	11.4	24.0	38.4	42.9	9.5	9.0	7.7	9.3	8.8	7.8	97	158
-3240	-2.7	3.2	11.5	23.5	38.3	43.3	9.5	9.1	7.7	9.4	8.9	7.8	96	158
-3248	-2.7	3.3	11.6	22.9	39.9	42.7	9.6	9.1	7.7	9.4	8.9	7.7	96	157
-3256	-2.8	3.2	11.8	26.2	38.4	43.0	9.7	9.2	7.6	9.5	8.9	7.7	95	156
-3264	-2.9	3.2	12.2	26.7	39.5	42.3	9.8	9.6	7.6	9.6	9.2	7.8	94	148
-3272	-3.0	3.3	12.4	25.1	38.8	40.5	9.9	9.6	7.4	9.5	9.0	7.6	91	152

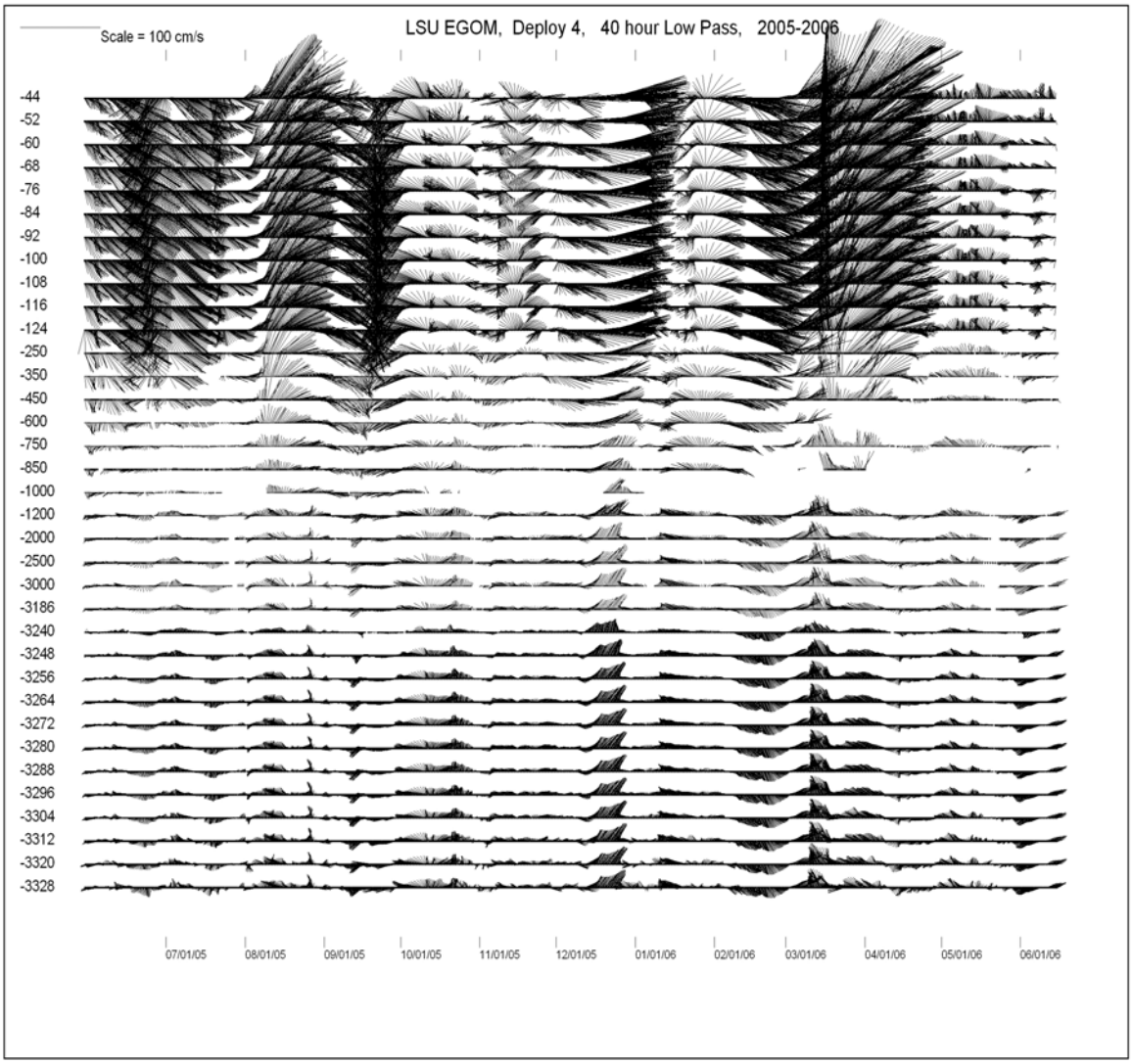

Figure 2-1. 40-HRLP current vectors during Deployment 4 for the indicated depths.

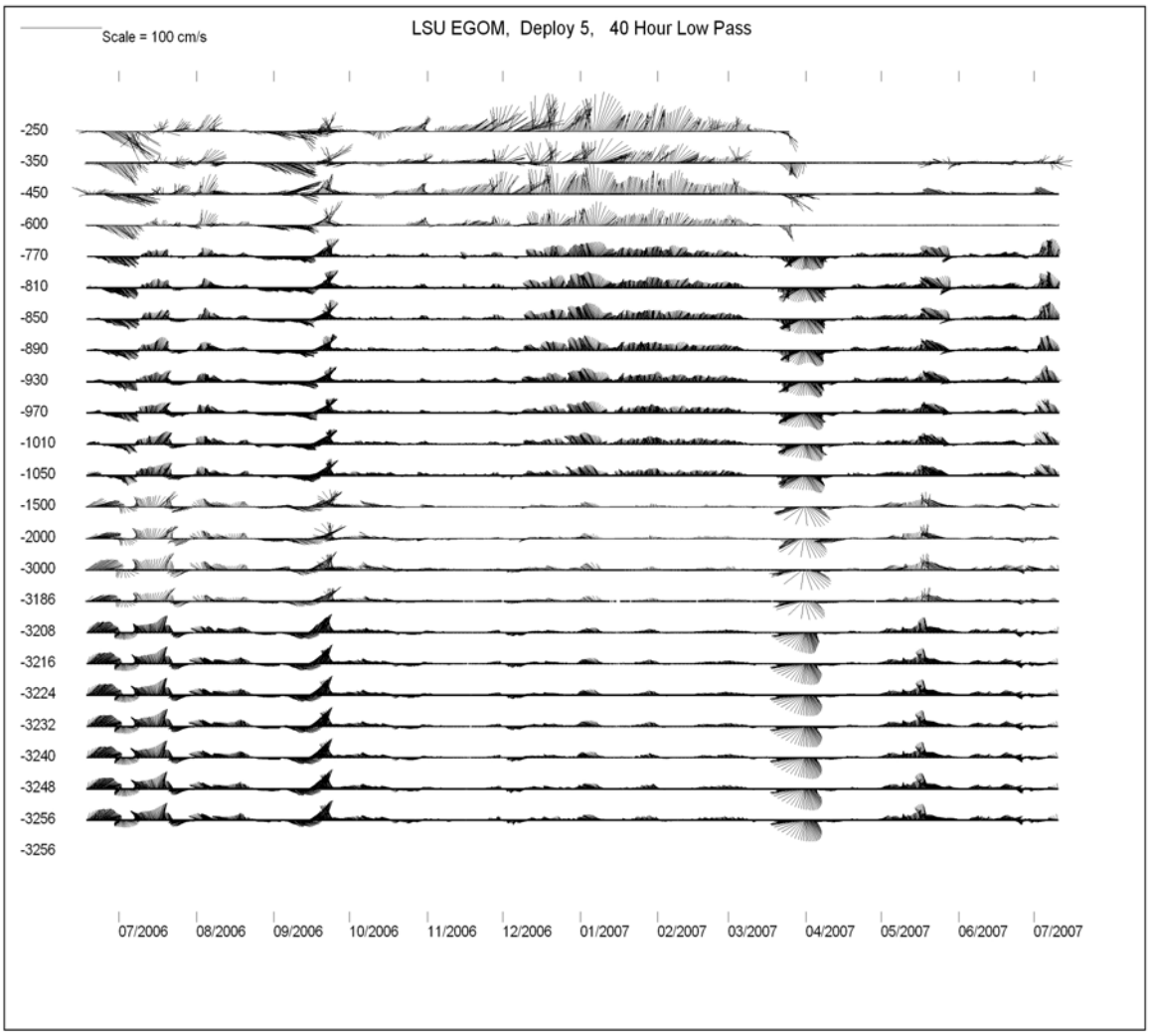

Figure 2-2. 40-HRLP current vectors during Deployment 5 for the indicated depths.

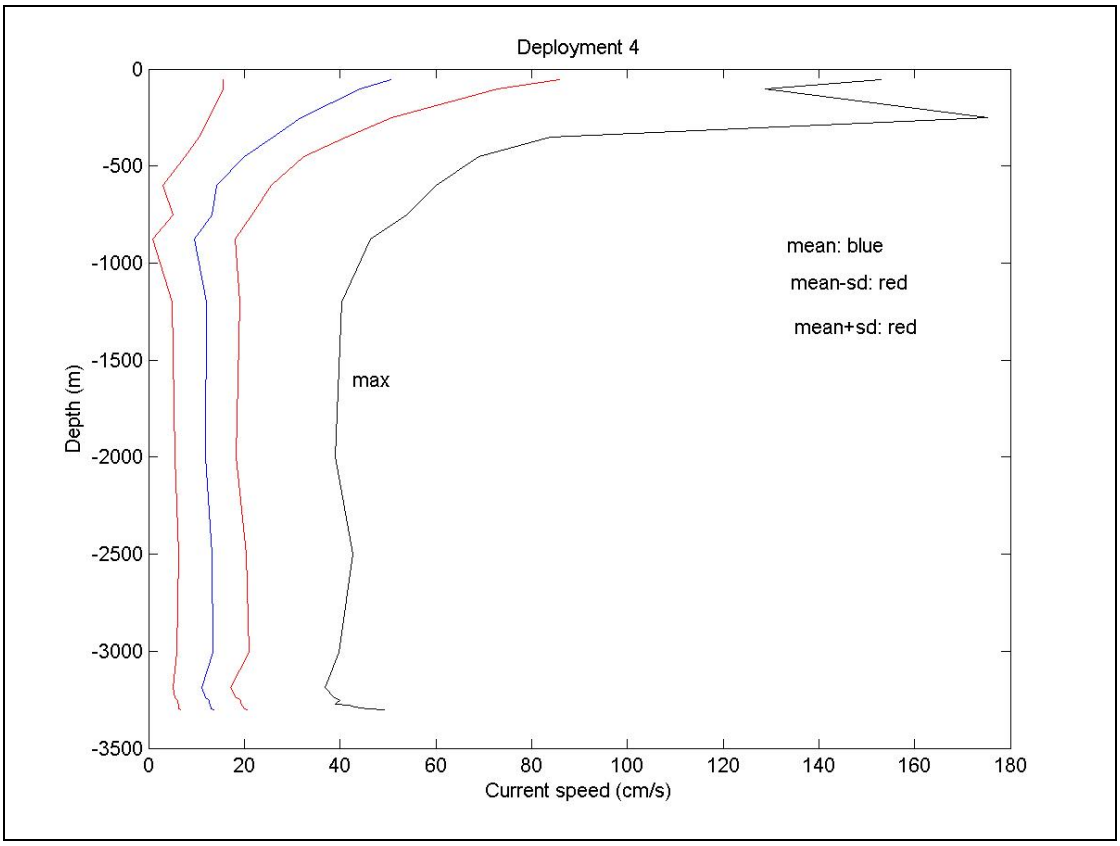

Figure 2-3. Record-length statistics (mean, maximum, 1 standard deviation around mean) of current speed during Deployment 4.

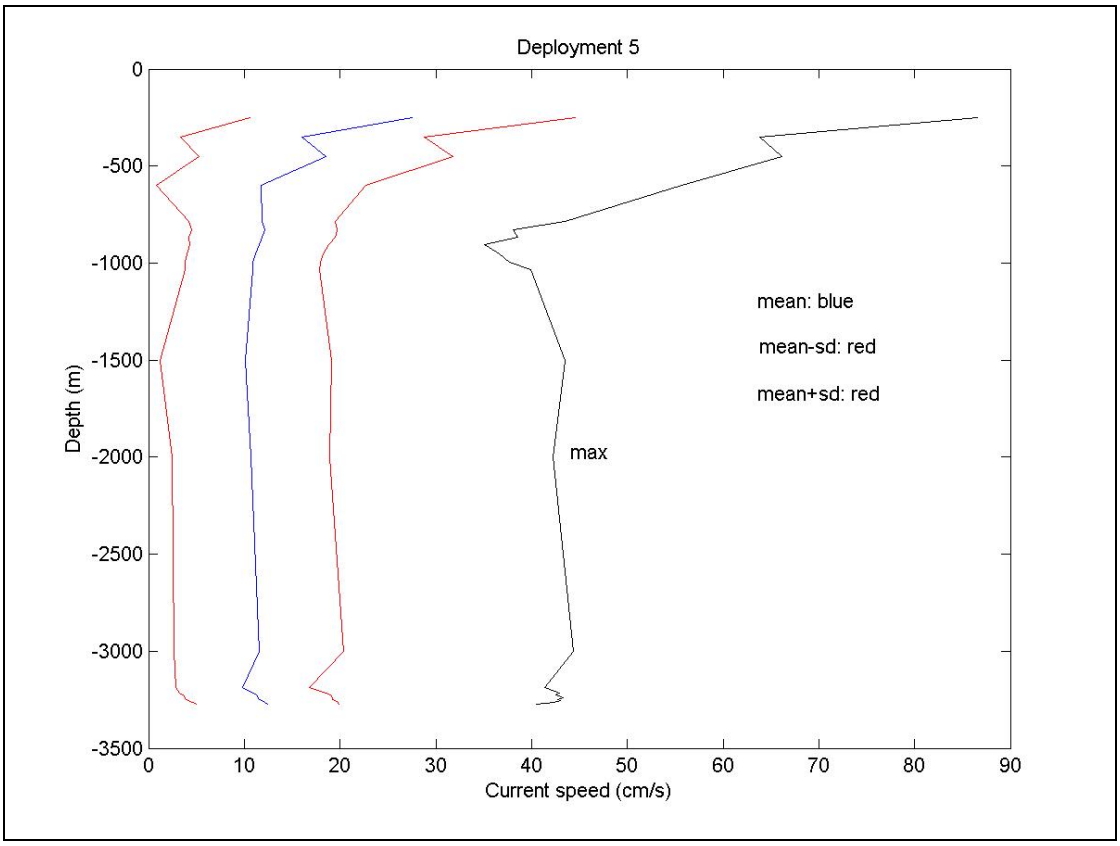

Figure 2-4. Record-length statistics (mean, maximum, 1 standard deviation around mean) of current speed during Deployment 5.

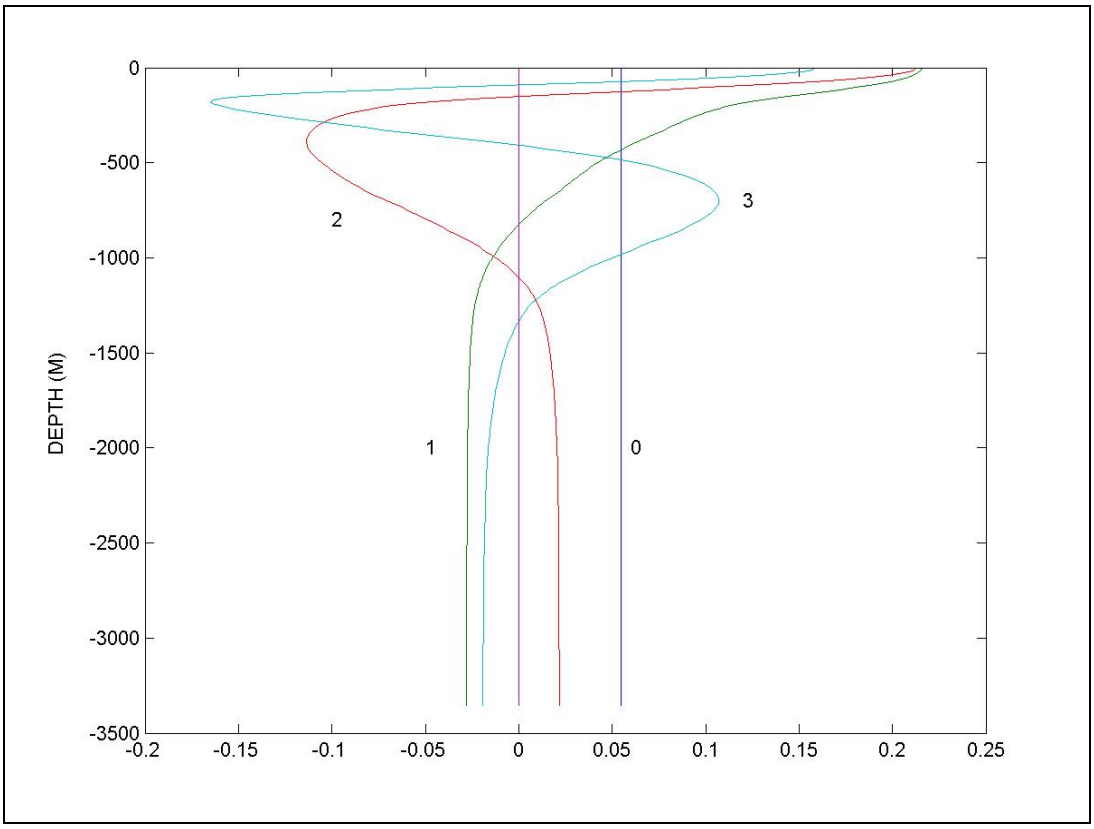

Figure 2-5. Vertical profiles of dynamic normal modes computed for the mooring site using mean temperature and salinity profiles sampled by CTD stations taken during deployments. Mode 0 is barotropic mode, Mode 1 refers to the first baroclinic mode, etc (from Figure 2-7 of Inoue et al. (2008)).

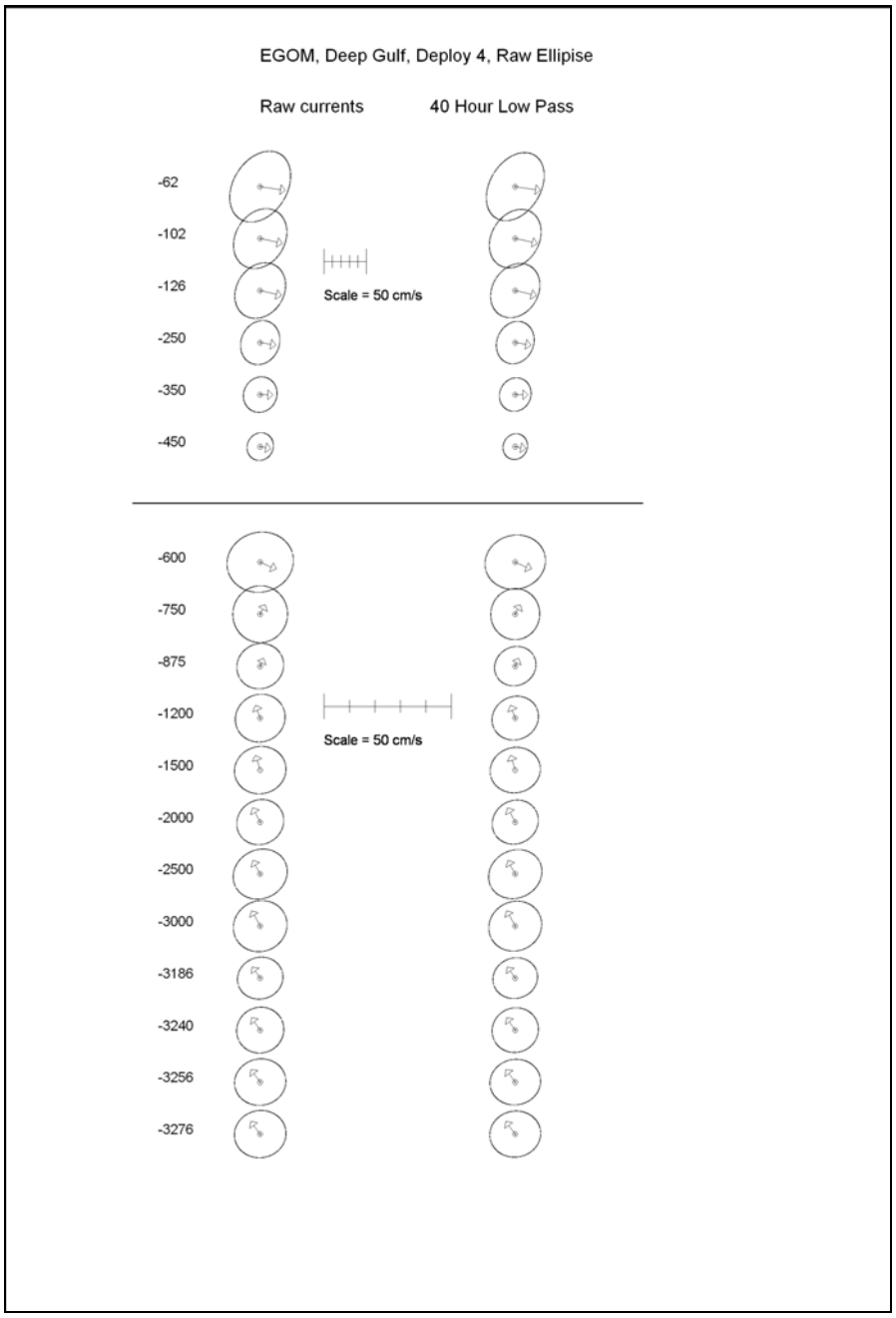

Figure 2-6. Standard deviation ellipses and mean velocity vectors from raw (hourly-sampled) and 40-HRLP current data for various depths during Deployment 4.

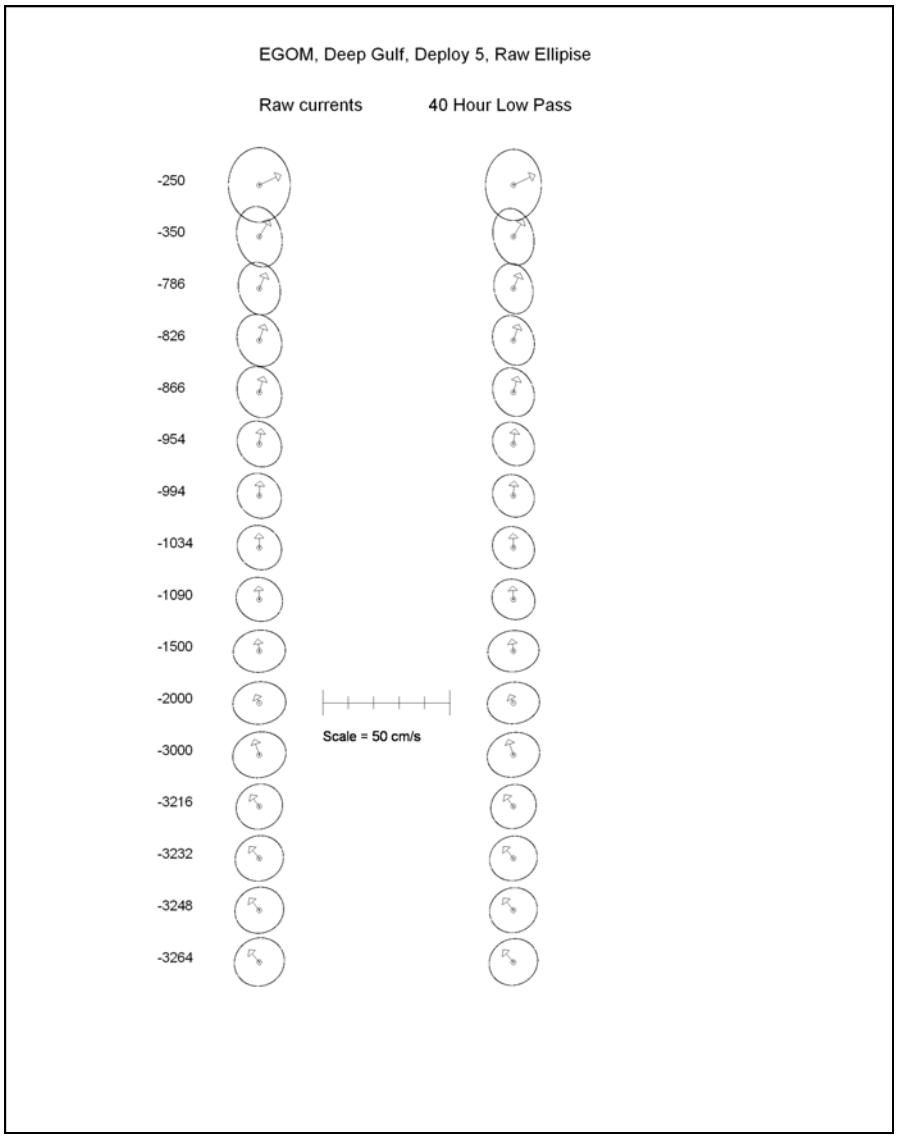

Figure 2-7. Standard deviation ellipses and mean velocity vectors from raw (hourly-sampled) and 40-HRLP current data for various depths during Deployment 5.

The orientation of the major axis of ellipse generally runs northeast-southwest in Deployment 4 while it runs northwest-southeast to north-south in Deployment 5. In Deployment 4, current characteristics changes from that of upper-layer below 600 m, and to that of lower-layer at 1200 m, while those at 750 m and 875 m exhibit characteristics somewhere between. In deployment 5, the transition from the upper-layer to the lower-layer takes place between 786 m and 1090 m. From those observations, it appears that the transition between the upper- and lower-layer takes place between 750 m and 1000 m. However, a clear-cut sharp interface cannot be identified. This is somewhat expected in that the interface observed by the mooring changes depth dependent on the location of the mooring relative to the LC, i. e., when the mooring moves out of the LC, the interface would move upward. This can also be seen in Figure 2-5 that shows the vertical profile of the first baroclinic mode transitions from the upper-layer to the lower-layer from 750 m to 1000 m with zero-crossing located at 830 m.

Currents in the lower-layer show more isotropic characteristics than the upper-layer counterparts suggesting that it may be primarily driven by passage of eddy-like features rather than a steady current like the LC. Long-term mean current in the lower-layer is again northerly in both deployments, confirming the previous three deployments. Mean current vectors and size and shape of ellipses are not much different between raw data and 40-HRLP data, suggesting that the observed currents are dominated by low-frequency currents.

2.3 Spectra

Spectra of currents were computed for north-south and east-west components using raw hourly-sampled data in the upper-layer (represented at 250 m) and in the lower-layer represented at 3004 m in Deployment 4, 3000 m in Deployment 5 with additional intermediate depths included (875 m in Deployment 4 and 975 m in Deployment 5). Results are presented in Figures 2-8 and 2-9.

Notable peaks associated with diurnal tides and inertial oscillations (~27.8 hours) are evident throughout the water column. Overall, the upper-layer is much more energetic compared to the lower-layer with prominent low-frequency peaks found in the range of 40-80 days in the upper-layer while in the lower-layer they are located near 40 days. There appears to be another peak near 15 days in deep water during Deployment 5. These observations are consistent with what was observed during the first three deployments. Dominant time scales in the upper-layer are dictated by the movement of the LC relative to the mooring while in the lower-layer, shorter time-scales found are manifestations of smaller-scale deep water eddies. In terms of the shape of the spectra, currents at 875 m in Deployment 4 and those at 975 m are quite similar to those at 3000 m. However, currents in the transition zone near the interface between the upper- and lower-layers exhibit the least energy level even compared to those in deep water.

The low frequency peak associated with the LC frontal jet is much weaker at 600 m (not shown here) compared to what was measured by the upper meters. However, it still retains the low-frequency peak characteristics of the upper-layer while currents at 750 m have already transitioned into the lower-layer characteristics. Although overall shape of spectra for the upper- and lower-layer remains more or less similar throughout the five deployments, details vary from

deployment to deployment, suggesting that because of relatively long time scales associated with formation of LC rings in the eastern GOM, any one-year observation is not sufficiently long to capture basic statistics of flow field driven by the LC.

In order to test relationships between upper-layer and lower-layer current components, coherence squared and phase were computed using the longest common record length raw current data. For the estimate of squared coherence, the data were averaged over 30 frequencies. Deployments 4 and 5 show significant coherence between upper and lower layers for periods longer than 14 days for east-west component and similarly for north-south component in Deployment 4 while north-south component in Deployment 5 shows coherence peak near 6 days. Overall, upper-layer and lower-layer currents are said to be decoupled except for periods ranging from 14 to 30 days for north-south component. They are consistent with the idea that the upper-layer currents are directly driven by the LC and LC rings while lower-layer currents are primarily driven by different mechanisms (Sturges et al. 1993; Welsh 1996; Oey 1996; Welsh and Inoue 2000; Romanou and Chassignet 2004; Chérubin et al. 2005; Oey et al. 2005) and occasional coupling between the upper- and lower-layers takes place when deep water energetics are driven by the interface movements associated with the formation of LCEs (Inoue et al. 2008).

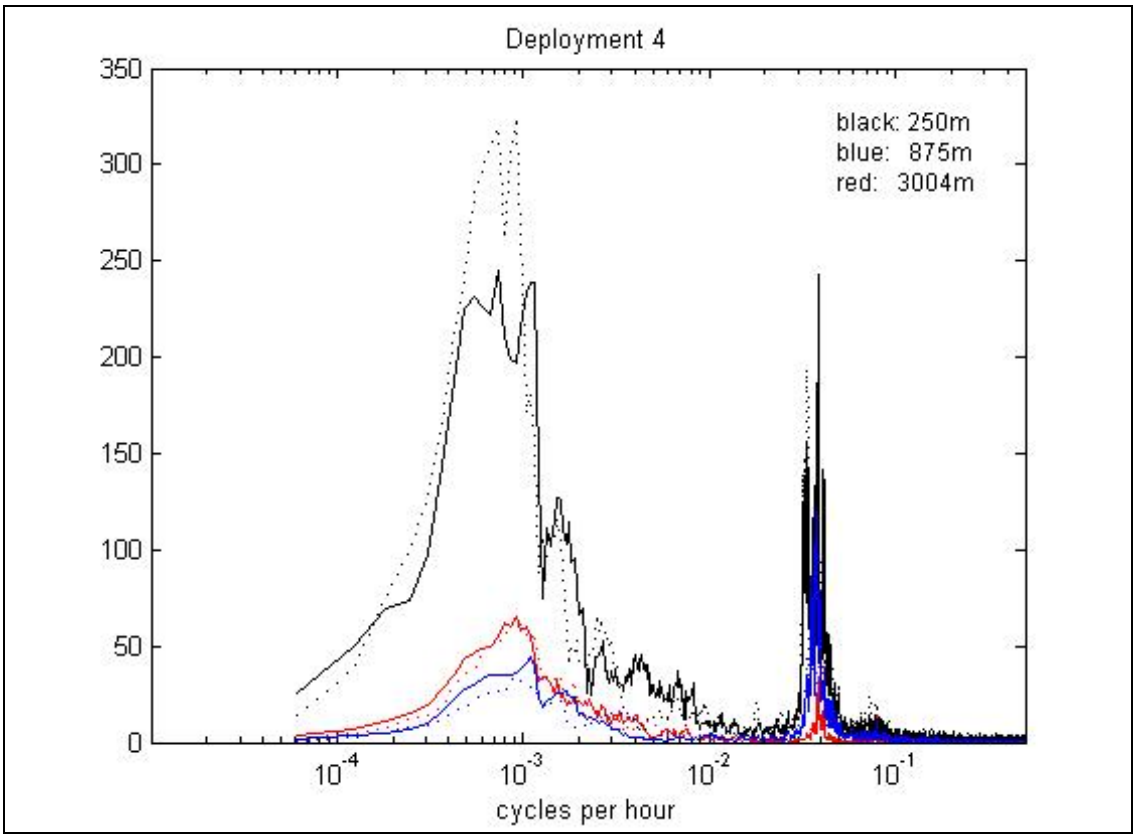

Figure 2-8. Current spectra in variance preserving form, for raw (hourly-sampled) current components (east-west component (solid line), north-south component (dotted line)) at 250 m, 875 m, and 3004 m during Deployment 4.

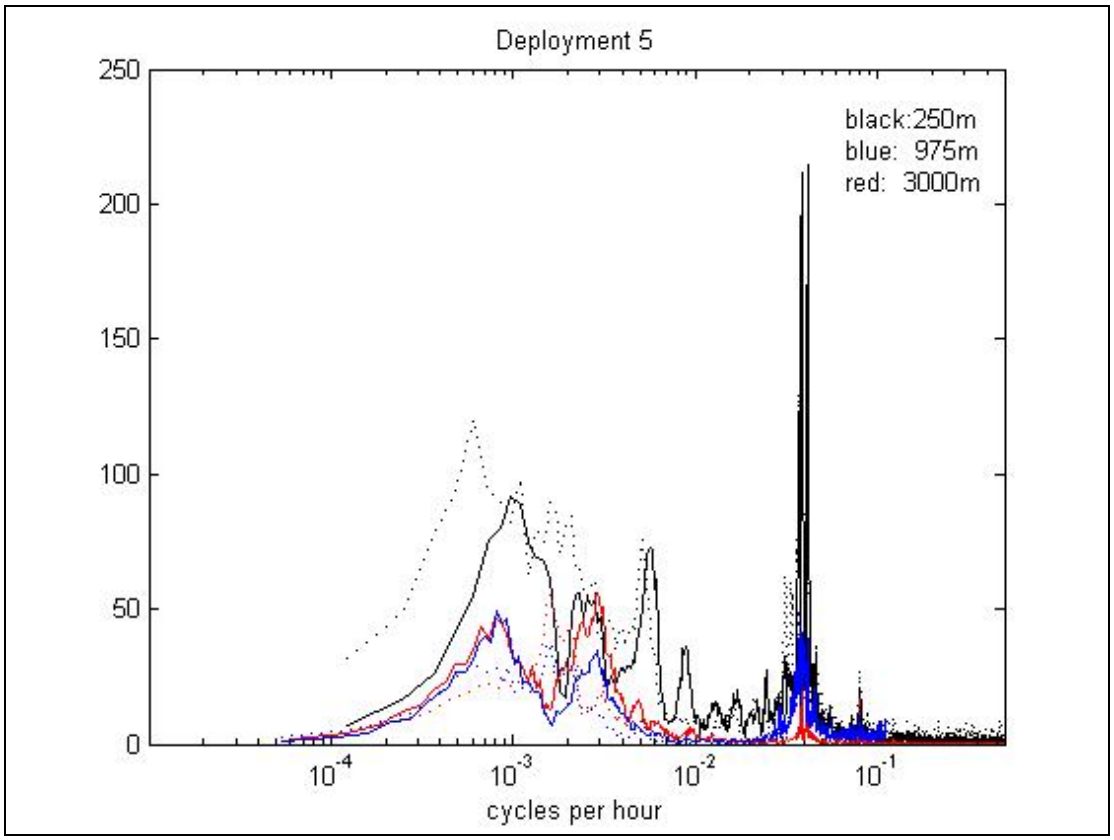

Figure 2-9. Current spectra in variance preserving form, for raw (hourly-sampled) current components (east-west component (solid line), north-south component (dotted line)) at 250 m, 975 m, and 3000 m during Deployment 5.

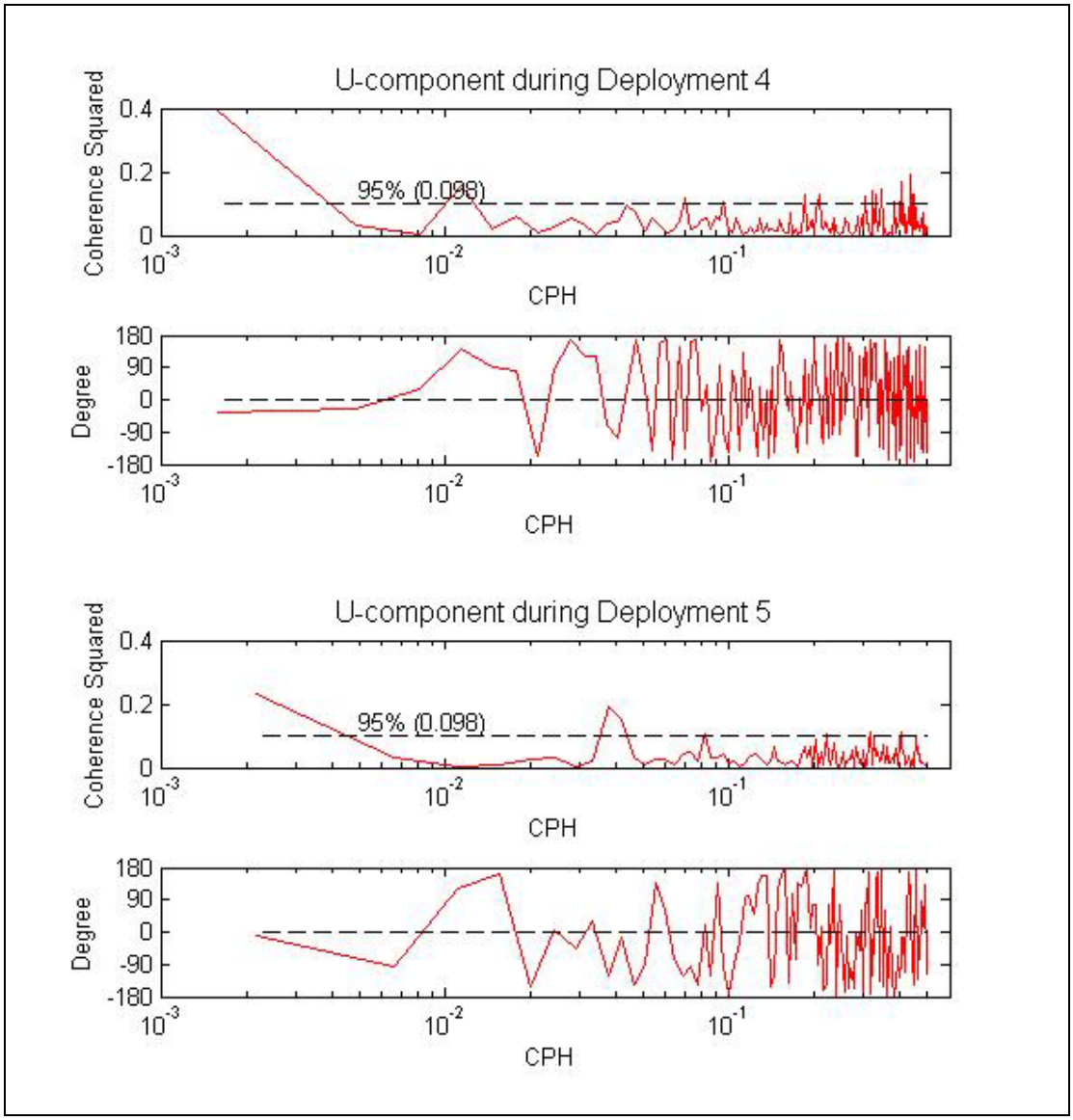

Figure 2-10. Coherence squared and phase between top (250 m) and bottom (3004 m in Deployment 4 and 3000 m in Deployment 5) U-component during Deployments 4 and 5.

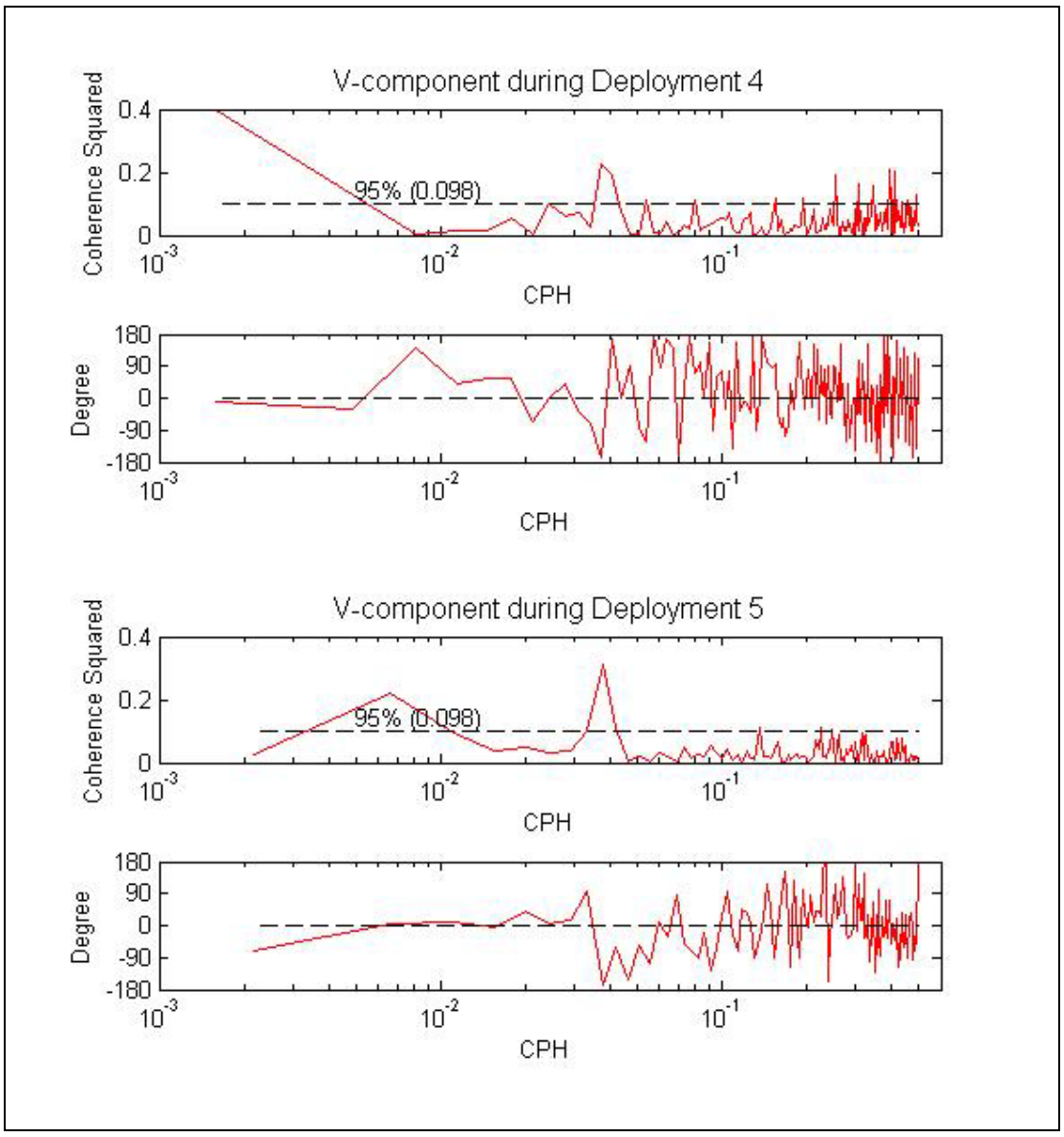

Figure 2-11. Coherence and phase between top (250 m) and bottom (3004 m in Deployment 4 and 3000 m in Deployment 5) V-component during Deployments 4 and 5.

CHAPTER 3

LC, LCE, AND THE DEEP CIRCULATION

3.1 Model Simulations

In previous models of the deep circulation using the Bryan-Cox Model, later called the Modular Ocean Model (MOM), with horizontal grid resolution ranging from .25 º (Sturges et al. 1993) to .1º (Welsh and Inoue 2002), an eddy pair, or modon, is observed to form in the eastern GOM beneath the LC as a ring forms. The deep eddy pair then propagates westward as the LC ring migrates westward in all versions of the model. The first model with .25º horizontal resolution had only two 900-m vertical levels below 1820 m, which reduced the slope to nearly vertical walls. There was no rise, no bottom topography, and no deep constriction between 87ºW and 89ºW (Sturges et al. 1993). The deep eddy pair was not constrained by the bathymetry and maintained the general shape of a modon as it migrated westward. The next version of the model had 3 times the vertical resolution below the sill depth and 2 times the horizontal resolution (Welsh and Inoue 2000). The slope and the deep constriction were both represented on the 1/8 º grid, as well as a much better representation of the Yucatan sill. The eddy pairs formed in the eastern basin, squeezed through the constriction, and reformed in the deep central basin (Welsh and Inoue 2000). There was considerably more eddy activity in the eastern basin as well as the western basin due to eddy-eddy and eddy-slope interactions that were now possible to simulate due to the greater horizontal and vertical resolution. The next version of the model had .1º horizontal resolution and 20 vertical levels. The increase in vertical resolution was confined to the upper layer, and the vertical grid spacing in the deep layer was again 300 m. The small increase in horizontal grid spacing resulted in increased eddy activity in the eastern basin, making it difficult to isolate the eddy components of the deep modon beneath the LC in the upper layer. The eddy pairs were distorted as they passed through the deep constriction and were not identifiable until the LC ring migrated west of 90ºW. For all of the grid resolutions, it is often difficult to isolate the eddy pairs in snapshots of the deep velocity field, but animations of model velocity make it possible to identify and follow the eddy pairs as they migrate westward.

These latest model simulations feature .075º horizontal grid resolution (7.55 km by 8.33 km at 25ºN) and 100 levels in the vertical. The vertical grid spacing is 20 m above the shelf break and 40 m below. It should be noted that for the first time the high vertical resolution grid effectively can represent the gentle rise and the steep escarpments, as well as the intricacies of the Yucatan Sill bathymetry. Three east-west cross-sections of the grid in the eastern basin are presented in Figure 3-1. The Catoche Tongue and the entrance to the Southern Straits of Florida are evident in the cross-section at 23.5ºN. The Florida Plain is bounded by the Campeche Terrace to the west and the west Florida escarpment to the east along 24.25ºW. Along the cross-section at 25ºN, the eastern basin opens up to the deep constriction at 87ºW. The smaller grid spacing in both the horizontal and vertical are necessary to resolve deep eddy interaction with the bathymetry. It will be demonstrated below that eddy interaction with the bathymetry creates a very chaotic eddy field in the eastern basin. The eddy ‘pairs’ appear as distinct regions of anticyclonic and cyclonic vorticity that form beneath the LC as it penetrates northward and sheds an eddy. Interaction with the bathymetry causes stretching and compression of the deep eddies, which results in an increase or decrease of the eddy vorticity.

As mentioned earlier, the leading anticyclone in the deep layer is easily identifiable in all of the simulations of LC ring formation (Sturges et al. 1993; Welsh and Inoue 2000; Welsh and Inoue 2002). In the higher resolution models, the area behind the leading anticyclone is populated by eddies that are highly ephemeral. As the LC begins to intrude northward, a cyclone typically forms off the West Florida escarpment and then moves southward and westward along the eastern edge of the leading anticyclone. Sometimes the cyclones appear to be absorbed by the leading anticyclone and other times they dissipate in the narrow region on the northern side of the Yucatan Channel. After the leading anticyclone moves into the deep constriction between 87ºW and 89ºW, the circulation in the southeastern GOM breaks up into a chaotic eddy field populated by both cyclones and anticyclones. Chérubin et al. (2005) observed this process using the MICOM model to study the deep circulation in the eastern GOM. Chérubin et al. (2005) attribute the leading anticyclone to the 'deepening of the active layer underneath the LC ring' and observe in the model that three or four cyclones form around the deep anticyclone. Due to topographic interaction, one or two cyclones dissipate and the other one or two rotate around the deep anticyclone. One of the cyclones will gain vorticity and balance the anticyclone within the structure of the modon. The formation of the modon pair described by Chérubin et al. (2005) is very similar as the process that occurs in this high resolution model.

The series of images in Figure 3-2 depict the deep velocity field during a typical ring separation. On day 1, an anticyclone appears over the flat sea floor of the Florida Plain as the LC begins to push northward in the eastern basin. An elongated anticyclone bridges the gap between the trailing cyclone associated with the previously shed LC ring, and a newly formed deep anticyclone is present on days 1 and 40. As the LC front extends northward on day 60, the leading anticyclone coalesces with the anticyclone positioned over the deep constriction. Although the leading anticyclone changes shape, size, and orientation, it is generally centered beneath the northwestern (leading) section of the LC. On day 80 the leading anticyclone appears to separate into two circulation cells – one over the constriction and another aligned with the center of circulation of the LC. A deep cyclone has formed on day 40 up against the Florida Escarpment at 26ºN. By day 60 the cyclone has moved southeast and nearly fills the deep Florida Plain, and an anticyclonic feature has begun to form just to the north of it. On day 80, the cyclone has become landlocked and the anticyclonic feature has strengthened and moved south. The anticyclonic feature moves westward on day 100 and again appears to coalesce with the leading anticyclone. The entire deep region adjacent to the Florida Escarpment is dominated by cyclonic circulation on day 100. When the LC moves northward over the Mississippi Fan on day 120, the leading anticyclone moves up over the Sigsbee Escarpment and is not visible at 2580 m, but it is clearly visible in velocity field at 1800 m (Figure 3-3). The strong interaction of the trailing cyclone with the Catoche Tongue can also be seen on day 120 (Figures 3-2 and 3-3). On day 140 the center of circulation of the LC has moved over the deep constriction and the deep eddy field appears chaotic. The LC ring has separated on day 160 and the leading anticyclonic and trailing cyclonic features are identifiable. On day 180 the cyclonic feature has moved westward with the surface expression of the newly formed LC ring and anticyclonic circulation has begun to dominate the deep eastern basin again. On day 220 the process begins to repeat itself.

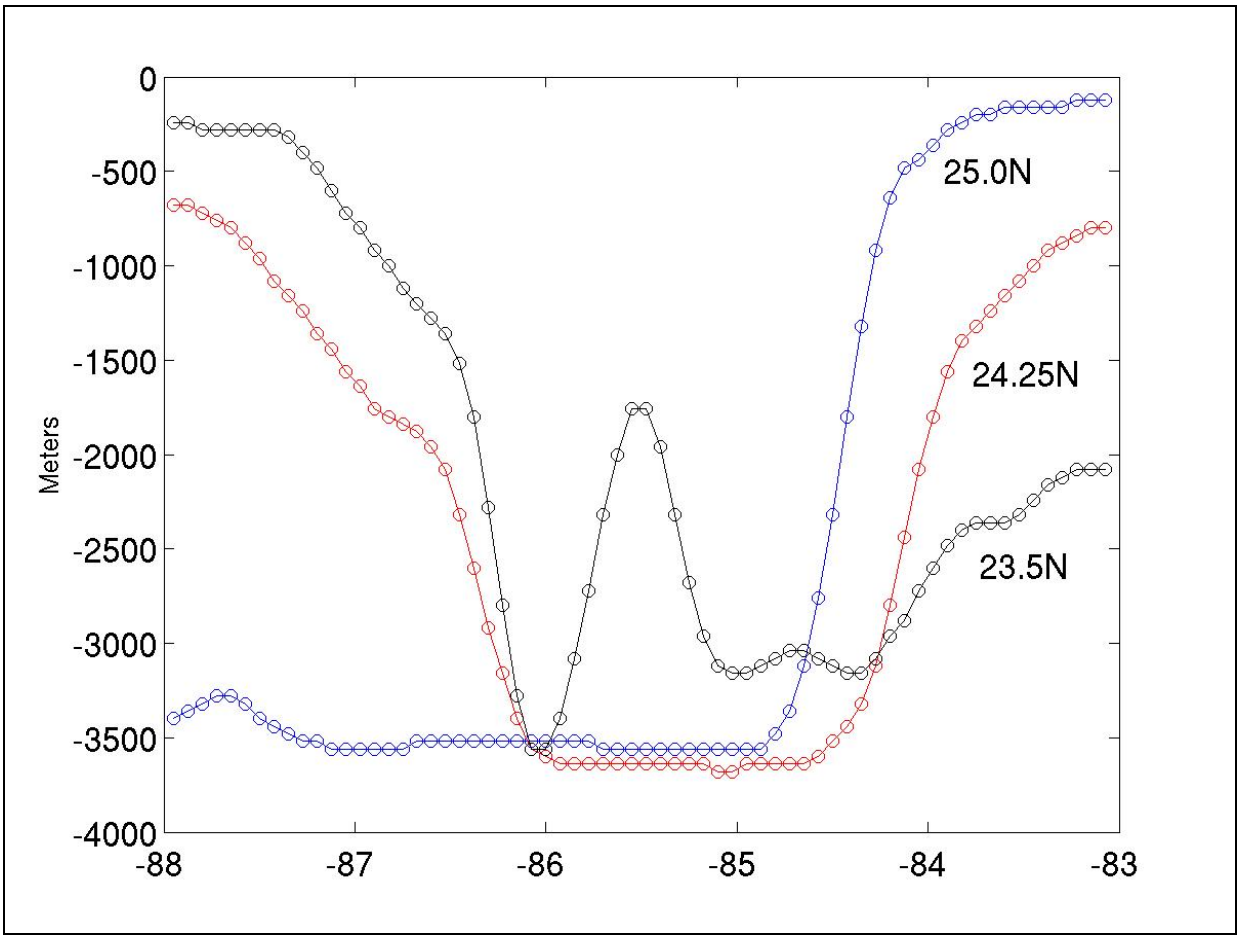

Figure 3-1. East-west cross-sections of the model grid in the eastern GOM. Each circle represents the longitude and depth of a model grid cell along the designated latitudes.

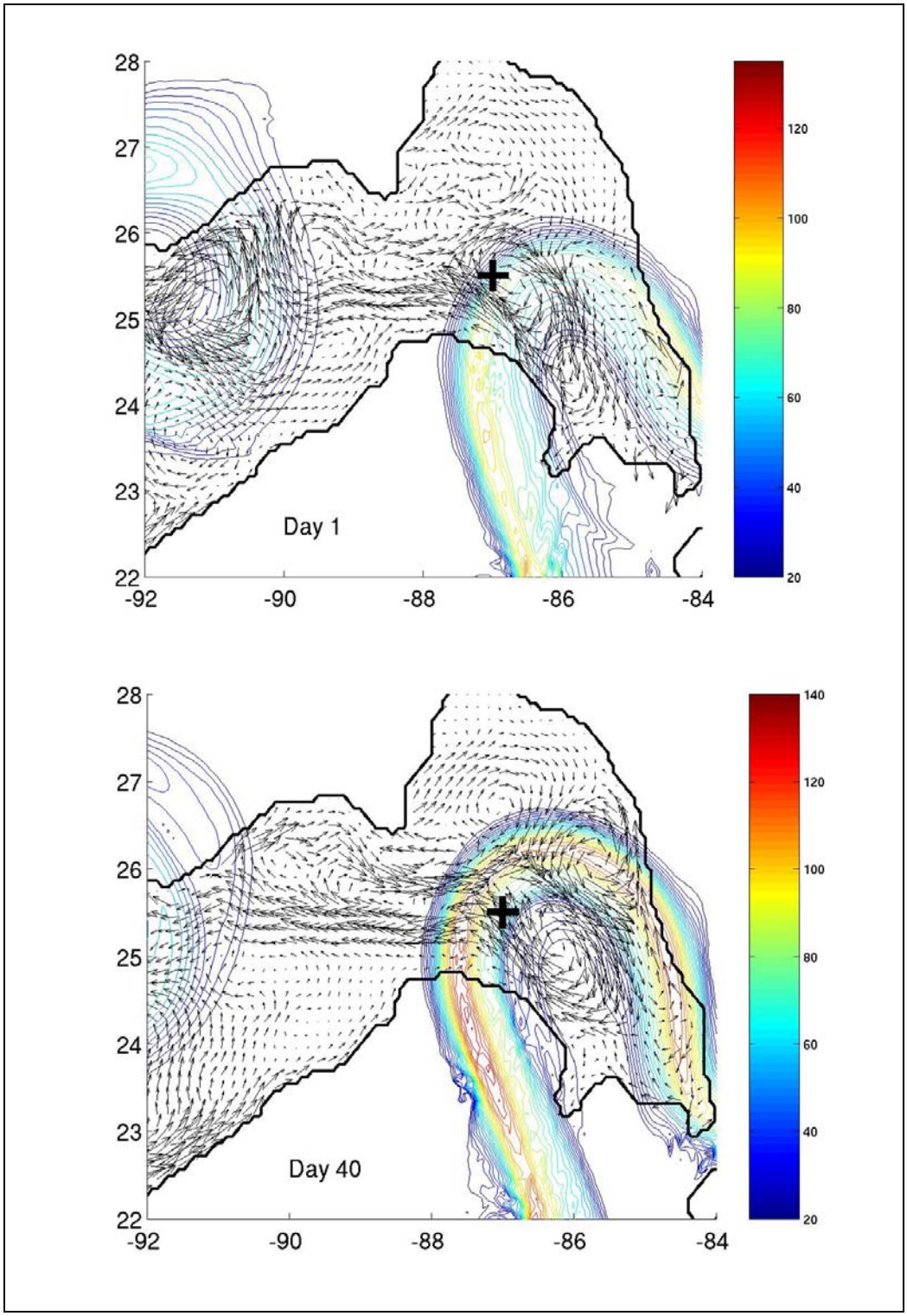

Figure 3-2. Velocity vectors at 2580 m (level 70) and contours of velocity magnitude (color bar units in cm s^{-1}) at 10 m (level 1) for the specified model days. The mooring location is marked with a '+'.

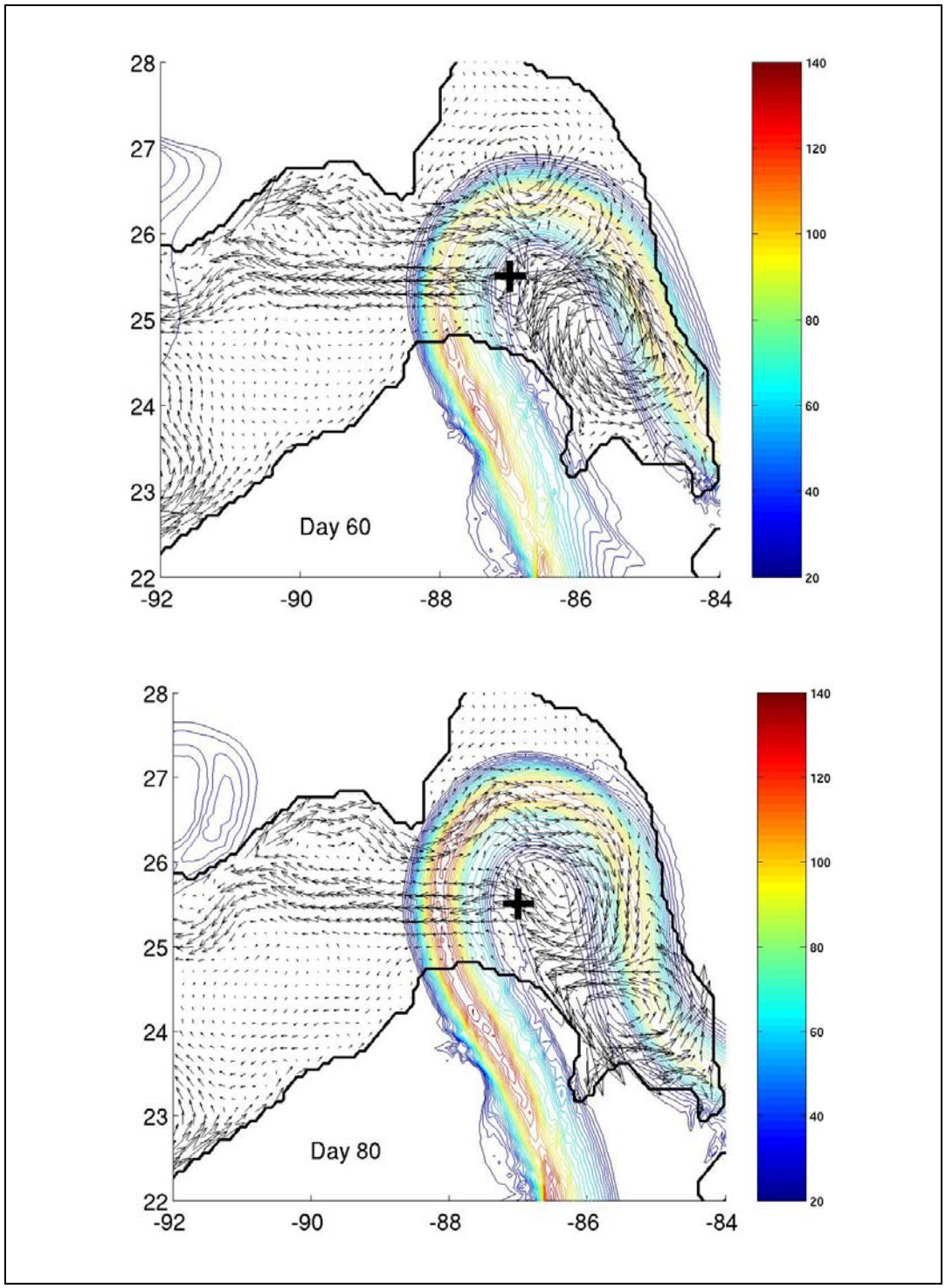

Figure 3-2. Velocity vectors at 2580 m (level 70) and contours of velocity magnitude (color bar units in cm s^{-1}) at 10 m (level 1) for the specified model days. The mooring location is marked with a '+' (continued).

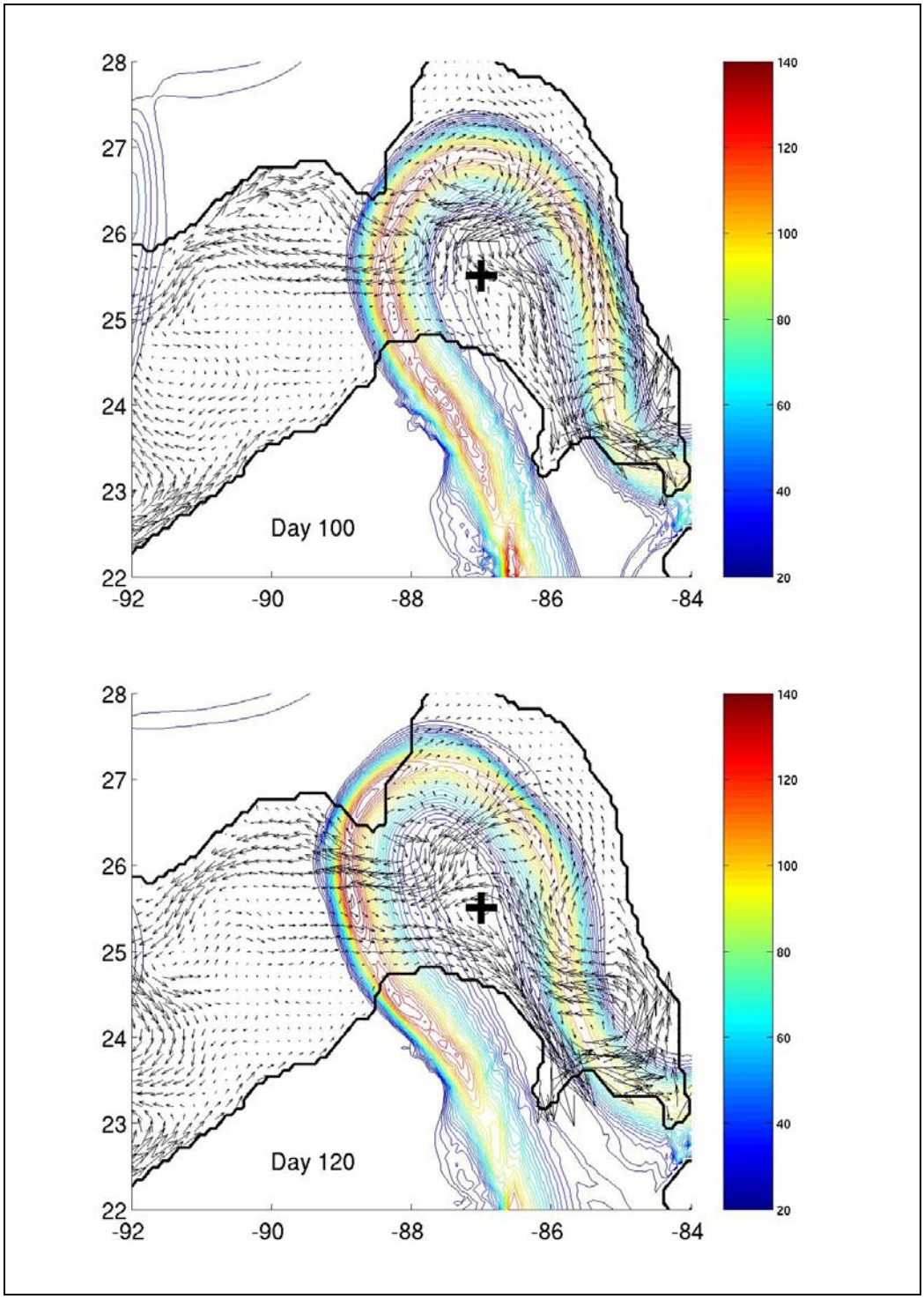

Figure 3-2. Velocity vectors at 2580 m (level 70) and contours of velocity magnitude (color bar units in cm s^{-1}) at 10 m (level 1) for the specified model days. The mooring location is marked with a '+' (continued).

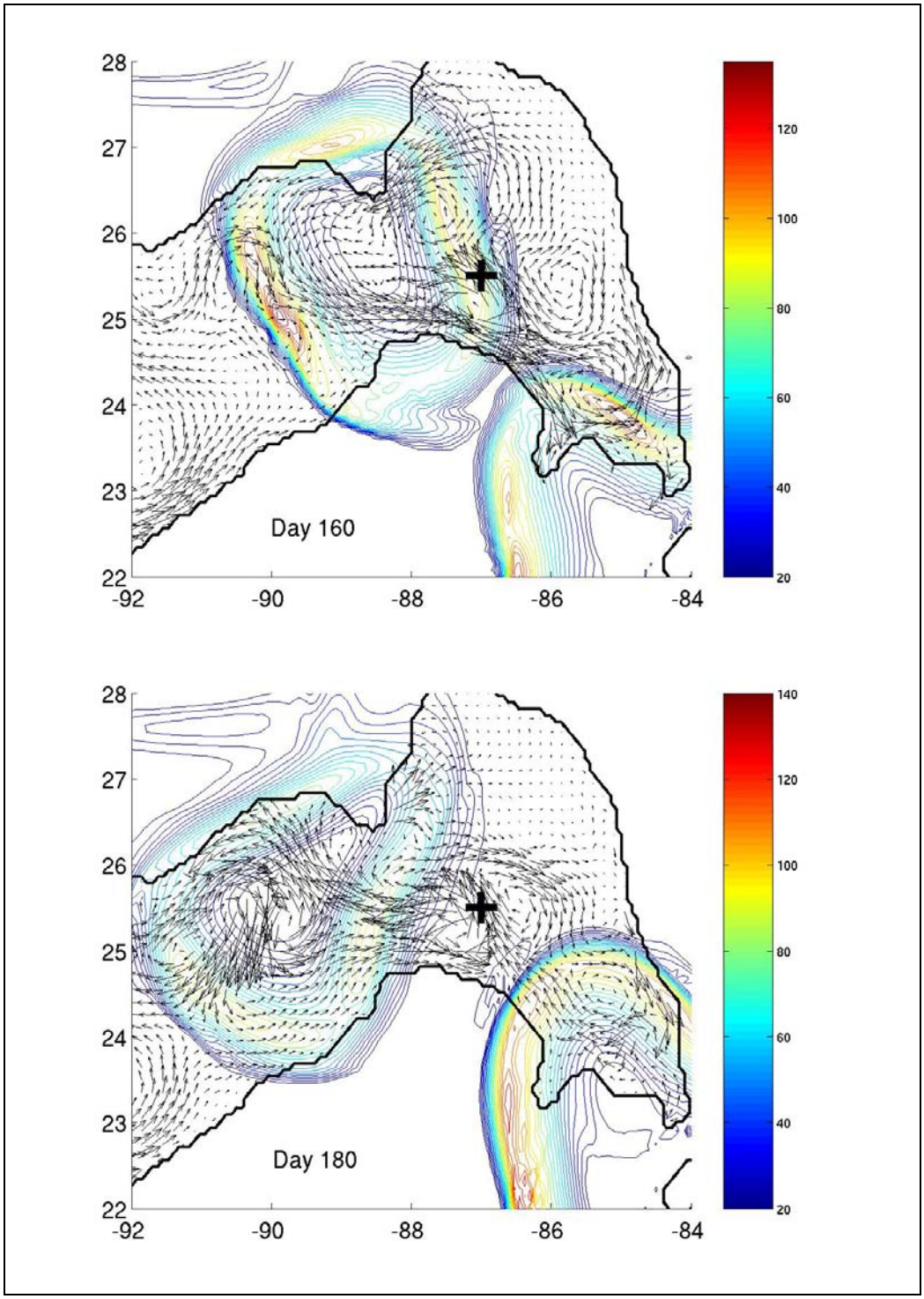

Figure 3-2. Velocity vectors at 2580 m (level 70) and contours of velocity magnitude (color bar units in cm s^{-1}) at 10 m (level 1) for the specified model days. The mooring location is marked with a '+' (continued).

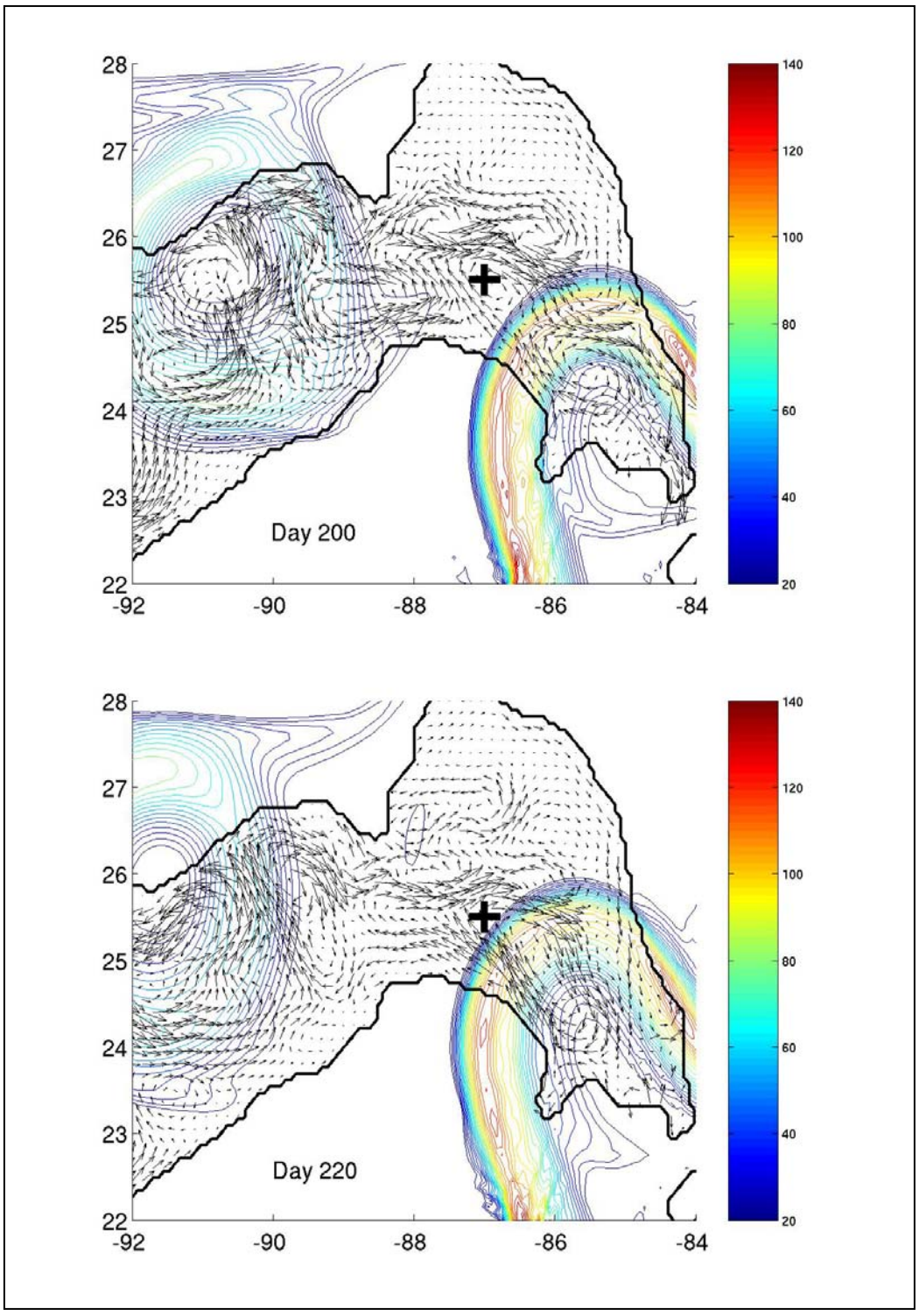

Figure 3-2. Velocity vectors at 2580 m (level 70) and contours of velocity magnitude (color bar units in cm s^{-1}) at 10 m (level 1) for the specified model days. The mooring location is marked with a '+' (continued).

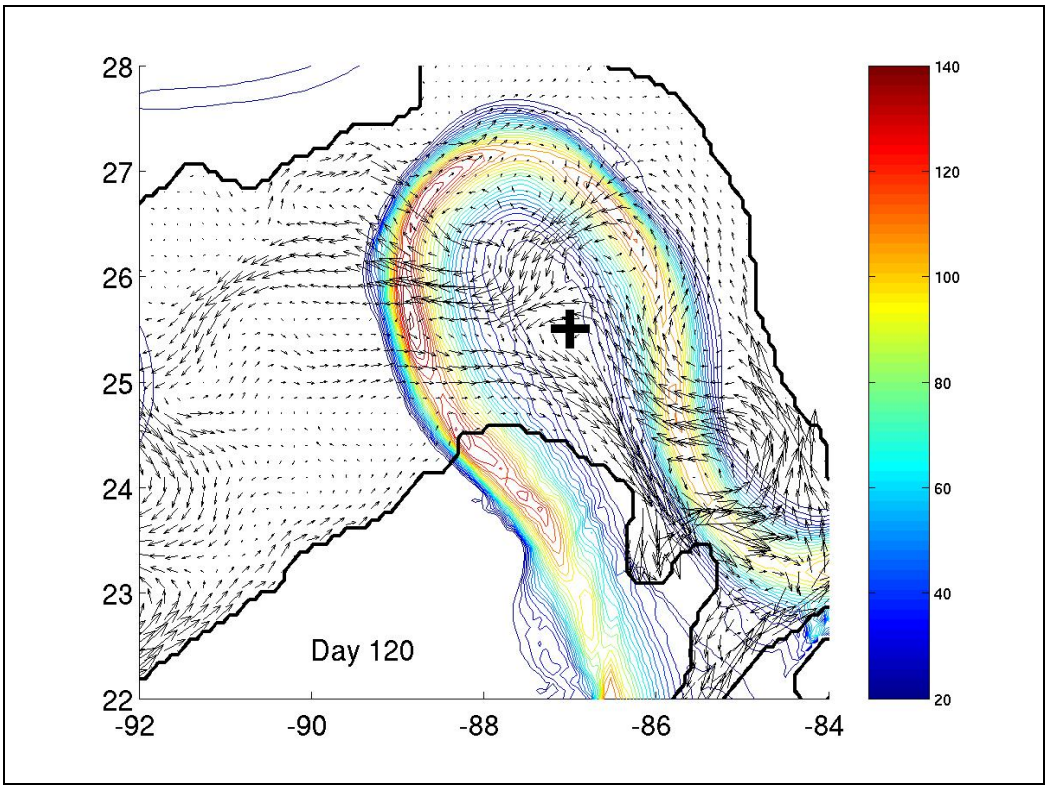

Figure 3-3. Velocity vectors at 1780 m (level 50) and contours of velocity magnitude (color bar units in cm s^{-1}) at 10 m (level 1) for the specified model day. The mooring location is marked with a plus sign.

Closer examination of the manifestation of the LC on the deep eddies as a function of the model grid resolution has provided the insight as to why the modons don't tend to reform in the western basin in this high resolution model. In previous versions, the eddy pairs only regained the characteristic modon shape if the LC ring migrated southwestward over the flat abyssal plain. When the LC ring migrated along the northern slope, the eddy pair became distorted and was hard to distinguish from the background eddy field. The LC rings in this high resolution model follow nearly the same path and migrate westward along the Texas-Louisiana slope. It is noted that because of the similarities in the model representation of the upper layer dynamics between this model and the older versions of the model, the LC behaves similarly while this is not true for the deep layer dynamics which is much better simulated in this version. The associated deep eddy pairs strongly interact with the slope and only the southern portion of each eddy pair is visible below 2500 m. In the animations of the deep velocity field, the western basin is populated by eddies that are constantly moving, coalescing, splitting, forming and decaying. The lifespan of the western eddies is on the order of weeks to months. The eddy field circulates counter clockwise in the western basin beginning at the constriction and dissipating over the Campeche Escarpment. The counter-clockwise tendency for deep eddy movement is indicated by tracking the center of circulation of eddies and is most apparent in the animations of velocity maxima. Deep cyclonic circulation was observed in the motion of inert particles in the .1º resolution model (Welsh and Inoue 2002). The cyclonic deep circulation is visible in the mean velocity field (Figure 3-4) in this model as well as the .1 º resolution model. The deep cyclonic circulation was deduced from historical temperature data, deep current measurements in the eastern GOM, and PALACE floats in the central GOM (DeHaan and Sturges 2005; Sturges et al. 2004).

The formation of modons as the interface moves up and down with the northward penetration of the LC and subsequent shedding of LC rings was clearly visible in the coarse resolution models. As the model grid resolution increases, so does the eddy-eddy interaction and the eddy-topographic interaction. How do we know that the process of modon formation is occurring in the high resolution model when the eddy field is so crowded and chaotic? As long as the surface expression of the LC ring remains far enough off the slope, the boundary between the anticyclonic and cyclonic circulation remains nearly fixed relative to the leading edge of the LC ring until the LC ring is in the western GOM. The boundary between the regions of anticyclonic and cyclonic flow is characterized as a southward jet. In all of the models with varying grid sizes, after a LC ring has migrated into the western GOM, the leading deep anticyclone dissipates first and the circulation becomes dominated by the deep cyclone. The effect of the westward migration of the deep eddy field is the net transport of vorticity into the western basin.

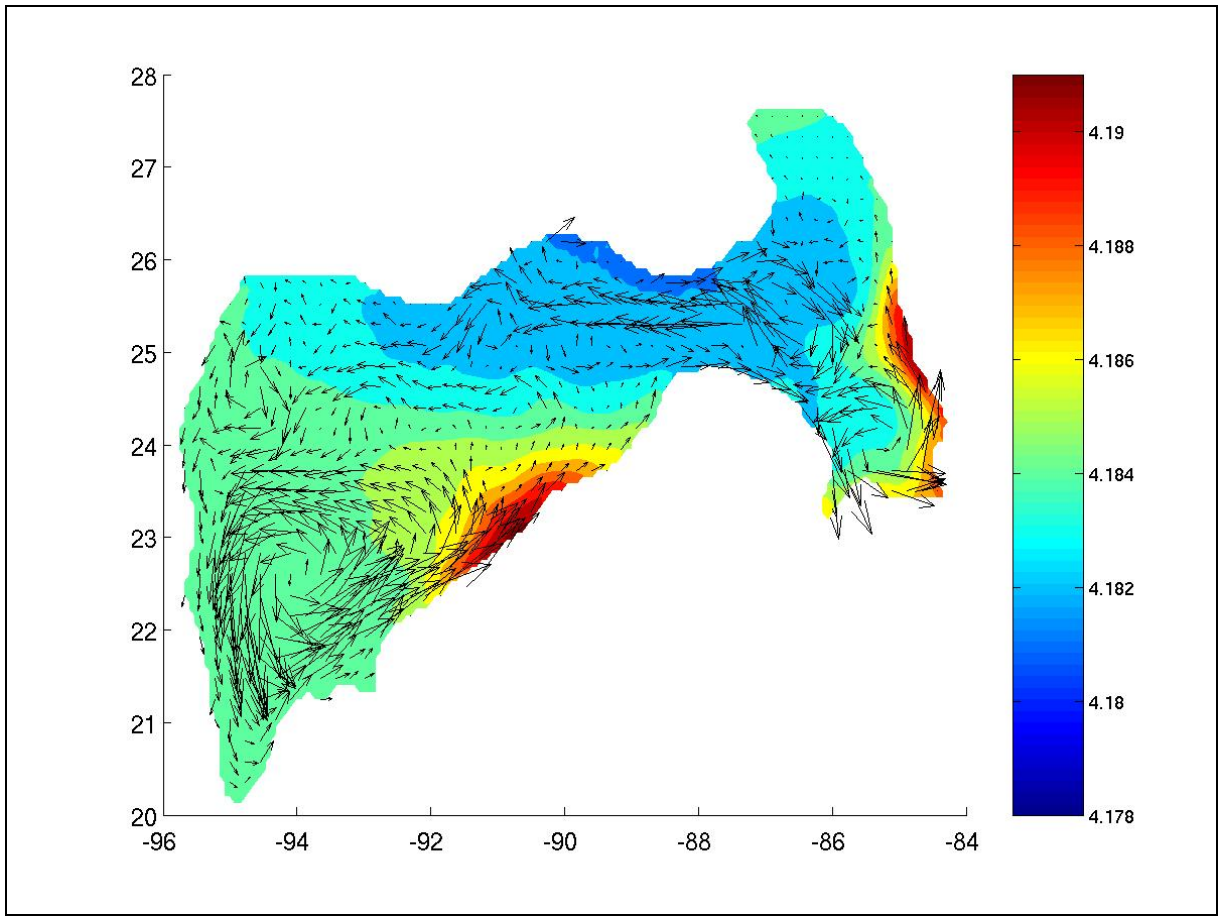

Figure 3-4. 4-year average model temperature (color bar units in ^{o}C) and velocity vectors at 3000 m (level 80).

3.2 Evidence of Deep Modon Formation in the Mooring Data

Does the deep water mooring data support the concept of modon formation that we observe in the model velocity fields? We learned from the model that the direction of the flow should reverse at the mooring location as deep eddies move past it. Do we see these reversals in the deep velocity field at the mooring location? The answer is yes. To examine the relationship of the deep currents at 87ºW, 25.5ºN to the eddy shedding cycle, altimetry data was used to create a database of LC ring shedding events. The stages of the LC ring separation process are compared to the timing of current reversals recorded by deep current meters during each deployment. Altimetry data for the beginning of the first deployment (5/31/00) to near the end of the 4th deployment (5/27/06) was examined using the animation of SSH images produced by Bob Leben at CCAR and presented at the USA-Mexico Workshop on the Deepwater Physical Oceanography of the Gulf of Mexico in June, 2007. The remaining images (5/27/06 through 7/10/07) were downloaded from the CCAR Near Real-Time Altimetry Data Homepage (http://argo.colorado.edu/~realtime/gsfc_gom-real-time_ssh/). The dates of each separation, near separation, reattachment and near reattachment were recorded for the time span covering all 5 deployments. The names of the LC rings or eddies were verified using both the table of named LCEs on the Horizon Marine web page (http://www.horizonmarine.com/namedlces.html) and from the table of ring separation events for 1993-2004 constructed (Leben 2005). The date of each south to north reversal of the deep currents is presented in Table 3-1 along with the dates of each stage of LC ring separation. The dates are highlighted to illustrate the temporal relationship between the deep current reversals and the near or complete separation of a LC ring. There is a current reversal prior to nearly every partial or complete separation of a LC ring. The only exceptions are on 8/3/03, 9/17/05, and 4/17/07. During these dates there was a change in the deep flow, but the direction or the timing of the event was somewhat different from the other events. LC rings vary greatly in size, intensity, and geographical location of separation compared to the model counterparts (Leben 2005). The SSH from satellite altimetry for the dates of each LC ring final separation during the 5 deployments is presented in Figure 3-5. These images illustrate the extreme variability of the ring separation process.

Table 3-1

Timeline of Deep Current Reversals and LC Ring Separation Events

Dates of South to North Reversals of Deep Currents	Dates of LC Ring Separations and Attachments	Name of LC Ring	Intermediate Stages
Deploy Mooring #1 5/31/00			
	6/15/00	Kinetic	Final Separation
1/20/01			
	1/28/01	Millenium	1st Separation
	1/30/01	"	1st Reattachment
3/13/01			
	4/13/01	"	Final Separation
Recover Mooring #1 8/1/2001 Deploy Mooring #2 8/3/2001			
9/1/01			
	9/9/01	Odessa / Nansen	1st Separation
	9/13/01	"	1st Reattachment
	9/22/01	"	Final Separation
2/1/02			
	2/28/02	Pelagic	Final Separation
3/13/02			
	3/14/02	Quick	Final Separation
Recover Mooring #2 6/3/02 Deploy Mooring #3 4/19/03			
7/12/03			
	7/13/03	Saragassum	1st Separation
	7/20/03	"	1st Reattachment
8/3/03 *			
	8/5/03	Sargassum	Final Separation
9/26/03			
	9/26/03	Titanic	1st Separation
	11/29/03	"	1st Reattachment
12/24/03			
	12/31/03	"	2nd Separation
	2/3/03	"	2nd Reattachment
2/13/04			
	2/16/04	"	Final Separation

Table 3-1. Timeline of Deep Current Reversals and LC Ring Separation Events (continued).

Recover Mooring #3 6/1/04 Deploy Mooring #4 5/29/05			
6/6/05			
	6/16/05	Vortex	3rd Separation
	6/30/05	"	3rd Reattachment
8/5/05			
	8/5/05	"	4th Separation
	8/20/05	"	4th Reattachment
9/17/05 **			
	9/18/05	Vortex	Final Separation
12/12/05			
	12/22/05	Walker	Near Separation
	1/16/06	"	Near Separation
	2/10/06	"	Final Separation
3/1/06			
	3/7/06	Xtreme	1st Separation
	4/10/06	"	1st Reattachment
4/1/06			
	5/6/06	"	Final Separation
Recover Mooring #4 5/25/06 Deploy Mooring #5 6/17/06			
7/5/06			
	7/14/06	Yankee	1st Separation
	7/26/06	"	1st Reattachment
7/31/06			
	8/4/06	"	Near Separation
9/14/06			
	9/23/06	"	Near Separation
9/28/06			
	9/29/06	"	2nd Separation
	10/9/06	"	Weak Reattachment
10/31/06			
	11/4/06	"	Final Separation
	4/13/07	Zorro	1st Separation
4/17/07 ***			
	6/1/07	"	1st Reattachment
Recover Mooring #5 7/10/07			

Exceptions:
* The northward surge from 8/3/03 to 8/5/03 was not preceded by southerly flow.
** The current direction changed from southerly to westerly.
*** The reversal occurred 4 days after the separation of Zorro.

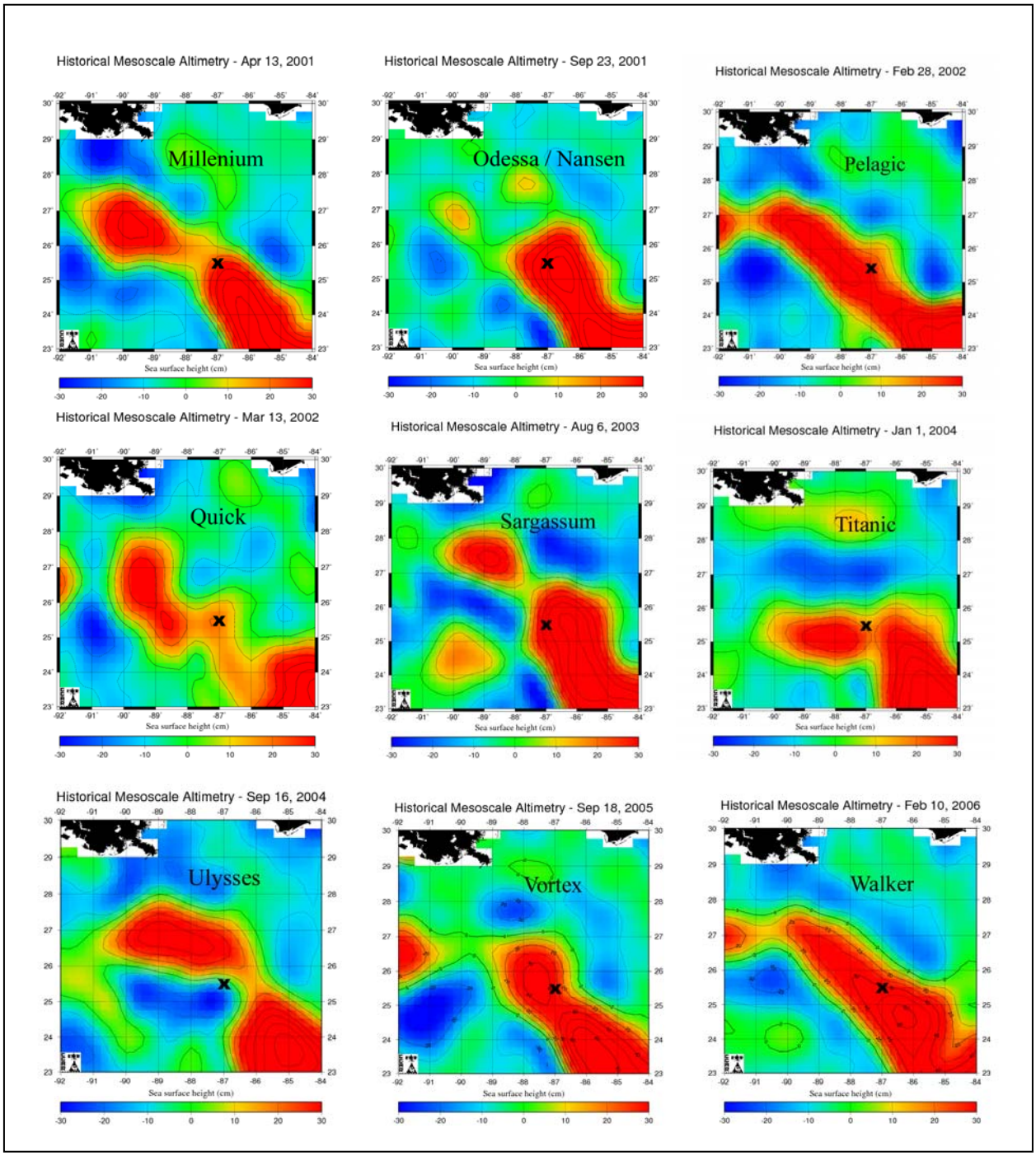

Figure 3-5. Sea surface height maps for dates corresponding to LC ring separations plotted from historical mesoscale altimetry data archived by Dr. Robert Leben at the University of Colorado. The mooring location is indicated by an **X**.

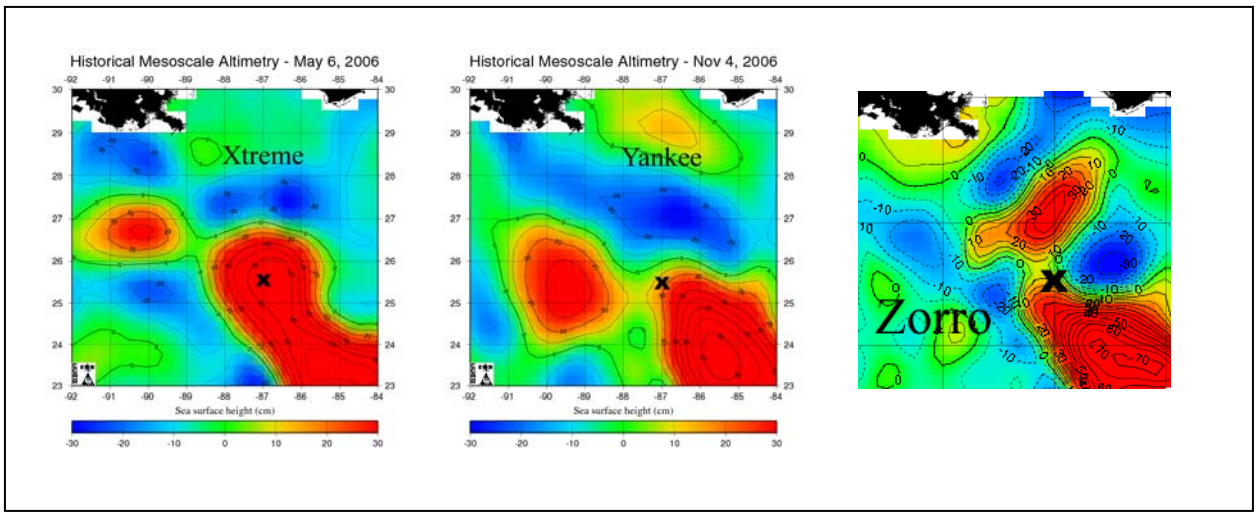

Figure 3-5. Sea surface height maps for dates corresponding to LC ring separations plotted from historical mesoscale altimetry data archived by Dr. Robert Leben at the University of Colorado. The mooring location is indicated by an **X** (continued).

3.3 Locating the Interface between Upper and Lower Layers

A two-layer approximation, that appears to characterize the flow field observed by the mooring, is considered here to locate the interface between the upper- and lower-layers. One way to visualize the two-layer approximation that can be applied to the region is to examine the vertical profile of the first baroclinic mode computed for the water stratification observed at the mooring site. The first baroclinic mode shown in Figure 3-6 appears to represent the vertical profile of the observed currents at the mooring site well, i. e., the upper-layer flow shows notable vertical shear while the lower-layer flow exhibits nearly barotopic flow with the zero-crossing located near 830 m. If one takes the zero-crossing of the first baroclinic mode as the interface between the upper- and lower-layers, current speed near the interface should be minimal. Consequently, the shortest progressive current vector is expected near the interface depth. Progressive current vector diagrams for Deployments 4 and 5 are plotted in Figure 3-7. It is evident that during Deployment 4, transition between the upper- and lower-layers appears to be located between 750 m and 875 m, above and below which flow regime shifts from the upper-layer flow with a predominant long-term southeast-ward drift to the lower-layer flow characterized by a slow northward drift. During Deployment 5, the upper-layer flow represented by currents at 600 m exhibits a tendency to drift north-northeasterly while the lower-layer flow, represented by currents observed at 3000 m and 1500 m, displays a northward drift. Currents between 775 m and 1015 m appear to be in the transition between the upper- and lower-layers. The difference in the direction of the upper-layer drift between Deployments 4 and 5 is the consequence of the differences in the location of the mooring relative to the LC. During Deployment 4, the mooring was primarily located on the eastern side of the LC while it was situated on the western side of the LC during Deployment 5.

It should be noted that unlike a two-layer system that by theory maintains a sharp interface between the upper- and lower-layers, transition between the two layers observed by the mooring extends from ~800 m to ~1000 m. Moreover, during all the cruises for this project, the mooring was always found to be located inside the warm upper-layer water associated with the LC or LCEs. However, the mooring data indicate that the mooring occasionally moved out of the warm upper-layer water. It is conceivable that when the mooring moved out of the warm upper-layer water, the interface could have moved upward. Thus, identification of a sharp interface is not expected. It is interesting that the zero-crossing of the first baroclinic mode (Figure 3-6) is located close to the sill depth (~800 m) at Strait of Florida, a confirmation that within the LC the warm water in the upper-layer flows from the Yucatan Channel to Florida Strait uninterrupted (e. g., Bunge et al. 2002).

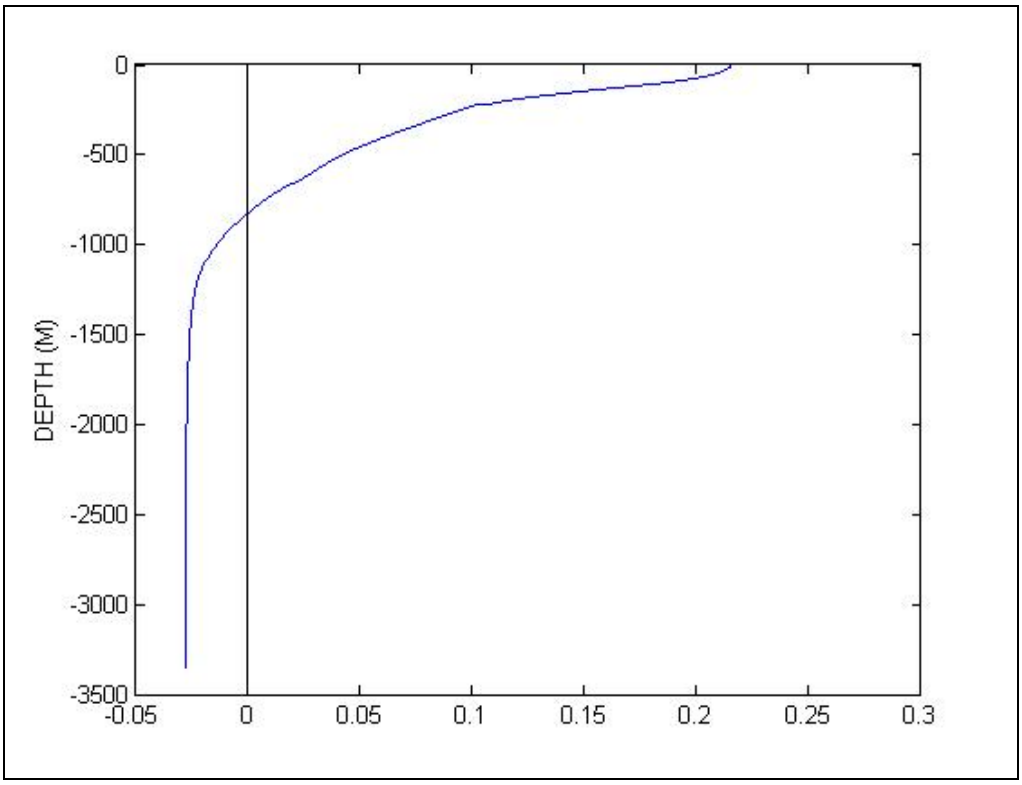

Figure 3-6. Vertical profile of the first baroclinic normal mode computed for the mooring site using the mean temperature and salinity profiles sampled by CTD stations taken during the first three deployments. Replotted from Figure 2-7 of Inoue et al. (2008).

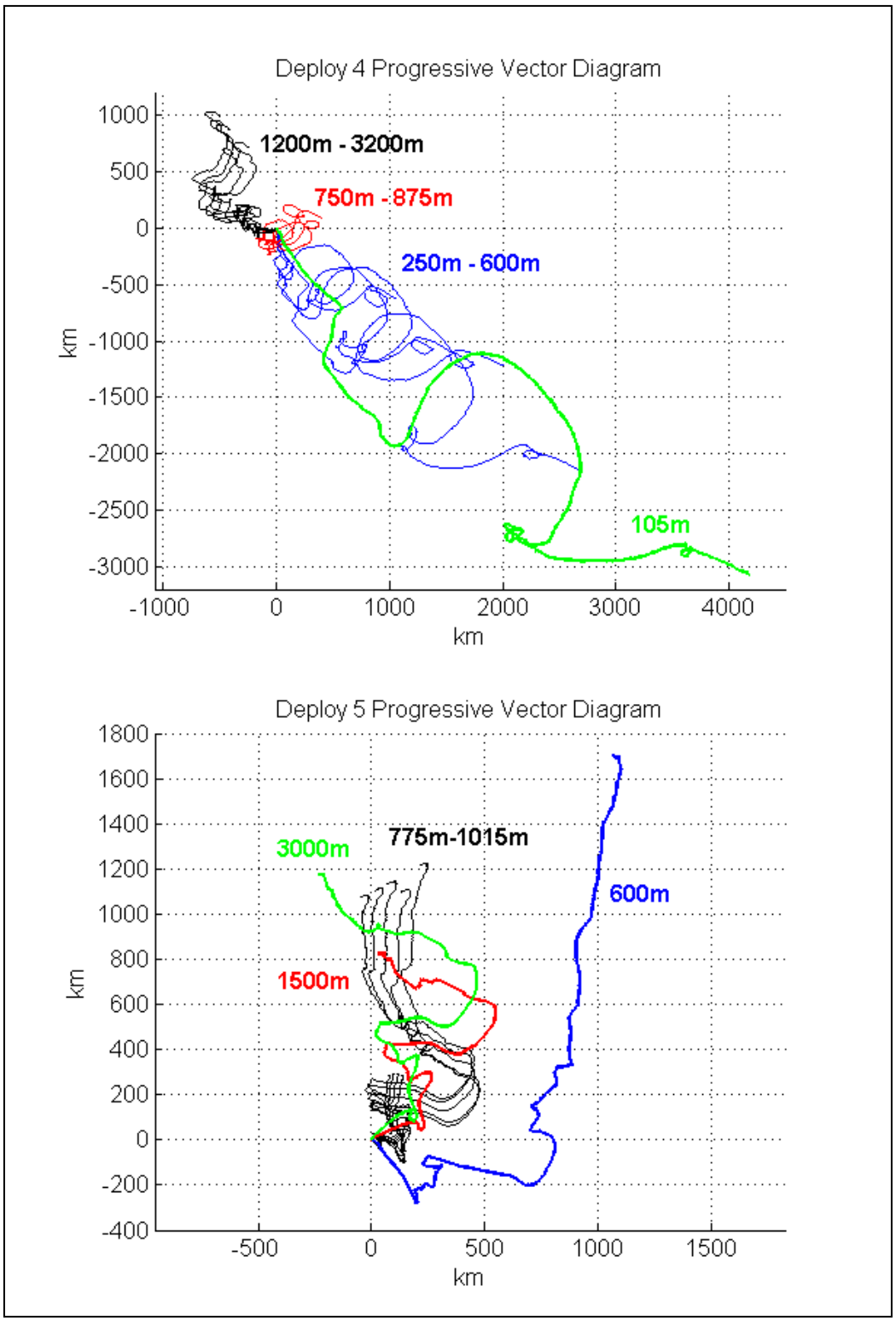

Figure 3-7. Progressive vector diagrams for the longest common record lengths for Deployment 4 (5/30/05-2/12/06) (top) and Deployment 5 (6/18/06-3/20/07) (bottom). Depths are indicated.

3.4 Temperature Variability in Deep Water

Using the numerical model to interpret the deep current reversals, we infer from the table that the mooring is capturing the passage of deep eddies which form as the LC extends northward in advance of the separation of a ring. The interface deepens when the LC moves over the mooring, which would inevitably push downwards and compress the lower layer. During Deployments 4 and 5 we had adequate vertical spacing of Microcats in the lower layer to monitor how the stratification in the deep water responds to the surface layer forcing. The average temperature gradient over the entire water column sampled by the mooring is presented in Figure 3-8. Although the lower layer is weakly stratified, we can see from the average vertical temperature gradient in deep water that if the deep layer was compressed, the water above the temperature inflection at 2000 m would become warmer and the water below that would become cooler. If the deep layer was stretched, the water above the temp minimum would become colder and the water below would become warmer. Hence, temperature variations above and below the temperature minimum should be out-of-phase. The depth-corrected temperature record (corrected for blow-over) for Deployments 4 and 5 is presented in Figure 3-9. For example, in the first part of June 2006, the interface is depressed corresponding to the LC Eddy Yankee sitting on top of the mooring (Figure 3-10) and warming is indicated above the temperature minimum near 2000 m, whereas in the latter part of July 2006, when the LC Eddy Yankee moved away from the mooring (Figure 3-10) and the interface moved upward, corresponding cooling above the temperature minimum near 2000 m is evident (Figure 3-9).

The out-of-phase relationship between temperatures above and below the temperature minimum near 2000 m can be seen in the depth-corrected standardized temperatures at 1500 m and 1800 m and those at 1500 m and 3000 m (Figure 3-11). Temperatures at 1500 m and 1800 m are in phase while those at 1500 m and 3000 m are clearly out-of-phase. It is not possible to systematically correlate the lower layer compression with the exact timing of ring separations, since the LC is almost never in the same position relative to the mooring when a ring separates (refer to Figure 3-5). Also, as mentioned above, the rings themselves vary greatly in size and shape. Even so, the mooring data clearly shows compression of the lower layer when warm surface water related to LC or LCE is located at the mooring site, while stretching of the lower layer is evident when cooler surface water is located at the mooring site.

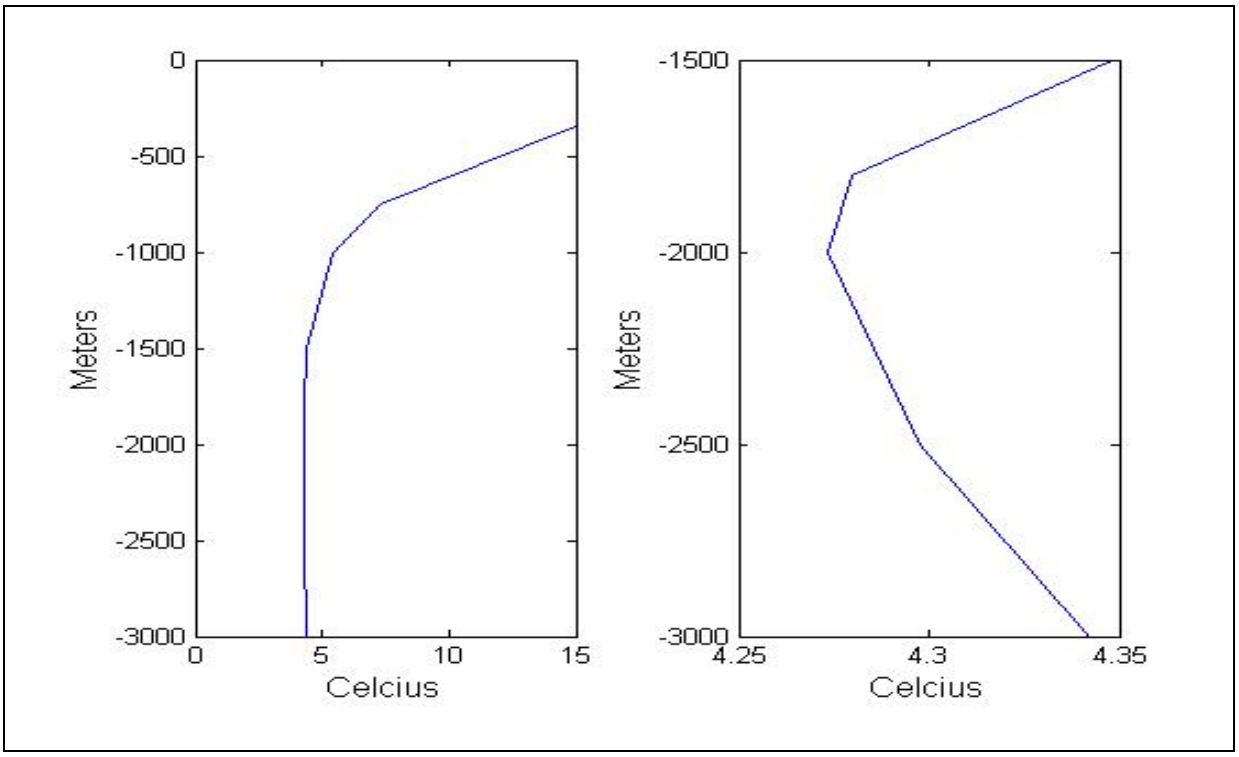

Figure 3-8. Mean vertical temperature gradient for Deployments 4 and 5.

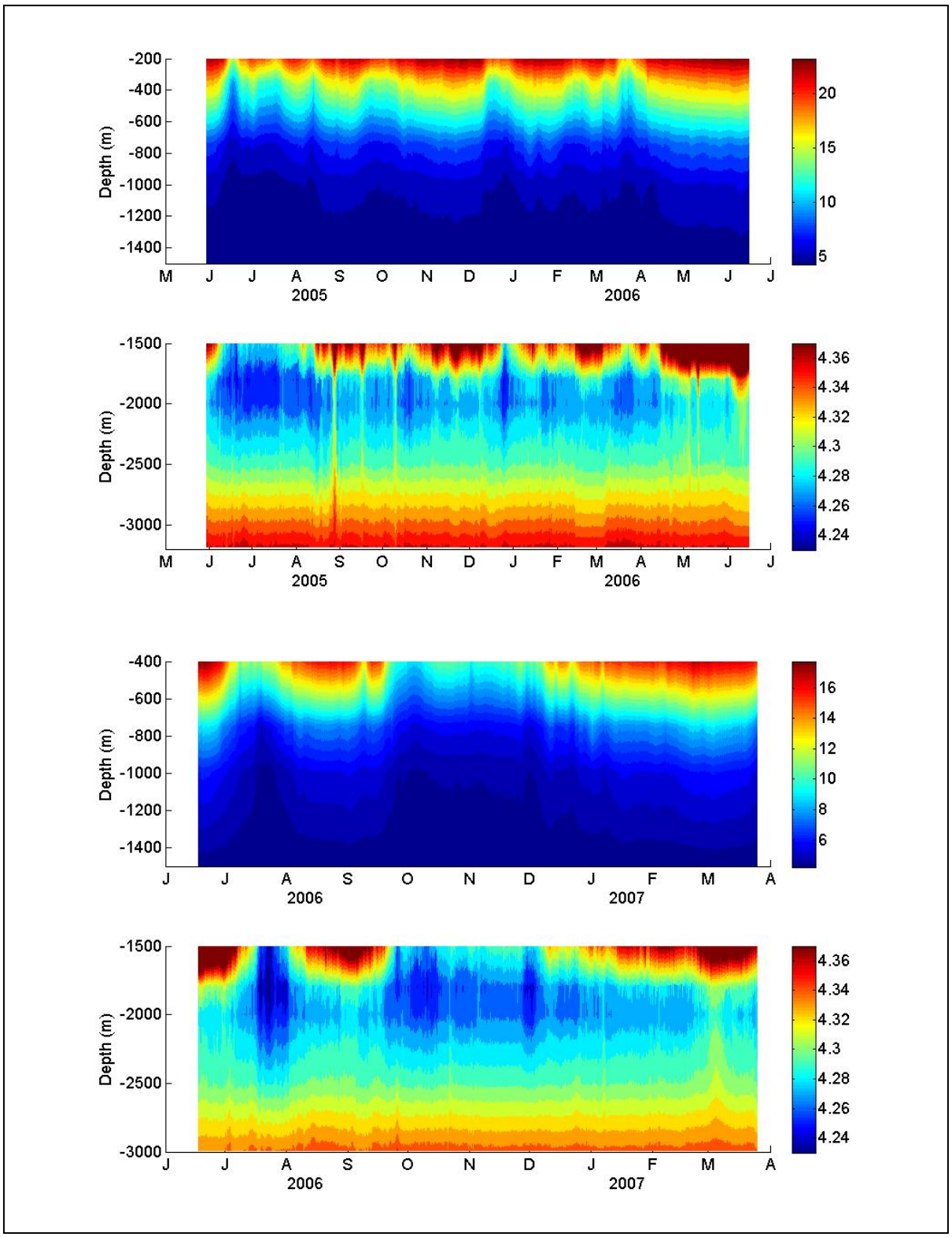

Figure 3-9. Contours of temperature (color bars in ^{o}C) corrected for blow over during Deployment 4 (top) and Deployment 5 (bottom).

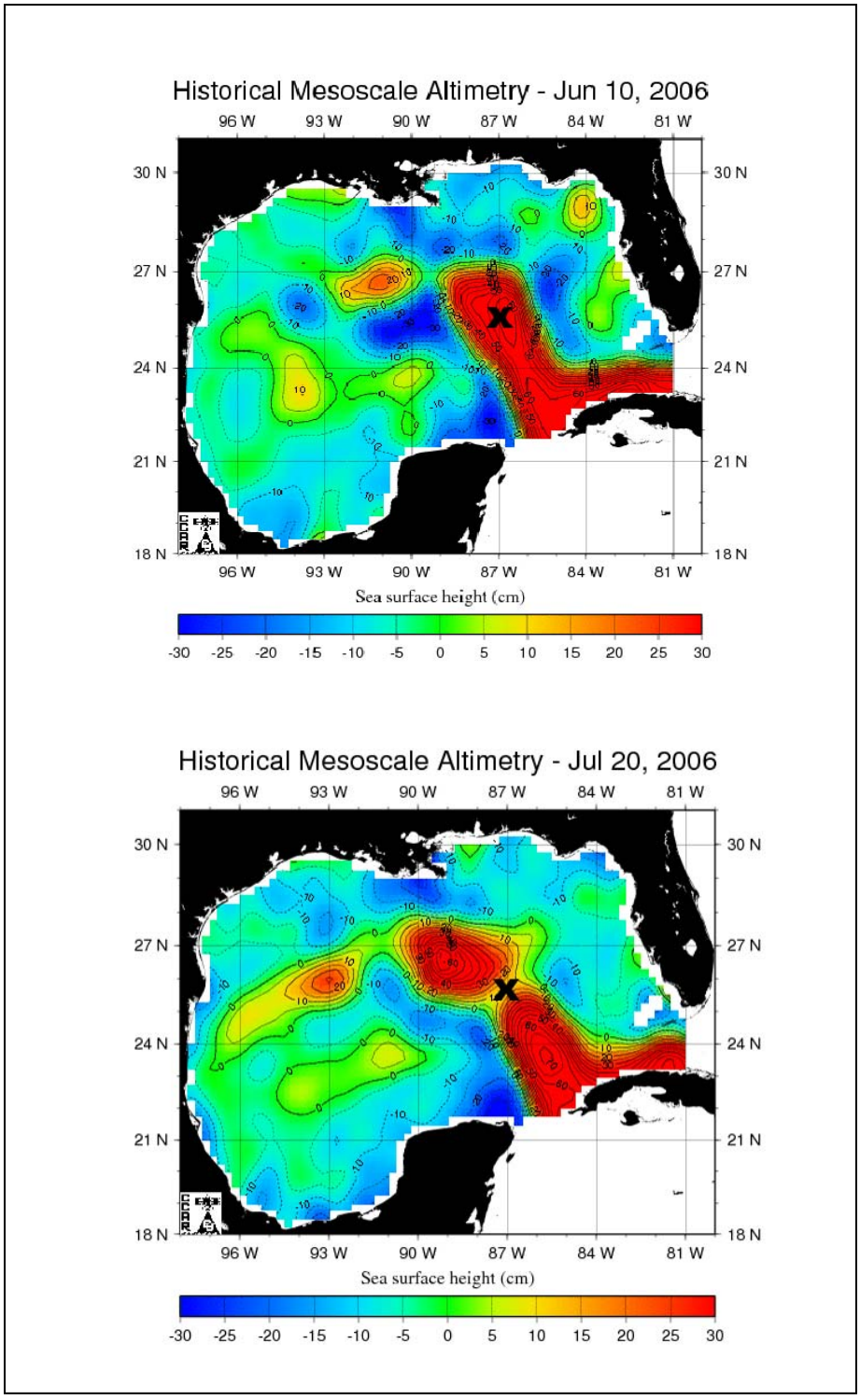

Figure 3-10. Sea surface height maps plotted from historical mesoscale altimetry data archived by Dr. Robert Leben, University of Colorado. The mooring location is indicated by an **X**.

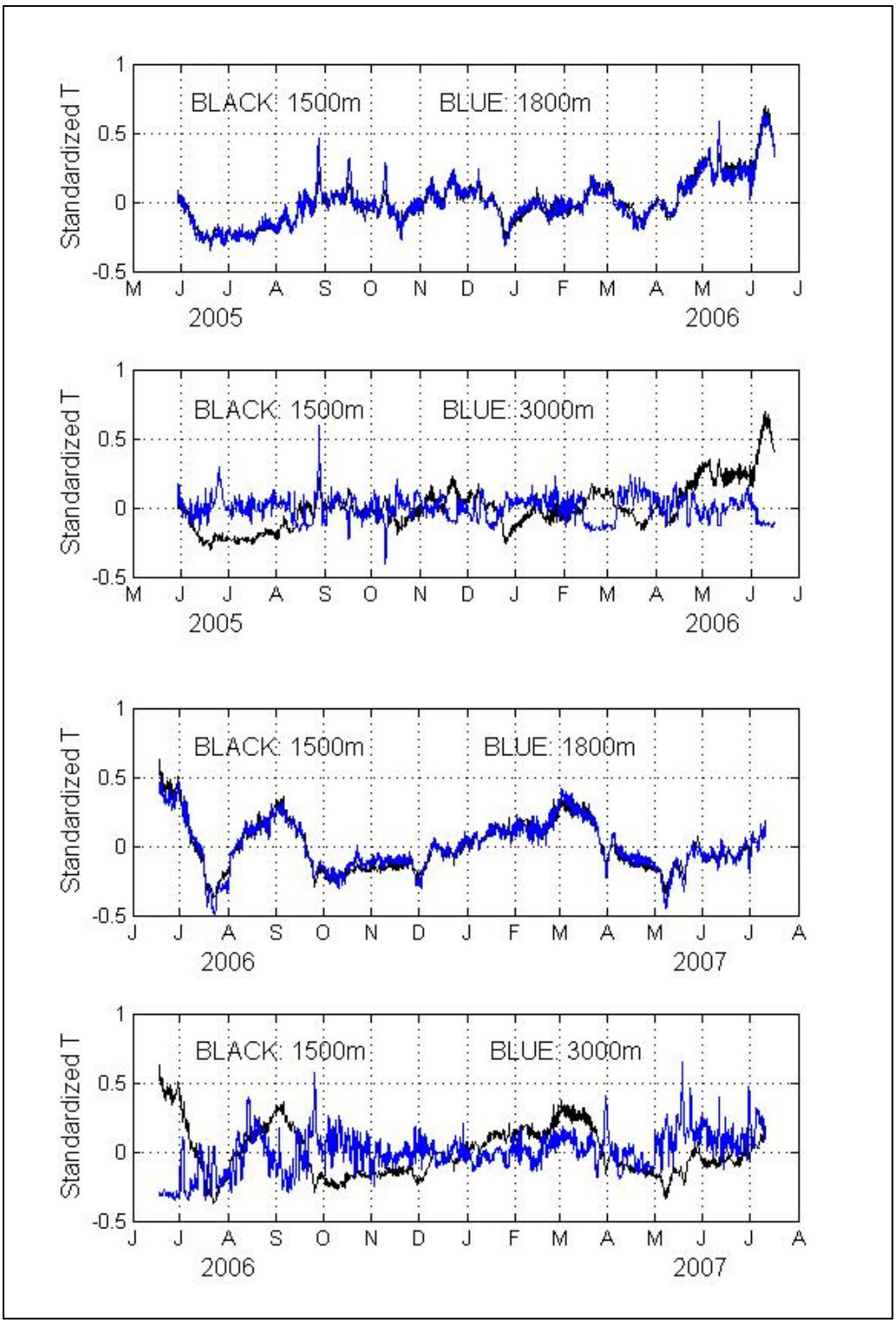

Figure 3-11. Standardized temperature at various depths for Deployment 4 (top) and Deployment 5 (bottom). Temperatures are standardized by dividing by the difference between the maximum and minimum for each time series.

3.5 The Fate of Cold Deep Caribbean Water

The temperature and salinity records exhibit several brief pulses of anomalous water from 1500 m to the bottom. These pulses are characterized by intrusions of relatively cold, salty water at 3000 m and 3200 m and intrusions of relatively warm fresh water from 1500 m to 2500 m. The pulses are not seen at 750 m or 1000 m. Three such pulses are visible in Figure 3-12 on 9/1/05, 9/16/05, and 10/09/05. They last from .5 days to 2.5 days. Similar pulses were observed during Deployment 4 on 12/10/05, 5/5/06, 5/11/06, which last from .5 days to 2 days. The duration and magnitude of the pulses in temperature or salinity at 3000 m is proportional to that of the pulses in temperature or salinity above, just in the opposite direction. The deep response associated with Hurricane Katrina is explained in Chapter 4. The pulses of cold, salty water are likely remnants of dense Caribbean water that enters the GOM at sill depth in the Yucatan Channel. The relatively dense Caribbean water enters the GOM sporadically, descends over the slope, and flows counter-clockwise along the slope (DeHaan and Sturges 2004). This deep inflow originates from below 2000 m in the Caribbean and enters the GOM in a boundary layer up to 200 m thick (Rivas et al. 2005). This deep inflow is oxygen rich, which contributes to the oxygen maximum in the bottom waters of the GOM. Rivas et al. (2005) emphasize that the cold, salty Caribbean water must reach the bottom in order to maintain the bottom oxygen maximum. Rivas et al. (2005) suggest that Topographic Rossby waves are responsible for these deep inflow events and that they are triggered by meanders in the mean flow or eddies. Observations of the cold, salty tongue in deep water not only indicate presence of a deep cyclonic gyre, but the cold tongue may be a factor in driving the deep cyclonic gyre (Sturges, 2005).

The observation of relatively warm, fresh water above the pulses of cold, salty water is reasonable. If a lens of relatively dense water flows along the bottom, then it would under cut the lighter water above it, which would become displaced upward. The stratification that we see at the mooring was likely formed some distance from the mooring and advected to the mooring site by the deep circulation, i.e. the deep eddies. The three pulses of dense water that we see in Figure 3-12 coincide with rotary currents that are indicative of the passage of deep eddy-like features (Figure 3-13). The small pulse just before 9/1/05 may be related to the large inertial response of the deep water to Hurricane Katrina. The larger pulses on 9/16/05 and 10/9/05 appear to be associated with the passage of deep cyclonic features.

Within the high resolution model, the cold salty water does not mix readily with the ambient water, and it reaches the bottom as an identifiable coherent plume. The inflow and outflow at the Yucatan sill is observed prior to and after each ring separation. The inflow averaged over 3 weeks prior to a typical ring separation and after a ring separation are illustrated in Figure 3-14. The cold tongue hugs the eastern slope during the formation of a LC ring as indicated by the temperature contours. After a ring has separated the outflow into the Caribbean is warmer and more uniform across the deep channel. The net flow into the GOM as a ring is forming and the backflow into the Caribbean after a ring has separated are explained using a simple conceptual model by Bunge et al. (2002) based on the hypothesis of Maul et al. (1985). The conceptual model compares the areal extension of the LC from satellite altimetry to the cumulative deep transport in the Yucatan Channel and results in a greater than .9 correlation with a ~1 week lag. The basic premise of the simple box model is that the total volume of water in the

LC should correlate with the deep transports in the Yucatan Channel and that the total volume of water in the GOM should remain constant.

Further mixing of the cold and salty tongue of the inflowing Caribbean water with the ambient water in the eastern GOM takes place as the cold and salty tongue rotates counterclockwise along the periphery of the eastern basin. Additional mixing of this cold and salty water takes place as deep water eddies shear off portion of the cold and salty water and advect it toward the interior region of the eastern basin. This advection by deep water eddies is clearly identifiable in the model output. Consequently, advection of cold and salty water passing by the mooring site gives rise to the observed energetic events in water mass characteristics in deep water at the mooring site.

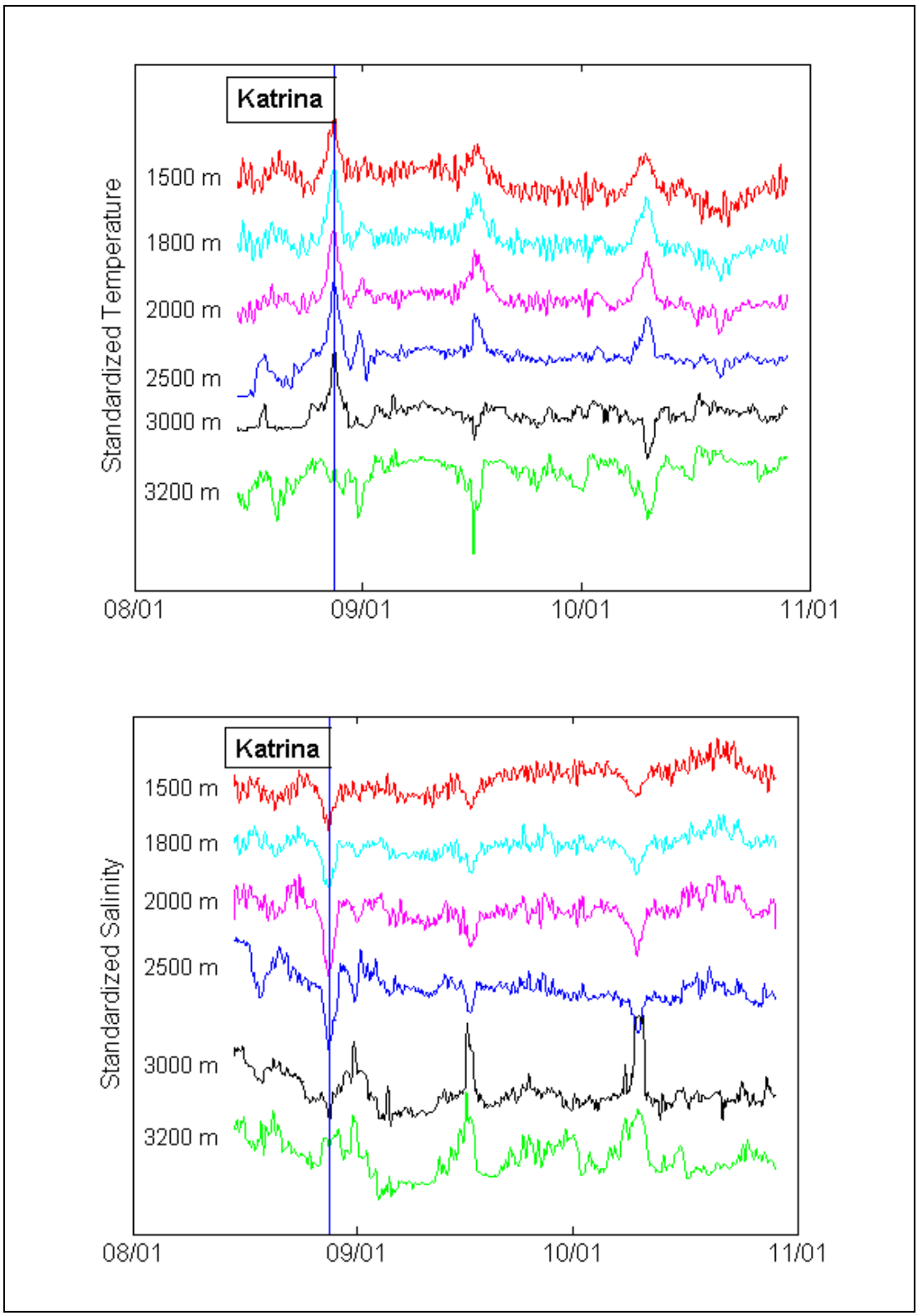

Figure 3-12. Standardized temperature (top) and salinity (bottom) from Microcats during Deployment 4. The times series are standardized by subtracting the mean and dividing by the range of the selected time period.

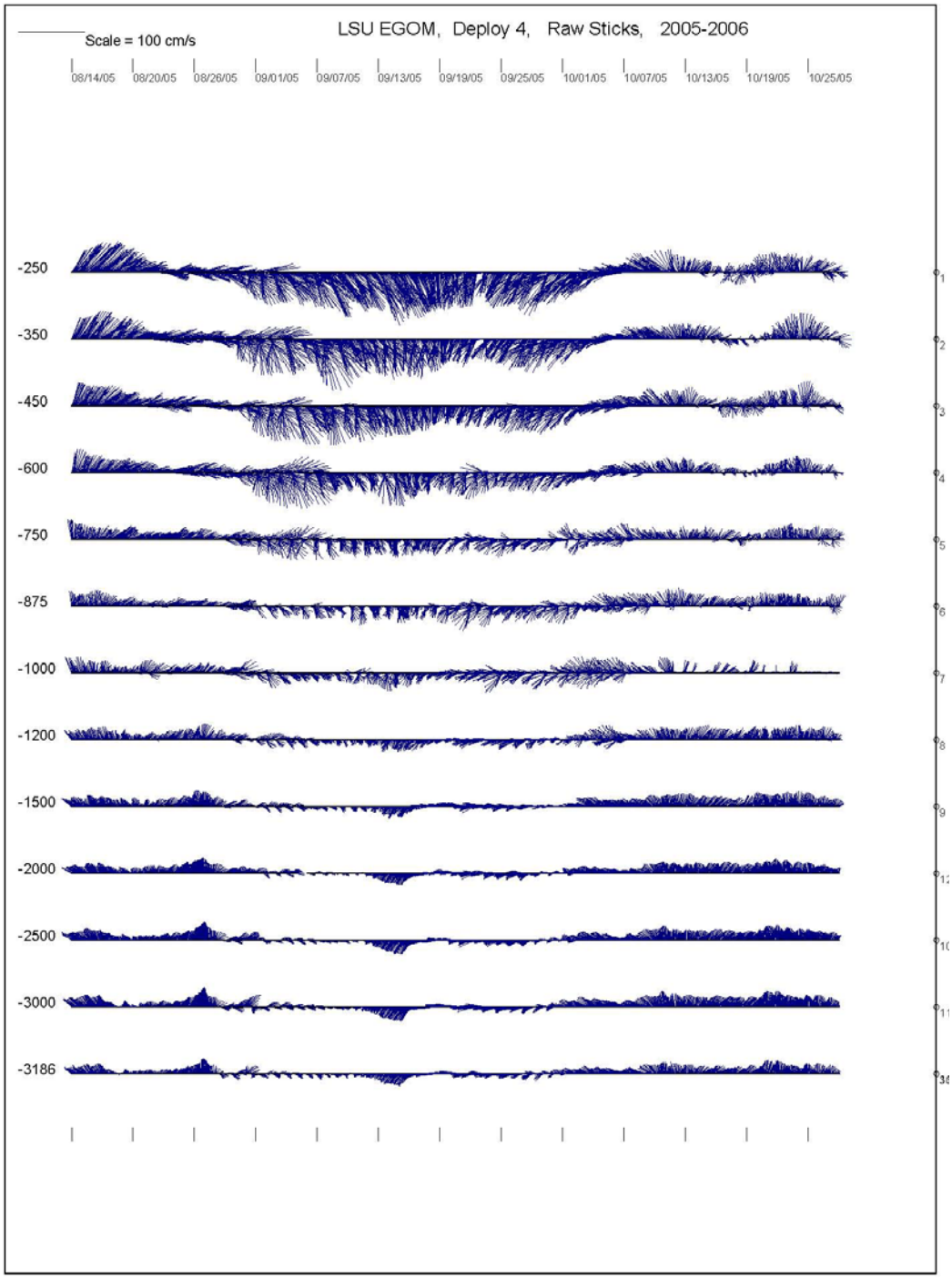

Figure 3-13. Stick plots from Aanderaa current meters during Deployment 4 for approximately the same time period shown in Figure 3-12.

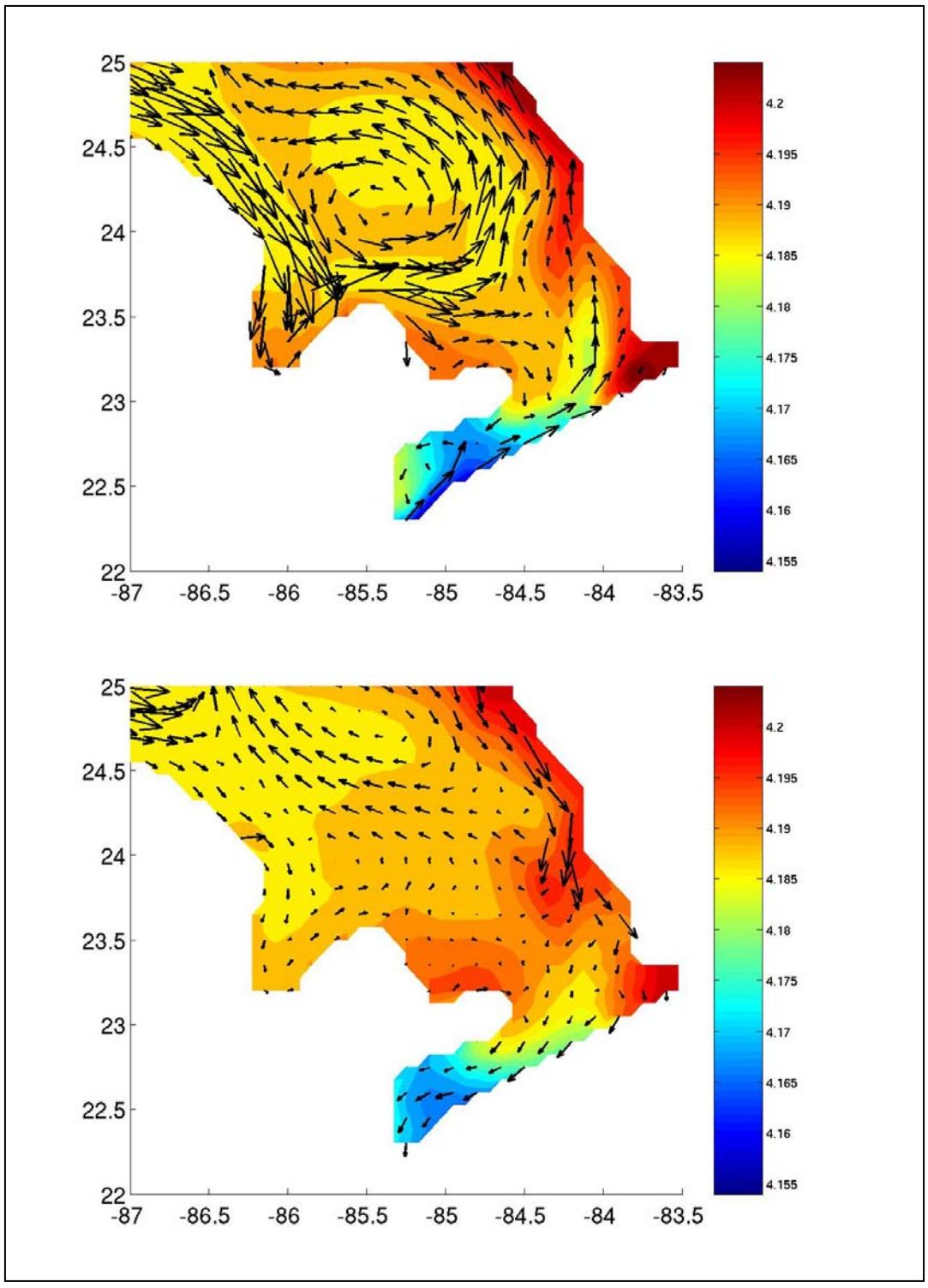

Figure 3-14. Model temperature (color bar units in ^{o}C) and velocity vectors at 2200 m averaged over the 3 weeks prior to a ring separation (top) and the 3 weeks following a ring separation (bottom).

CHAPTER 4

IMPACTS OF 2005 HURRICANES

During Deployment 4 a record number of tropical storms and hurricanes formed over the Atlantic, Caribbean, and GOM. Six storms passed through the GOM within 322.5 km of the mooring (Figure 4-1). Hurricane Cindy (path #2) was a tropical storm until right before landfall and remained the farthest from the mooring location. The second farthest was Hurricane Wilma (path #4), which passed within 307.9 km. Although Wilma had been a Category 5 before it entered the GOM, it was down graded to a Category 2 by the time of nearest approach to the mooring. Tropical Storm Arlene (path #5) and Hurricane Dennis (path #6) passed within 172.3 and 208.5 km to the east of the mooring, respectively. Dennis became a Category 3 approximately 4 hours before closest approach to the mooring and strengthened to a Category 4 only 2 hours after passing the mooring. These 4 tropical cyclones were not close enough to the mooring to have a discernible impact on the currents at the mooring location.

The two most intense hurricanes to make landfall on the US coast during 2005 were Katrina (path #3) and Rita (path #1). They not only passed relatively close to the mooring location, but they were at or near peak intensity as they approached the mooring. Rita was more intense than Katrina at the time of nearest approach, but the eye was smaller and farther from the mooring. Hurricane Katrina clearly had the greatest impact on the currents at the mooring site, which can be attributed to the large size of Katrina and the close proximity of the mooring to the path of Katrina. The u- and v-components of velocity as measured by 7 current meters during the passages of Katrina and Rita are presented in Figure 4-2. The impact of Katrina is indicated by the large amplitude fluctuations in the upper 600 m, but the impact of Rita is hard to distinguish from the background state. More details about the passage of these storms on the currents at the mooring are presented below.

4.1 Hurricane Katrina

Hurricane Katrina has earned the rank of costliest hurricane to ever make landfall in the United States, as well as third most deadly and third most intense hurricane to make landfall in the United States (Blake et al., 2007). The intensification of Hurricane Katrina as it neared the mooring location is shown in Figure 4-3. At 22:45 CDT on August 27, the wind speed at the mooring location (25.5 º N, 87 º W) was estimated to be at least 30 m s^{-1} (67 mi hr^{-1}) and the wave height was 15 m or greater (Figure 4-4). On August 28 at 05:11 UTC the diameter of the eye of Katrina was approximately 38 nm (70 km) along the major axis oriented WNW (120º-300º), and 32 nm (59.3 km) along the minor axis as measured by aircraft reconnaissance. At 09:21 UTC, the eye had a diameter of 30 nm (55.6 km) on the major axis oriented E-W (90º-270º) and 25 nm (46.3 nm) along the minor axis. During the interval from 06:00 and 09:00 UTC (01:00 and 04:00 CST), the center of circulation of Katrina came within 30 km of the mooring (Figure 4-5), the maximum wind speed was 145 mph, and the central pressure was 935 mb. During this same interval, the diameter of the eye ranged from 46 km to 70 km based on the measurements taken at 05:11 UTC and 09:12 UTC by aircraft reconnaissance. Consequently the

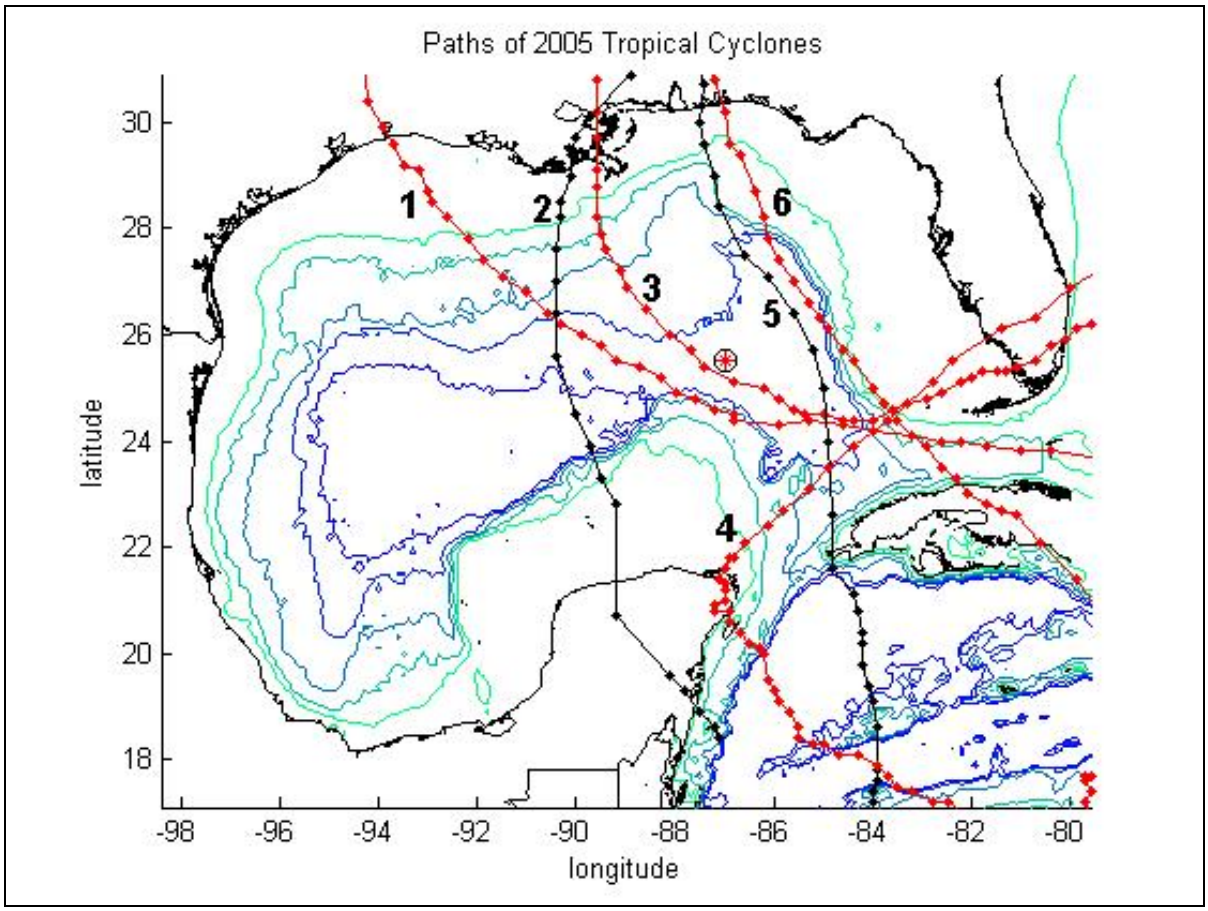

Figure 4-1. Paths of 6 tropical cyclones to pass through the GOM during 2005: (1) Hurricane Rita, (2) Hurricane Cindy, (3) Hurricane Katrina, (4) Hurricane Wilma, (5) Tropical Storm Arlene, and (6) Hurricane Dennis. The red star marks the location of the mooring.

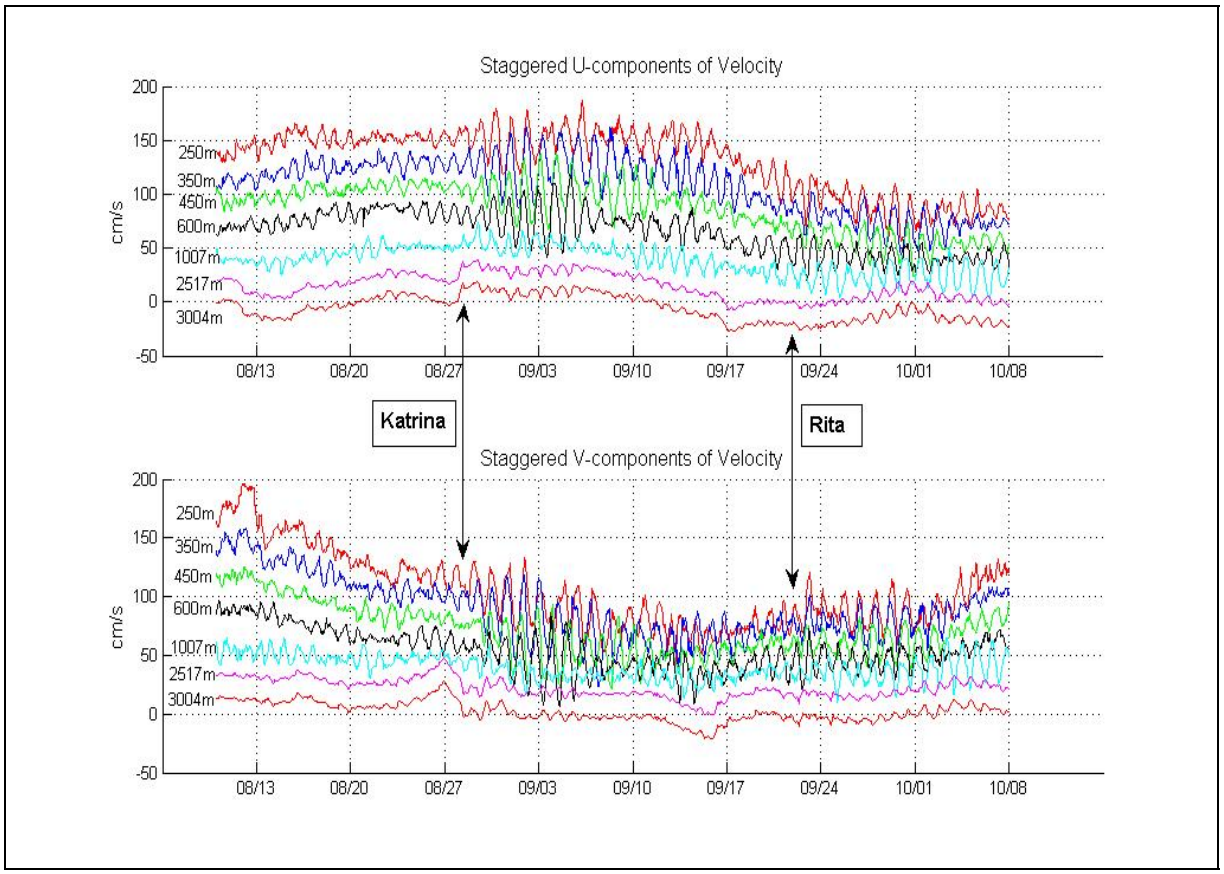

Figure 4-2. Staggered time series of the U-component of velocity (top) and the V-component of velocity (bottom) recorded by the current meters at 250 m, 350 m, 450 m, 600 m, 1007 m, 2517 m, and 3005 m. Multiples of 20 cm s^{-1} are added to each time series above the 3004 m record.

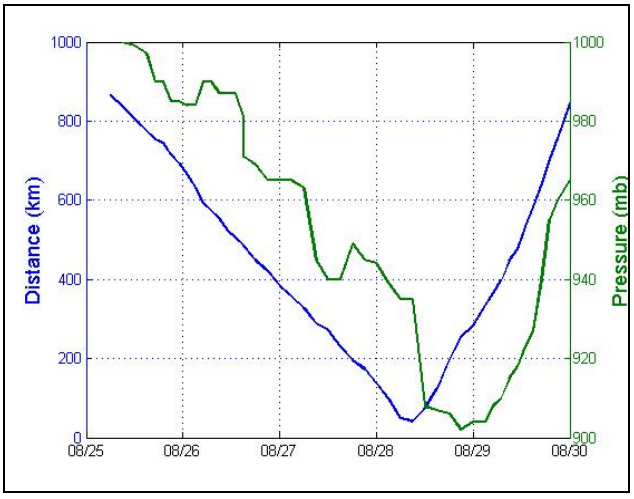

Figure 4-3. Minimum central pressure of Hurricane Katrina (mb) and its distance from the mooring (km). All data from the Johns Hopkins Applied Physics Lab Ocean Remote Sensing website: http://fermi.jhuapl.edu/hurr/05/katrina/index.html.

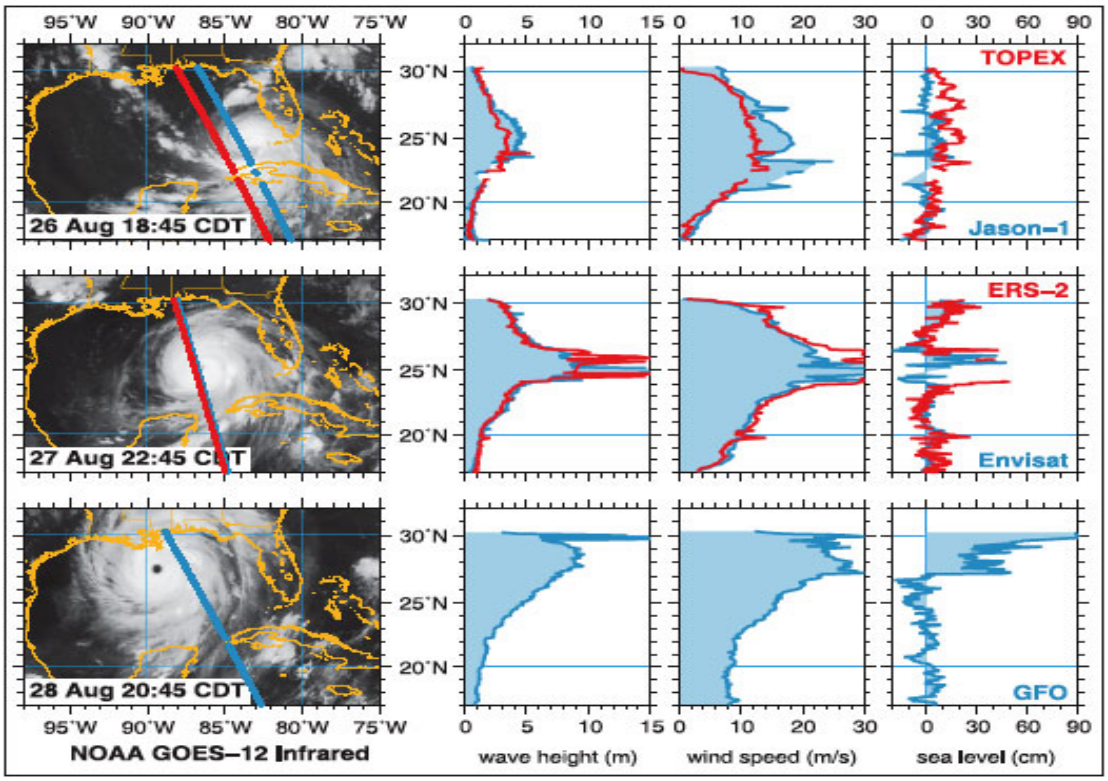

Figure 4-4. Tracks of TOPEX, Jason-1, ERS-2, Envisat, and GFO satellites superimposed over the NOAA Goes-12 Infrared images of Hurricane Katrina (first column). Plots of wave height (second column), wind speed (third column) and sea level (fourth column) as a function of latitude along the satellite tracks at the times given in the first column. (Reproduced from Bettway 2006).

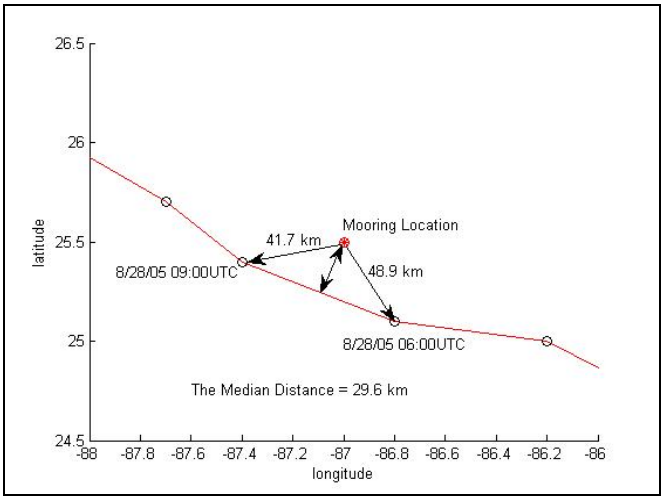

Figure 4-5. Location of the mooring relative to the track of Hurricane Katrina. The double arrow represents the median distance of ~29.6 km.

mooring experienced the strongest winds of the eye wall for several hours as Katrina moved over the mooring location. At 12:00 UTC on 8/28/05 when Katrina was only 73.7 km from the mooring, it reached Category 5 status with maximum wind speeds of 160 mph and a central pressure of 908 mb. As Katrina approached the mooring it moved over the warm water of the LC (Figure 4-6), which is a critical factor in the strengthening of hurricanes in the GOM.

4.1.1 Currents Observed at the Mooring

The impact of Katrina can be seen in the velocity field from the near surface all the way to the bottom. The response of the upper 140 m was recorded by the upward looking ADCP at 140 m. The sampling interval for the uppermost ADCP was erroneously set to 4.5 hours. Also the velocity time series in the top 3 bins, which were at depths of 49 m, 57 m, and 63 m, contained too much noise to be included in the analysis. Between 73 m and 100 m, the current surge exceeded 100 cm s^{-1} (Figure 4-7). The large amplitude response in the upper 100 m can be attributed to the combined effects of wind stress, storm surge, and drop in atmospheric pressure as the eye went over. The rotary nature of the currents immediately after Katrina can be inferred from the stick plots in Figure 4-8, although the 4.5 hour sampling reduces the number of observations to fewer than 6 per day. Fortunately there were 13 Aanderaa current meters ranging from 250 m to 3187 m that were working properly during the passage of Katrina.

The NIO (Near-Inertial Oscillation) is apparent in the velocity field through the entire water column before Katrina (Figures 4-2, 4-7 and 4-9), although the amplitude of the NIO is much smaller below 1000 m. Large amplification of the NIO is observed at all depths after the passage of both Katrina and Rita (Figure 4-2). The large amplitude response lasted until September 28 in the upper 1000 m (Figure 4-9). A repeating downward propagation of the velocity maxima that begins at nearly 7 days intervals and lasts for 10 days can be seen in contour plots of velocity magnitude (Figure 4-9). Oey et al. (2008) computed the energy from NIO in the mooring data for the 2005 hurricane season and found that the NIO response was much greater for Hurricanes Katrina and Rita than for Wilma or Dennis. Oey et al. (2008) reported that the downward propagation of energy in the upper ~600 m during the 10 days following Katrina at the mooring site had a group speed of 30~50 m day^{-1}. Morozov and Velarde (2008) observed the downward propagation of inertial oscillations in response to hurricanes at moorings in the northwestern Pacific and Atlantic Oceans. They observed that the NIO response lasts for 10-12 days and the downward propagation in the upper ocean varies from 1-10 m hr^{-1}. The velocity of the downward propagation of inertial oscillations was influenced by the stratification and vorticity (Morozov and Velarde 2008).

The downward propagation of inertial oscillations has been simulated by Kundu (1986) in a linear, two-dimensional, continuously stratified model with a maximum depth of 2500 m. The open ocean model is forced with a propagating wind field that has a translation speed equal to the motion of a hurricane. Kundu (1986) observed a downward propagation of energy with a speed of .2 cm s^{-1} in the upper thermocline, a decrease in the amplitude of the inertial oscillation with depth, and an upward propagation of phase with a speed of ~2 cm s^{-1} in the model output. There is a blue-shift of the inertial frequency toward a higher frequency than the local inertial

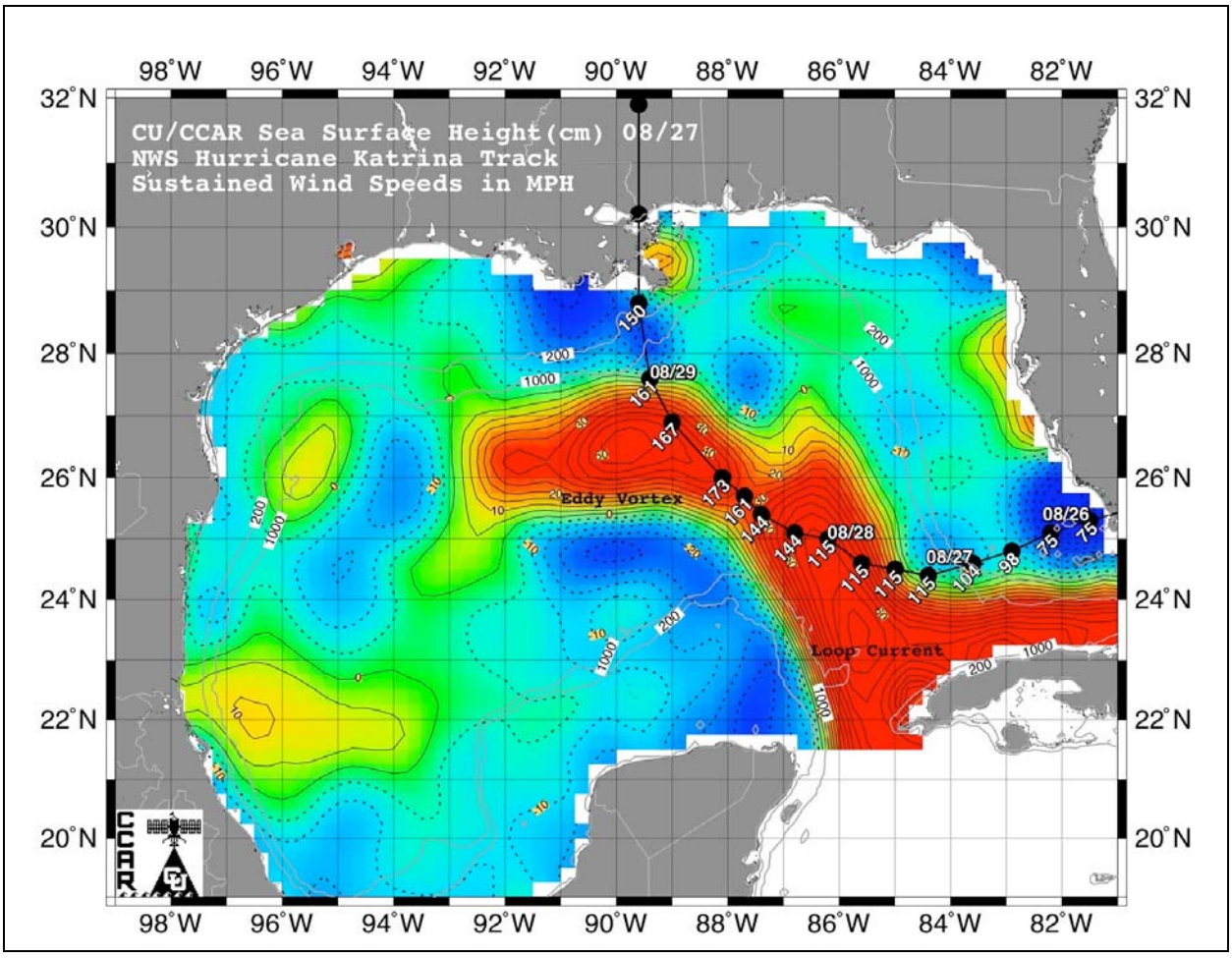

Figure 4-6. Sea surface height map from August 27, 2005, is shown overlaid with the path and maximum sustained winds reported for Hurricane Katrina by the NOAA's National Weather Service (NWS). Reproduced from Leben et al. (2006).

frequency and the blue-shift of frequencies increases with depth (Kundu 1986). A blue shift of the inertial frequency was also observed at the deep water mooring and is discussed in more detail below. Kundu (1986) attributes larger blue shifts in the deep ocean to larger values of the internal wave speeds.

The rotary nature of the currents is apparent in the stick plots of velocity and is accentuated at 600 m (Figure 4-10), which is near the base of the thermocline. The trapping of the NIO during Katrina is discussed by Oey et al. (2008). This depth is below the strong surface flow associated with the LC and above the weak currents associated with the interface near 1000 m. In the deep layer, the NIO are markedly visible following a northward surge which preceded the passage of Hurricane Katrina (Figure 4-10, bottom). The NIO persist for ~7 days after Katrina at 1500 m and can be observed for a longer time with increasing depth down to 3200 m.

Another way to view the rotary nature of the currents is with progressive vector diagrams (PVD) for each depth, which provide Lagrangian particle displacements based on the Eulerian measurements (Figure 4-11). The PVD are plotted separately for the upper (250 m – 600 m) lower (750 m – 3000 m) depth ranges. The large displacements in the PVD of the upper 600 m demonstrate are due to the higher velocities associated with the LC. The general current direction is southeasterly in the upper 600 m and easterly below this depth. The circular motion at 600 m is also accentuated in the PVD of the demeaned currents (Figure 4-12). The PVD of the demeaned currents demonstrate that the onset of the near-inertial oscillations is progressively delayed with depth.

Rotary spectra of the depth averaged currents from the upward-looking ADCP at 140 m for the 4 weeks prior to Katrina are compared to the rotary spectra for the 10 days following the passage of Katrina (Figure 4-13). As Katrina approached the mooring the winds opposed the direction of flow of the LC and after the eye moved north of the mooring the winds were in the general direction of the LC (Figure 4-6). The wind strength and direction were recorded by the nearby NDBC meteorological Buoy 42003 located at 25.97ºN, 85.59ºW (150 km NE of the mooring) up until 02:00 UTC, after which the buoy went out of commission. The last record of speed and direction were 28.9 knots and 82º (toward the WSW), respectively.

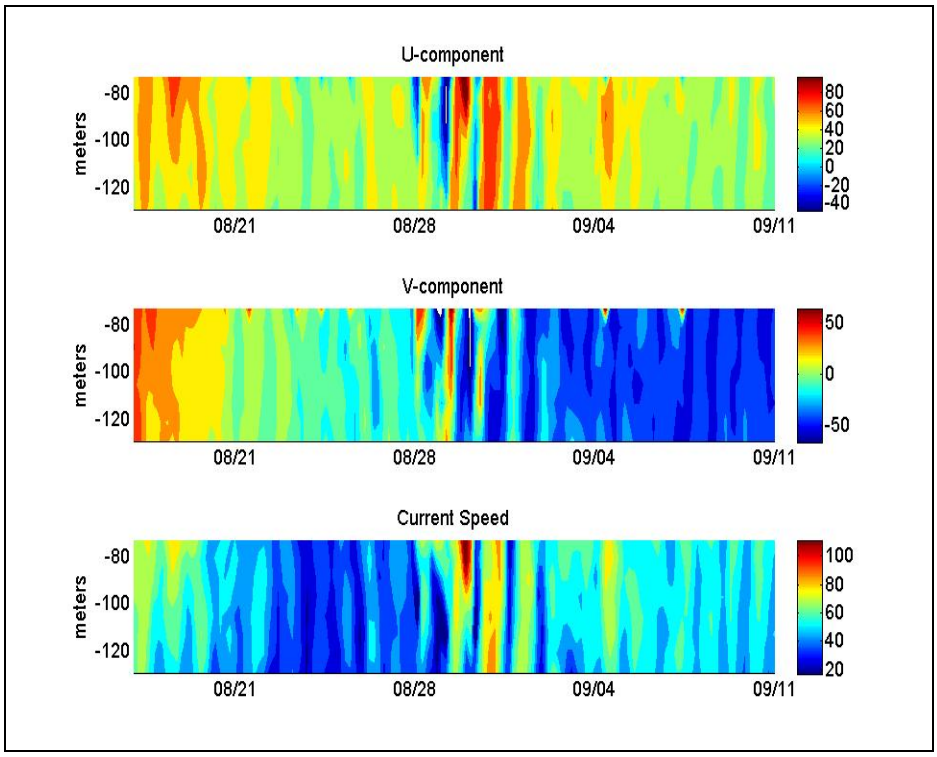

Figure 4-7. Contours of the U-component, V-component, and magnitude of velocity from the ADCP at 140 m.

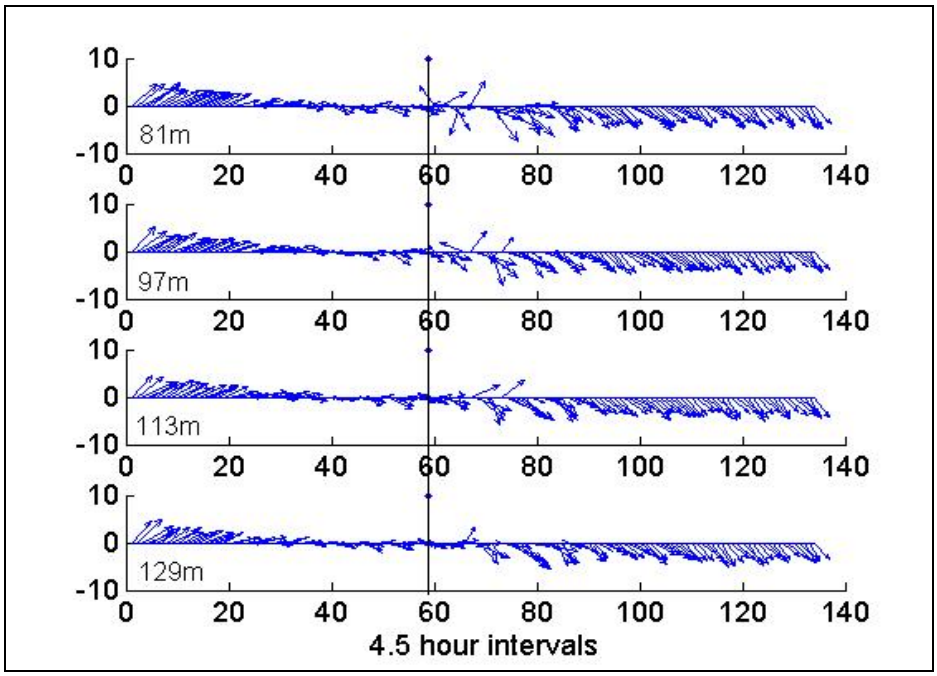

Figure 4-8. Velocity vectors for the same time period as Figure 4-7. The vertical line denotes the passage of Hurricane Katrina.

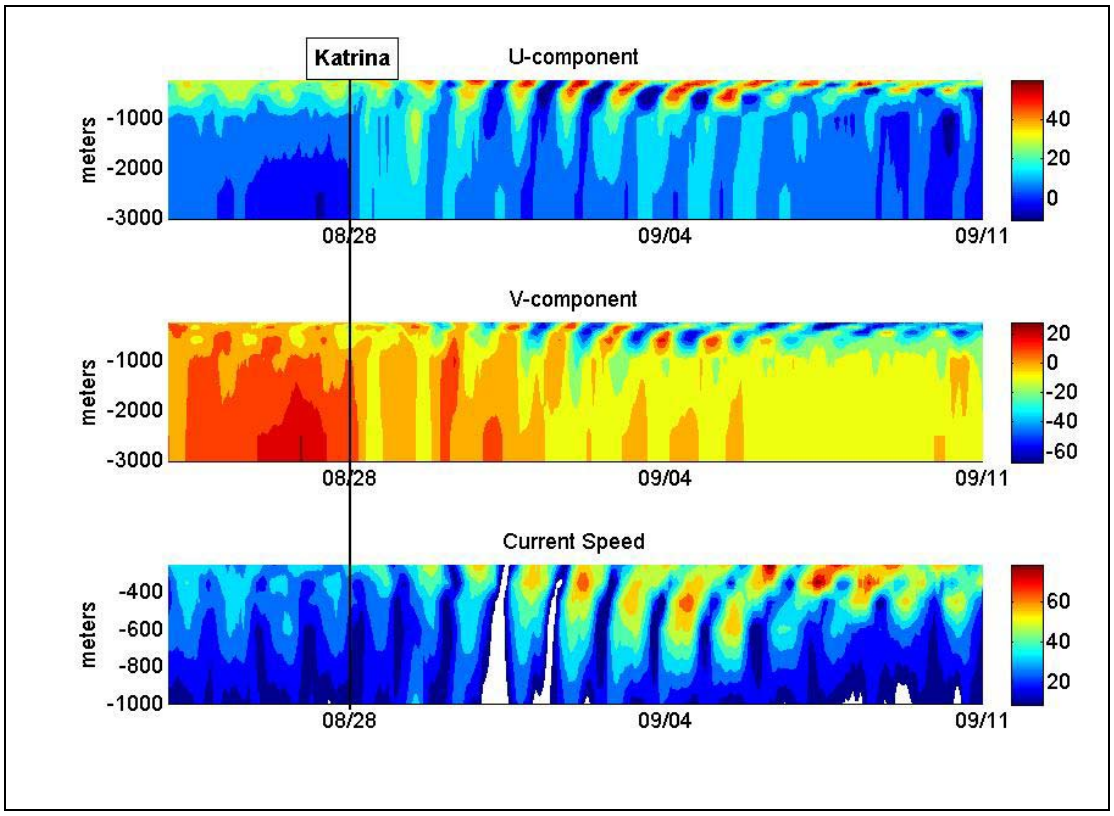

Figure 4-9. Contours of U-component (top) and V-component (middle) of velocity from current meters at 250 m, 350 m, 450 m, 600 m, 750 m, 875 m, 1007 m, 1500 m, 1200 m, 2000 m, 2500 m, 3000 m, and 3200 m. Contours of the magnitude of velocity for the top 5 current meters (bottom). The sampling interval is 60 min.

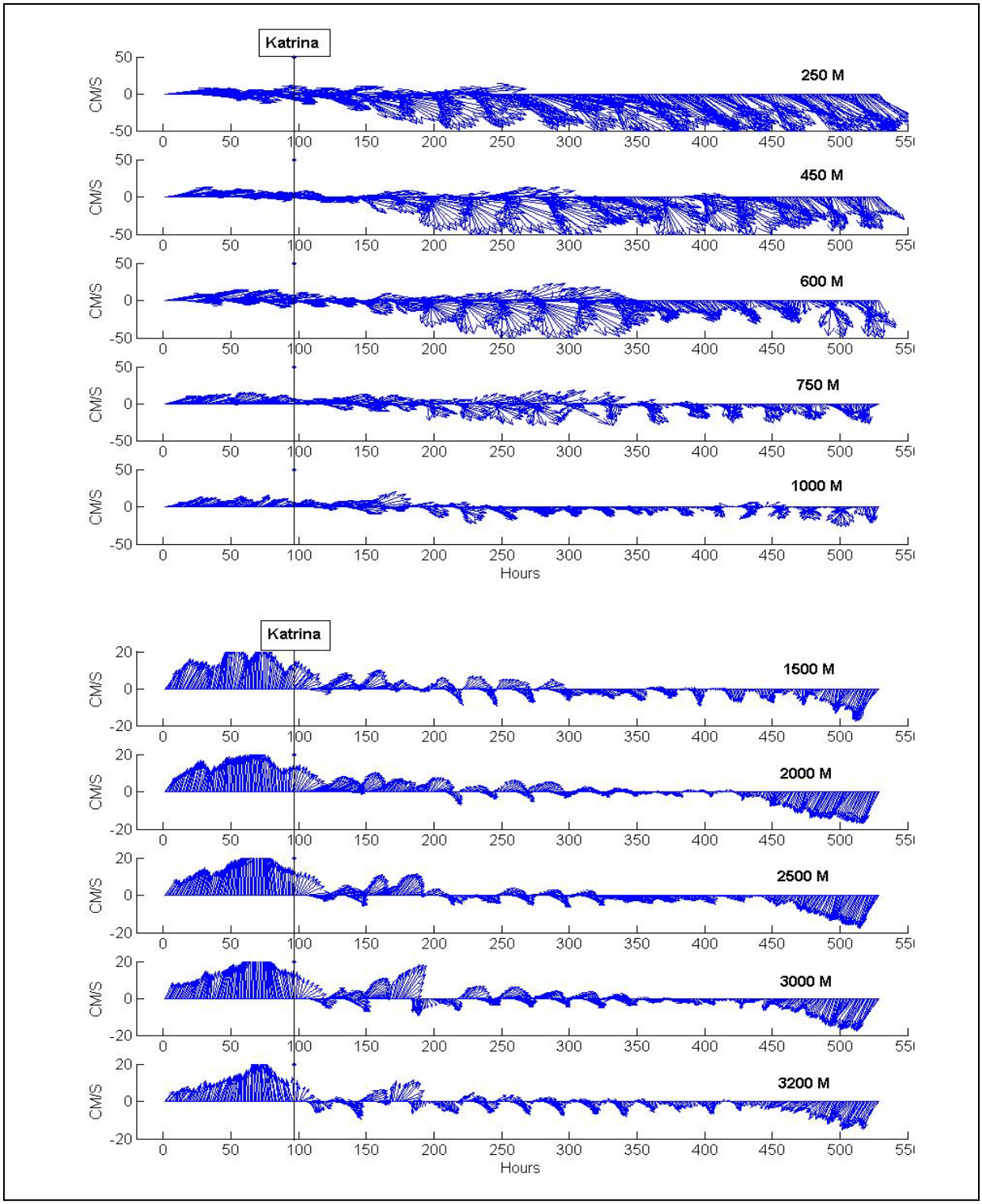

Figure 4-10. Upper layer (top) and lower layer (bottom) velocity vectors from current meters at the depths indicated for the same time period shown in Figure 4-8. Current vectors greater than 50 cm s^{-1} (top) and 20 cm s^{-1} (bottom) are truncated.

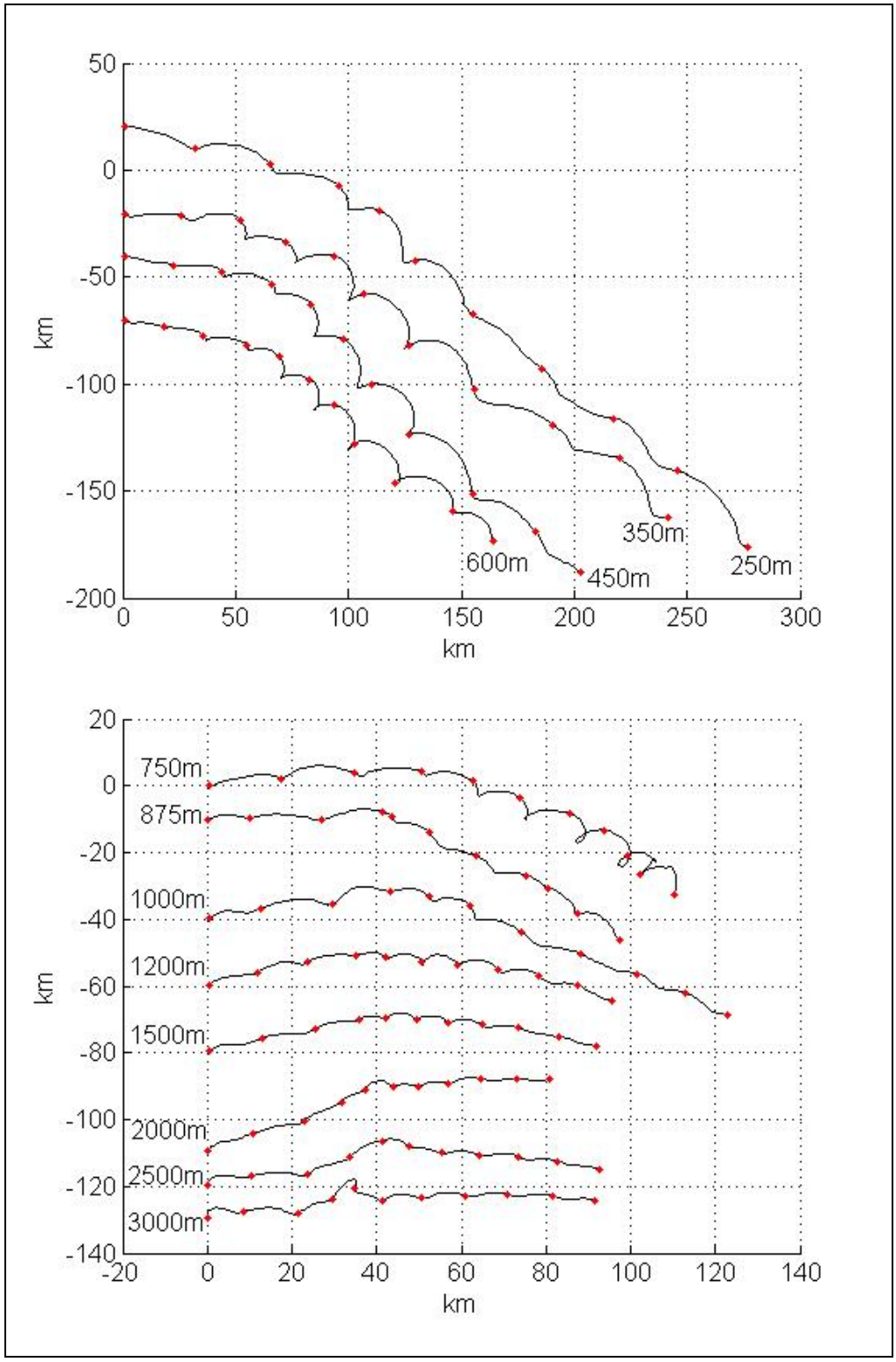

Figure 4-11. Progressive vector diagrams from U- and V-components for 10 days from August 28, 2005 at 00:00 to September 7, 2005 at 00:00. The red '·' marks each 24 hour segment.

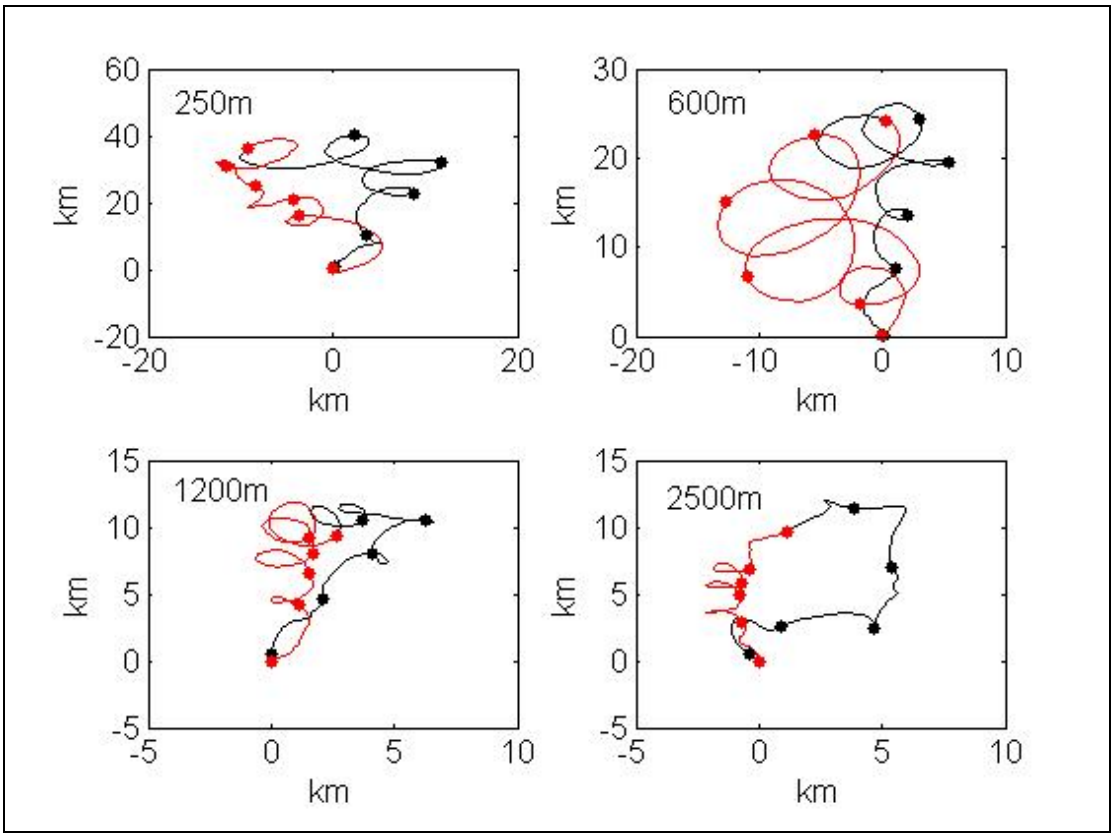

Figure 4-12. Progressive vector diagrams from demeaned time series of the U- and V-components. Each PVD begins and ends at the point (0,0). The dots mark the beginning of each 24hour segment. The first 5 days are denoted by a black line and the last 5 days are shown in red.

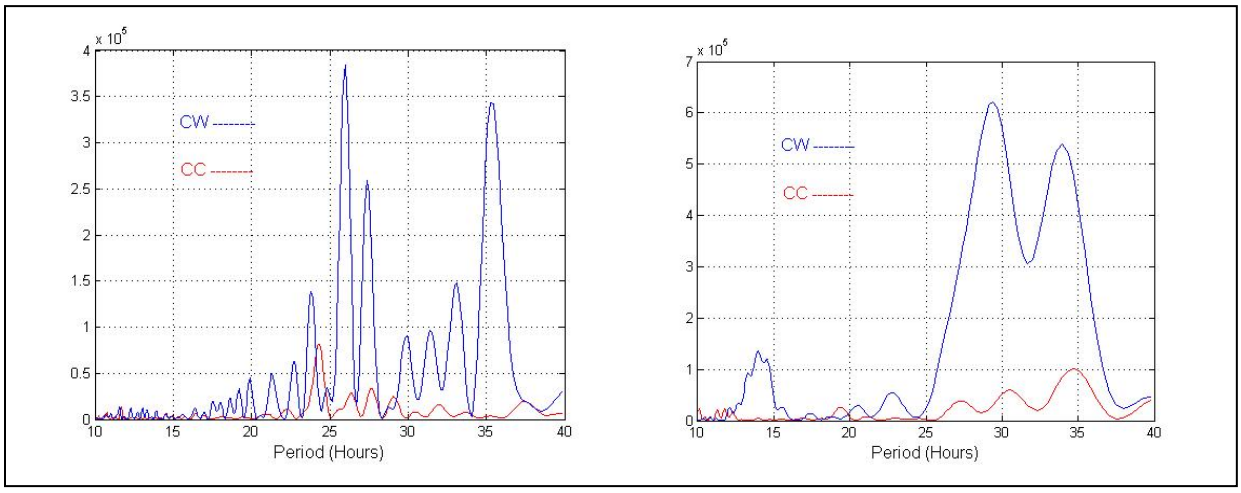

Figure 4-13. Rotary spectra of depth averaged currents (81 m-129 m) from ADCP for 4 weeks prior to Katrina (8/1/05 – 8/28/05) (left) and 10 days following Katrina (8/28/05-9/7/05) (right).

Prior to the storm the rotary spectra exhibits many discrete frequency bands. The clockwise component dominates the spectra, although there is some contribution by the counter clockwise component near 24 hours. The 24- and 26-hours peaks (Figure 4-13) are close to the tidal frequencies observed at the NDBC DART buoy 42408, which was located only 22 km from the deep water mooring, and was coincidentally knocked out of commission during Katrina. The power spectrum of a 6-week record of water column height at buoy 42408 during Deployment 5 is shown in Figure 4-14. The spectrum has distinct peaks at .082 CPD (12.2 hours), .079 CPD (12.4 hours), .041 CPD (24.4 hours), 038 CPD (26.3 hours), and 02835 (35.27 hours). The broader peaks correspond to the semidiurnal tide (12-12.4 hours), the diurnal tide (24-26 hours), and the local inertial period of 27.87 hours.

The peak in the rotary spectra at 27.5 hours is slightly less than the local inertial period (Figure 4-14). After the passage of Katrina, the spectral response is narrower and nearly continuous in the 25 to 37 hour range with only two distinct peaks near 29 and 34 hours. There is a large peak in the pre-Katrina spectrum near 35 hours in the 81 m-129 m depth range, which is slightly longer than the peak at ~33 hours in the pre-Katrina rotary spectrum at 250 m from current meter records (Figure 4-15). Although we have not investigated the source of the peak near 35 hours, it is also present in the spectrum of the SSH from the DART buoy (Figure 4-14).

Rotary Spectra of the currents at 250 m from Aanderaa current meters for the 4 weeks prior to Katrina is dominated by the clockwise component. The largest peak near 28 hours is close to the local inertial period. In the deep water at 2500 m there is more energy in the counterclockwise rotary spectrum and a greater number of individual peaks than at 250 m. The largest peak at 2500 m is near 25 with a secondary peak near 29 hours. The blue shift to a higher frequency (shorter period) with depth is expected (Kundu 1986).

The rotary spectra for the 10 days immediately following the passage of Katrina at 250 m is similar to the rotary spectra in the near surface (Figure 4-16). The spectral response is again narrower with only two dominant peaks at periods slightly greater than 25 and 30 hours. The magnitude of the spectral response is an order of magnitude larger. The post-Katrina rotary spectra exhibit a blue shift toward smaller periods (higher frequencies). The frequency response becomes narrower and the two peaks are shifted toward higher frequencies with depth. The magnitude of the post-Katrina peak at ~25 hours at 2500 m is nearly an order of magnitude higher than the pre-Katrina peak and slightly red-shifted. The rotary spectrum at 2500 m is dominated by the clockwise component in just two very narrow frequency bands around ~22 and ~25 hours. The counter-clockwise component nearly disappears at the base of the thermocline, but increases slightly with depth relative to the counter-clockwise component.

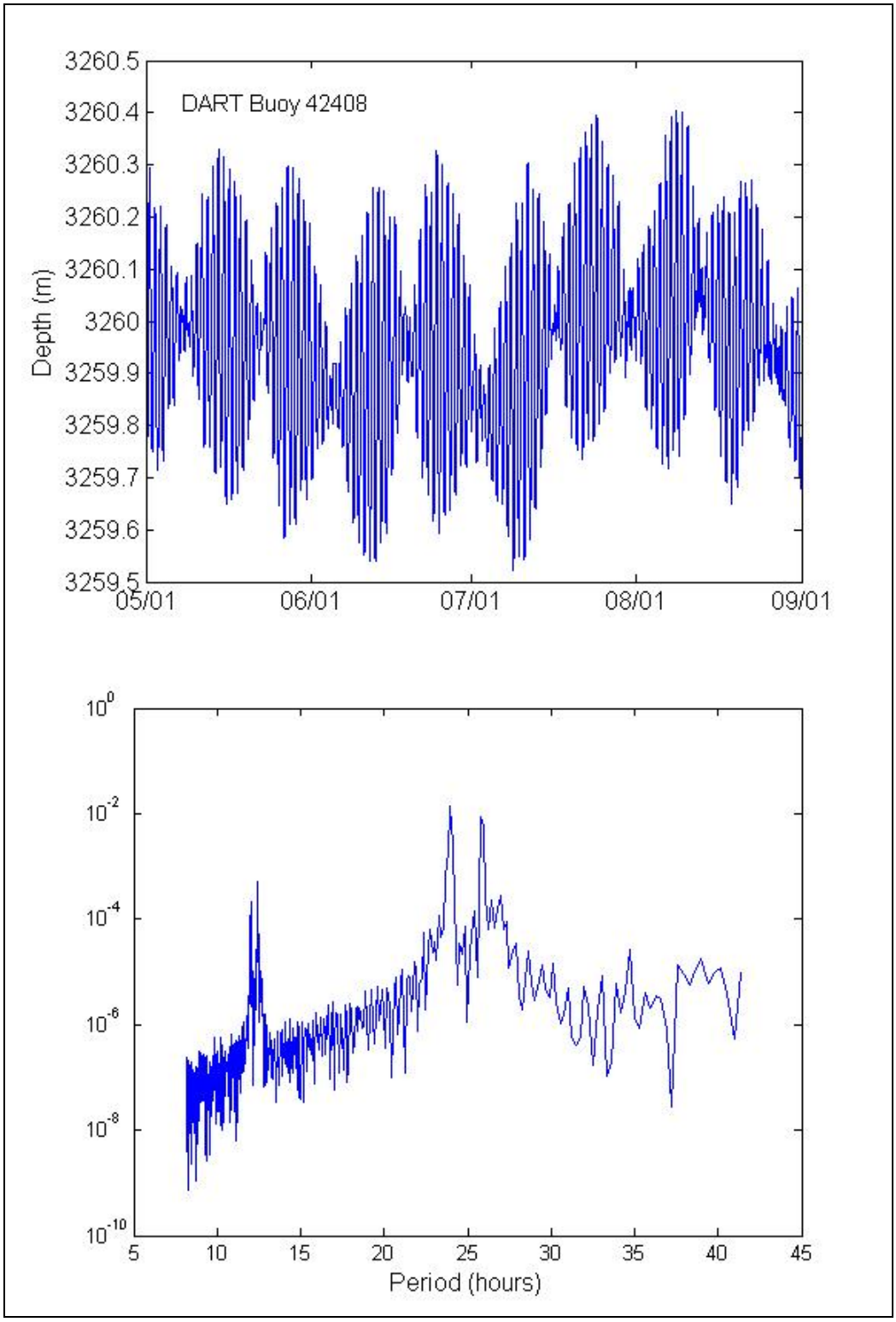

Figure 4-14. Water column height (top) and power spectrum (bottom) from NDBC Dart buoy 42408 during 2006. Buoy 42408 (25.41ºN, 86.8ºW) was approximately 22 km from the Deep Sea Mooring.

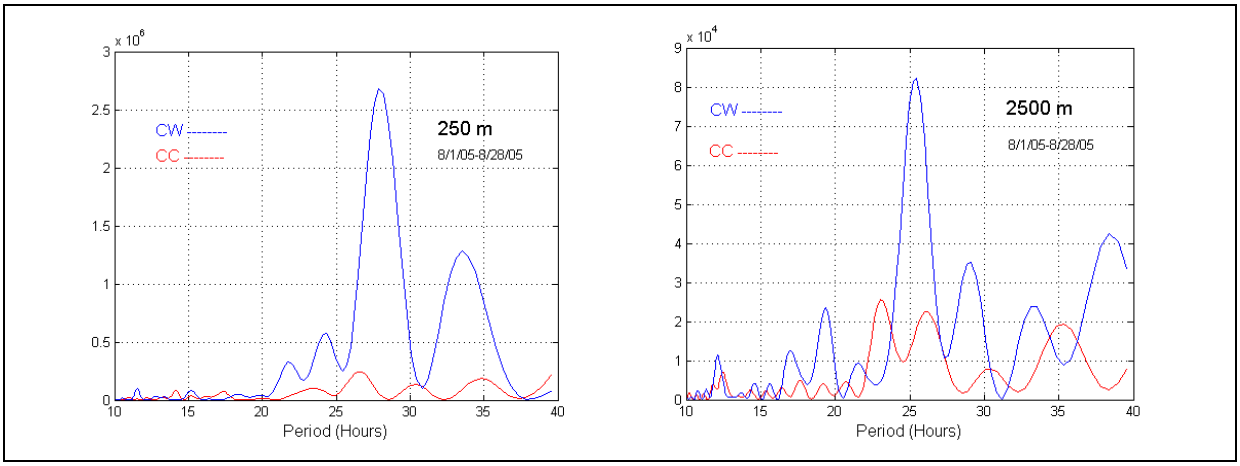

Figure 4-15. Rotary spectra of currents for the 4 weeks prior to the passage of Katrina at 250 m (left) and 2500 m (right).

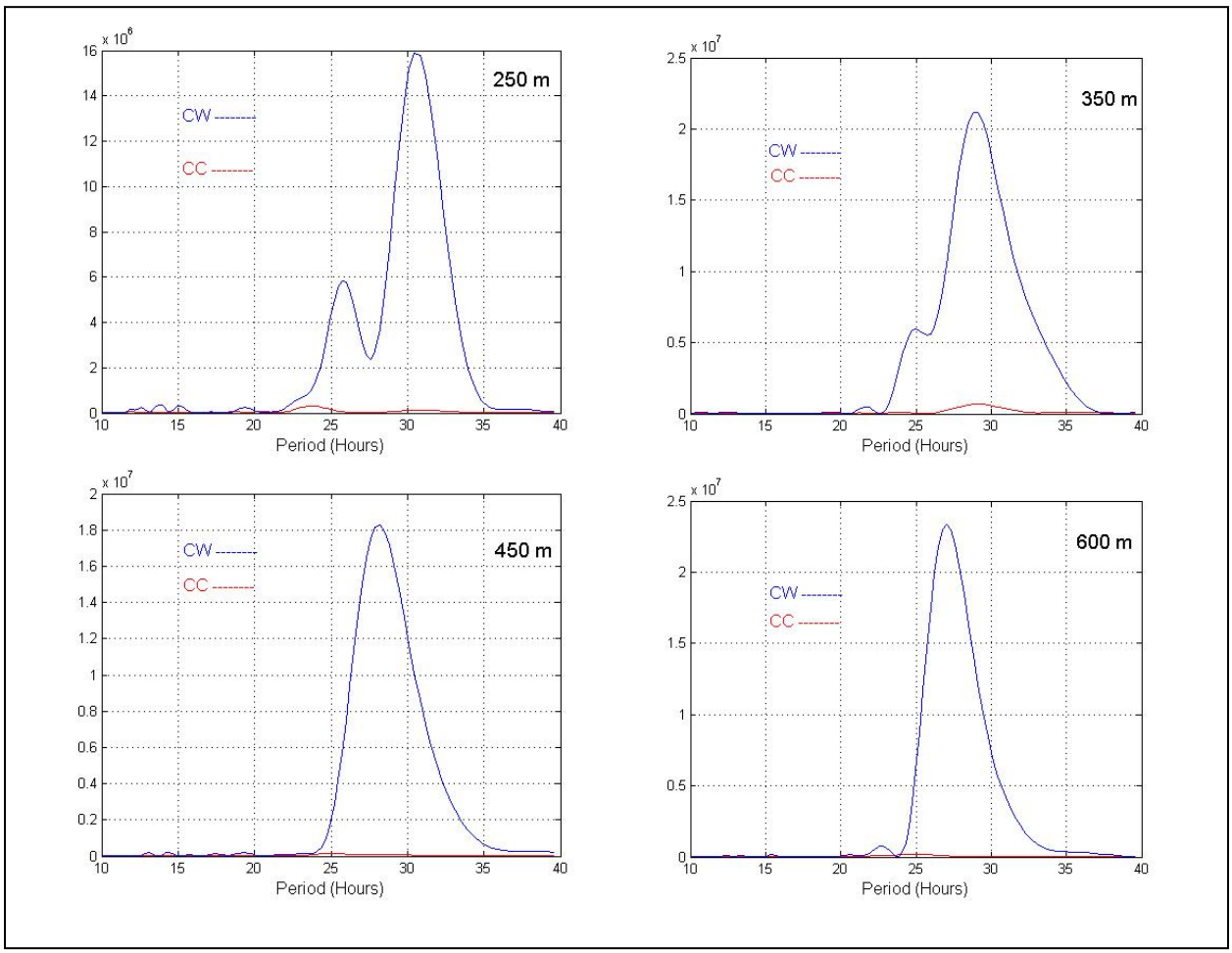

Figure 4-16. Rotary spectra of currents at the indicated depths for 10 days after Katrina passed by the mooring (8/28/05 – 9/7/05).

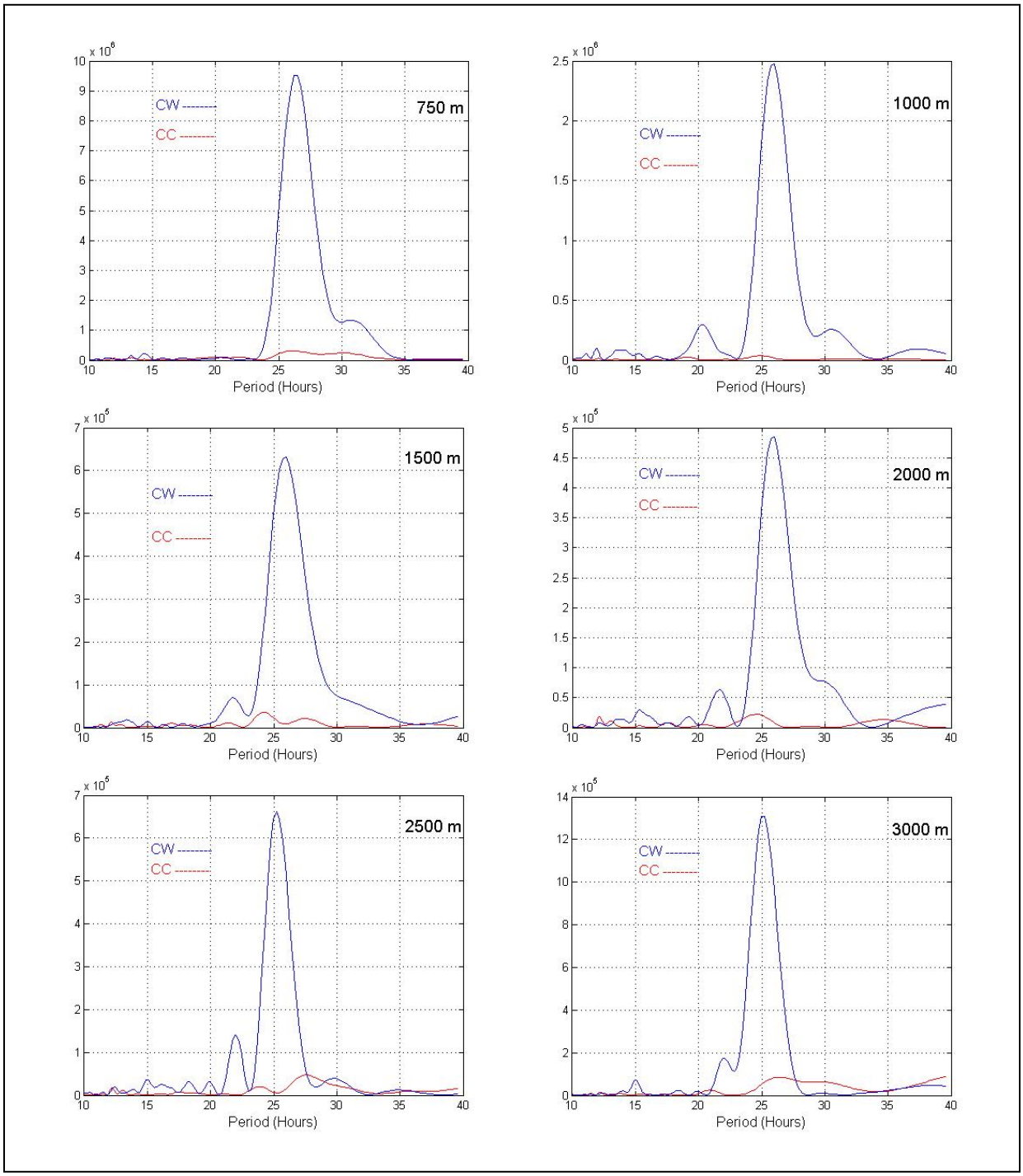

Figure 4-16. Rotary spectra of currents at the indicated depths for 10 days after Katrina passed by the mooring (8/28/05 – 9/7/05) (continued).

4.1.2 Temperature and Salinity Observed at the Mooring

The passage of Hurricane Katrina was reflected in the temperature and salinity fields throughout the entire water column (Figures 4-17 and 4-18). The conductivity sensor at 3200 m failed, so there is no salinity record for this depth. The contour plots in Figure 4-17 and 4-18 are corrected for depth to account for the changes in temperature and salinity that would result simply from depth variations of the Microcats due to blow over of the wire. The demeaned temperature and salinity for the top two Microcats are plotted for the 24-hour period during which Katrina made its closest approach (Figure 4-19). The instrument depth changed by less than 1 m in the first 24 hours (Figure 4-20). In the days following the passage of Katrina, the instrument depths varied greatly in response to the inertial motions of the water column (Figure 4-20).

In the upper 750 m, a decrease in temperature is observed at each Microcat within 2 hours of the nearest approach of Katrina. A corresponding decrease is observed in the salinity at 350 m and 750 m, whereas a slight increase in salinity is observed at 145 m. The upwelling of the isotherms and isohalines during the passage of a cyclone is expected due to Ekman divergence in the upper water column (Morey et al., 2006). There is a relatively large lifting of the isotherms from 700 m to the uppermost instrument at 140 m and a corresponding change in isohalines, although it is less pronounced above 300 m.

At 145 m, the initial drop in temperature of nearly 4ºC is accompanied by an increase in salinity of ~0.275 PSU from 09:00 to 19:00 UTC (Figure 4-19). The cooling of the upper ocean after the passage of a hurricane is expected and has been reported for the following hurricanes in the GOM: Dennis (Morey et al., 2006); Eloise and Belle (Price, 1981); Gilbert (Shay et al. 1992). Changes in SST for 23 tropical cyclones in the GOM, Caribbean, and Atlantic were recorded and discussed by Cione and Ulhorn (2003). According to Shay et al. (1992) the cooling of the ocean surface is due to increased vertical mixing at the base of the mixed layer, thereby entraining cooler water from the thermocline. Price (1981) attributes the mixing to vertical shear of the horizontal currents. Morey et al. (2006) attribute the cooling of the surface waters to the vertical flux of thermal energy from the deep ocean to the surface ocean due to upwelling and horizontal entrainment. Morey et al. (2006) also conclude that the degree of heat loss is a function of the depth of the mixed layer and is greater where the mixed layer is shallow, such as in a cold-core eddy. At the time Katrina passed over the deep sea mooring, it was engulfed in the LC, which acts as a heat reservoir and contributes to the strengthening of hurricanes in the GOM. Katrina strengthened rapidly while it was passing over the mooring and reached peak intensity within 15 hours of closest approach to the mooring. A comparison of the vertical temperature profiles for 6/18/05 and 8/26/95 shows how much deeper the thermocline was during the approach of Katrina due to the presence of the LC (Figure 4-21). The presence of the LC in the southeastern GOM no doubt contributed to the intensification of tropical storms during the 2005 hurricane season.

There were no significant variations in the temperature or salinity observed at 1000 m during the passage of Katrina. Below 1000 m there was an increase in the deep temperature and a decrease in the deep salinity at the same time that Katrina made its closest approach

(Figure 4-18). It appears that warmer and fresher, and consequently lighter water was being advected past the mooring site in deep water all the way to the bottom. The upper layer response to Hurricane Katrina can be explained by upwelling and entrainment of cold subsurface water.

It is interesting to note that the variations in deep temperature and salinity during the passage of Katrina were unique. Other incidences of relatively large increases (decreases) in temperature (salinity) at 1500 m and 2500 m were accompanied by a decreases (increases) in temperature (salinity) at 3000 m and 3200 m, which occurred on 9/16 and 10/11 (Figure 4-15), as well as 12/10/05, 5/5/06 and 5/11/06 (not shown). It was only during Katrina that the increase in temperature and decrease in salinity extended all the way to the bottom (Figures 4-22). The out-of-phase behavior of the temperature and salinity signals above and below 3000 m is discussed in more detail in Chapter 3.3. A similar notable response in the deep water was not observed with the passage of Rita on 9/22/05 (Figure 4-23).

What caused the observed differences in deep water response between the two hurricanes? It appears that the observed strong deep water response to Hurricane Katrina was the result of barotropic oceanic response to the elevated sea surface within the hurricane's eye wall. In response to the very low central pressure at the center of Hurricane Katrina (Figure 4-3), sea surface near the center of the hurricane could have been elevated by as much as 90 cm. As a result, significant barotropic response is expected in the ocean all the way to the bottom particularly within the hurricane's eye wall (Chang, 1985). Apparently, the mooring was able to capture this barotropic oceanic response during the passage of Hurricane Katrina while the mooring was simply too distant from the center of Hurricane Rita during its passage. This observation raises an intriguing question. As previously noted (Lewis and Hsu, 1992), GOM is a region preferred by tropical storms and hurricanes partly due to the presence of warm water in the LC and LCEs. Moreover, the presence of warm water within GOM even during the winter season gives rise to numerous formations of extra-tropical storms (Hsu, 1993). Consequently, those tropical and extra-tropical storms could force significant barotropic oceanic response in deep water all the way to the bottom within the paths of those storms. Although the width of footprint of each storm is limited, simply due to the large number of tropical and extra-tropical storm occurrences within GOM, this could represent another important mechanism by which to transmit significant energy to deep water in the GOM, thus contributing to deep water energetics and its well-mixed deep water conditions.

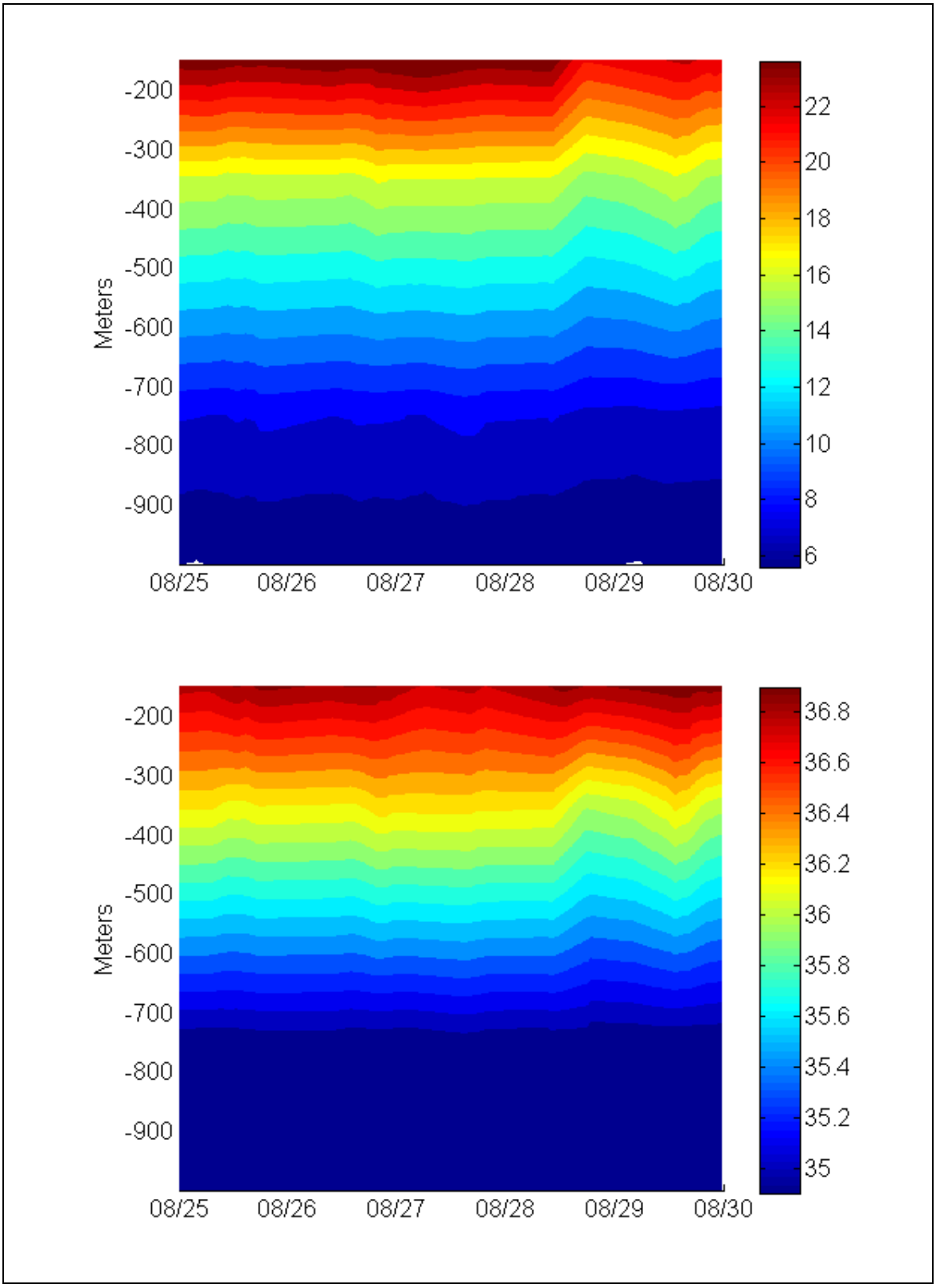

Figure 4-17. Depth-corrected temperature (top) and salinity (bottom) from Microcats at 145 m, 350 m, 750 m, and 1000 m.

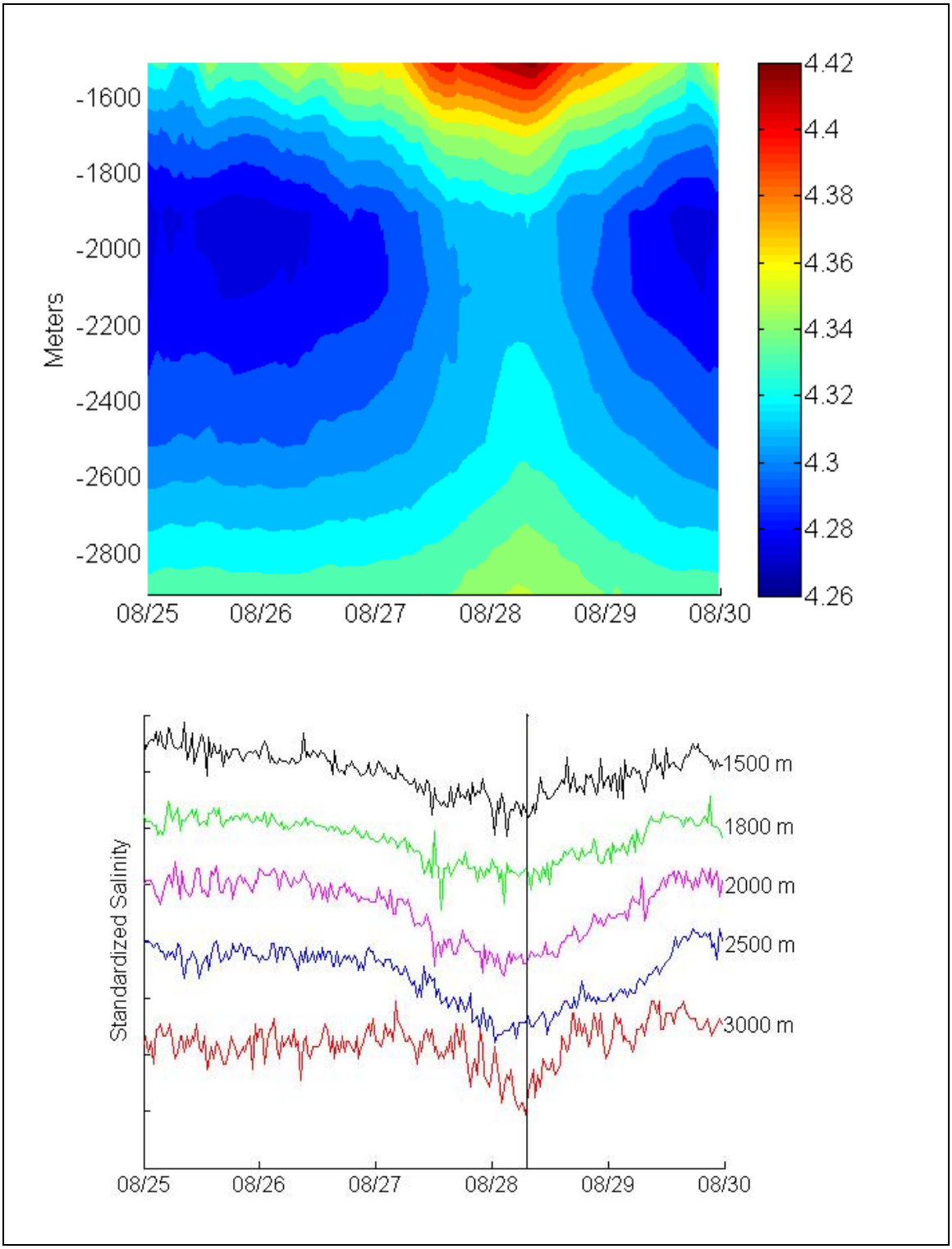

Figure 4-18. Depth-corrected temperature (top) and standardized salinity (bottom) from Microcats at 1500 m, 1800 m, 2000 m, 2500 m, and 3000 m.

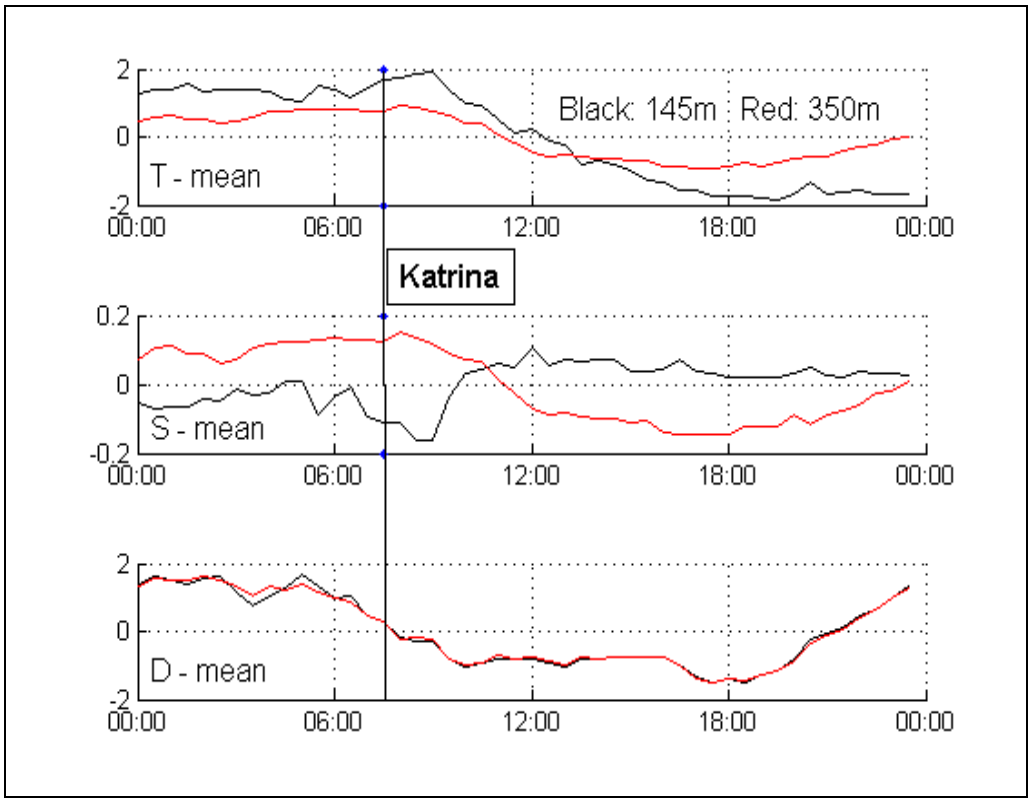

Figure 4-19. Demeaned temperature (top), salinity (middle), and depth (bottom) recorded by Microcats at 145 m (black line) and 350 m (red line) on August 28, 2005. The time of closest approach of Hurricane Katrina is indicated by the solid black line.

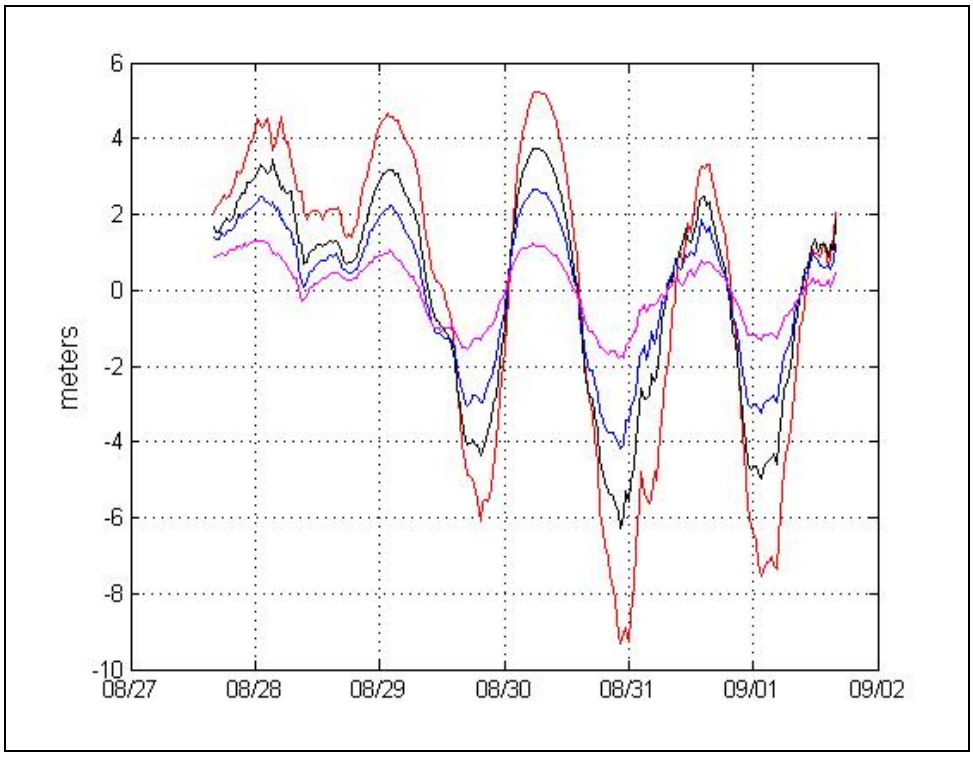

Figure 4-20. Demeaned time series of depth from the Microcats at 145 m (red), 350 m (black) 750 m (blue) and 1000 m (magenta).

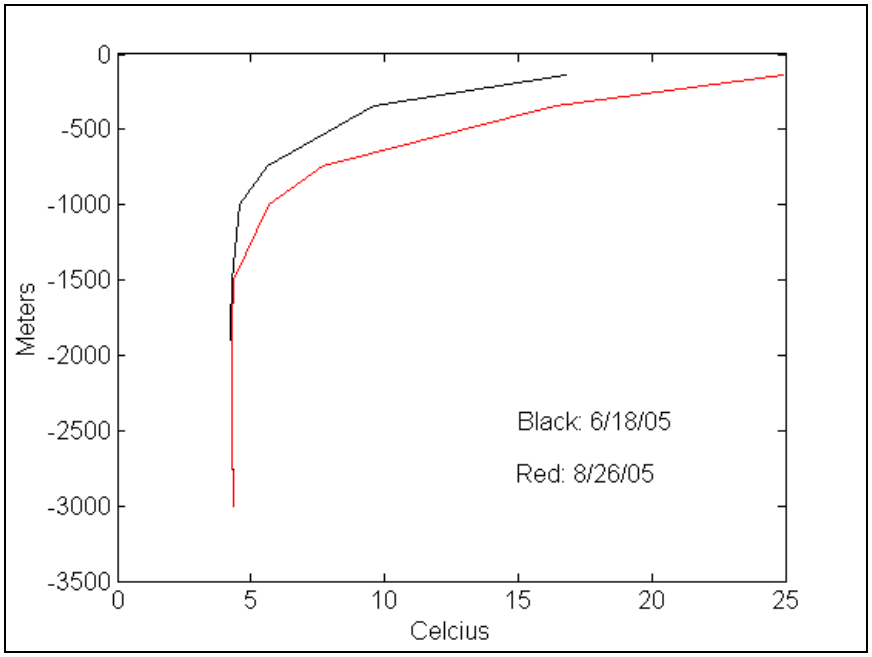

Figure 4-21. Vertical temperature profiles from Microcats on June 18, 2005 (outside of the LC) and August 26, 2005 (within the LC).

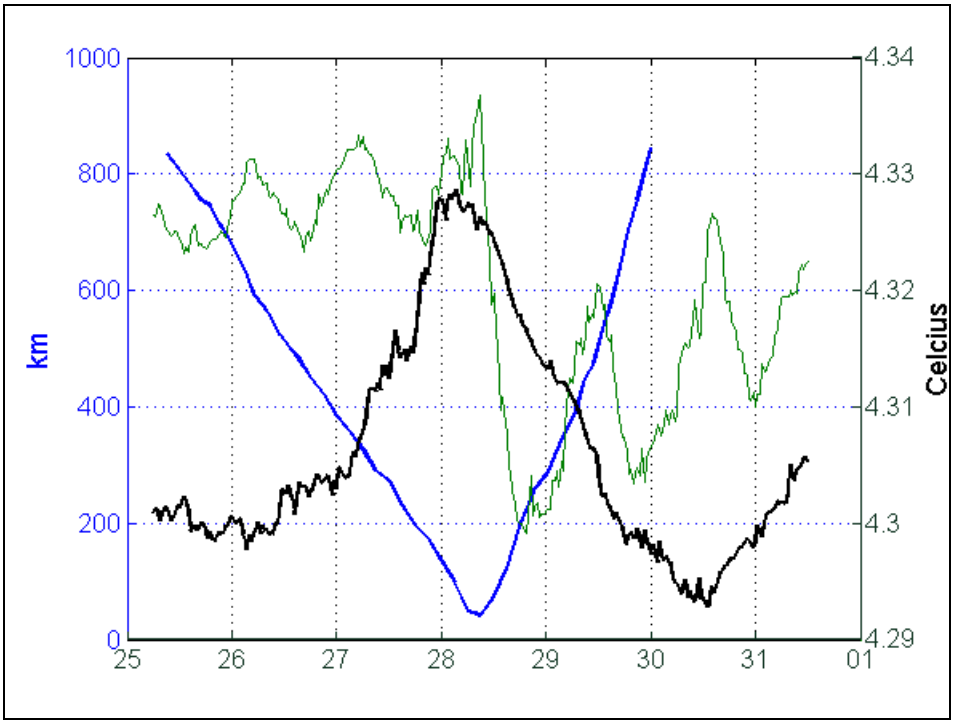

Figure 4-22. Distance from Hurricane Katrina to the mooring (blue), temperature at 2500 m (black), and scaled temperature at 145 m (green).

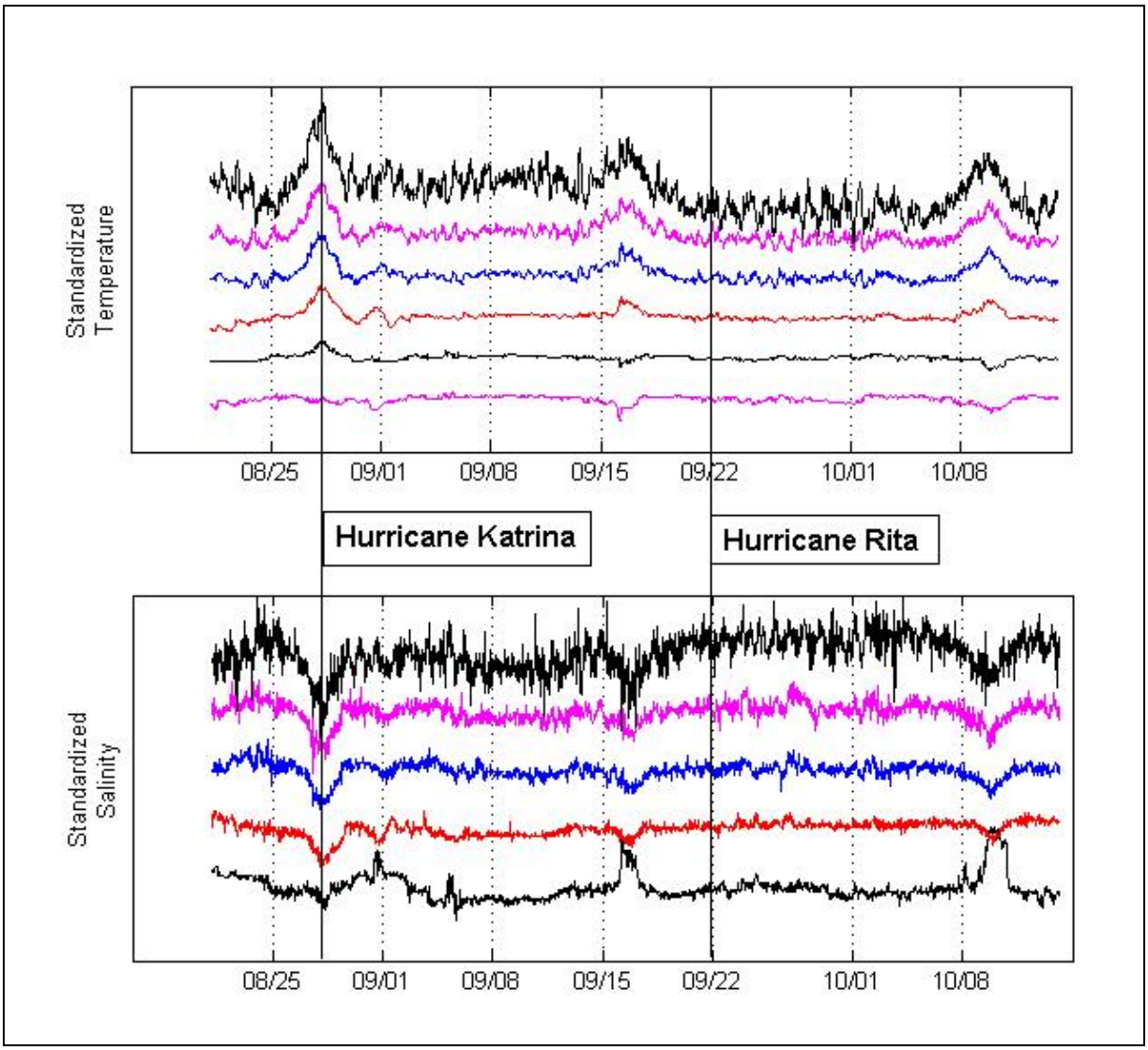

Figure 4-23. Standardized temperature (top) and salinity (bottom): 1500 m (black), 1800 m (magenta), 2001 m (blue), 2500 m (red), 3001 m (black), and 3200 m (magenta – temperature only). The time series are standardized by subtracting the mean for time period shown from each record and then adding a constant in time to separate the records on the plot.

4.2 Hurricane Rita

Hurricane Rita reached peak intensity between 03:00 and 06:00 UTC on 9/22/05, which coincided with the time that Rita was closest to the mooring (Figure 4-24). During this interval, the maximum wind speed reached 175 mph and the minimum pressure was estimated to be 895 mbar (Knabb et al., 2006). The eye diameter was estimated to be 20 n mi (37 km) (Knabb et al., 2006) at 00:00 UTC, reducing to 16 n mi (30 km) at 06:00 UTC. The mooring remained outside of the eye wall and the center of Hurricane Rita was 98.63 km from the mooring at 03:00. Between 3 and 6 hours after closest approach to the mooring, Hurricane Rita began to weaken (Figure 4-24).

The magnitude of the current response was similar for the two hurricanes, although the direction of the currents was nearly opposite. During Katrina, the northwestern branch of the LC was flowing over the mooring (Figure 4-6). Eddy Vortex separated a final time from the LC around September 18, 2005, only a few days before Rita made its closest approach. On September 22, 2005, the mooring was situated in the southward flowing eastern branch of the LC and due to the nearly closed contours of SSH, it looked as though another eddy was forming (Figure 4-25). The paths of Katrina and Rita were very similar, although the path of Rita was farther to the west (Figure 4-1). The wind shift as the hurricanes passed was essentially the same, but the direction of the winds relative to the currents was opposite.

The upper layer current response measured by the downward looking ADCP at 140 m and current meters at 250 m, 350 m, 450 m, 600 m, and 750 m was somewhat similar to Hurricane Katrina (Figure 4-26). A packet of internal oscillations is observed to propagate downward for approximately 10 days following the closest approach of Rita, but we don't see the repeating packets that followed Katrina. Also the packets don't penetrate as deeply following Rita. From both the velocity vector plots (Figure 4-27) and progressive vector diagrams (Figure 4-28) corresponding to Rita, it is apparent that the amplitude of the inertial oscillations is also smaller following Rita than Katrina. The signature of the inertial oscillations is likely different due to the direction of the background flow. There is only a slight accentuation of the inertial oscillations in the vector plots at 600 m immediately following Rita, but the oscillatory nature of the inertial motion at 600 m can be seen in the PVD of the demeaned currents in Figure 4-29.

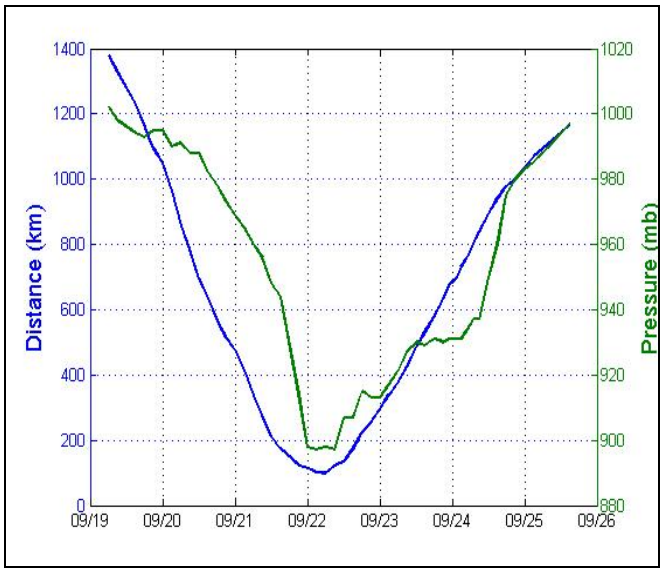

Figure 4-24. Distance (km) from Hurricane Rita to the mooring and central pressure (mb) for Hurricane Rita (Source: Johns Hopkins Applied Physics Laboratory Ocean Remote Sensing web site: http://fermi.jhuapl.edu/hurr/05/rita/rita.txt)

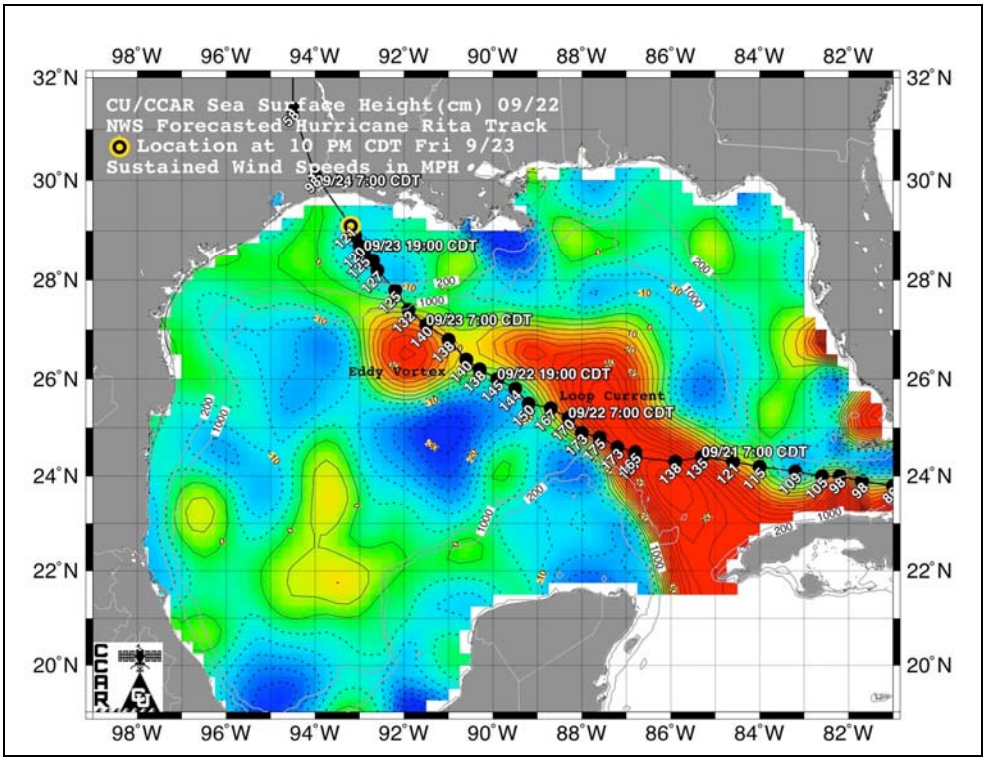

Figure 4-25. Sea surface height map from September 22 is shown overlaid with the path and maximum sustained winds reported for Hurricane Rita by NOAA's National Weather Service from Leben et al. (2006).

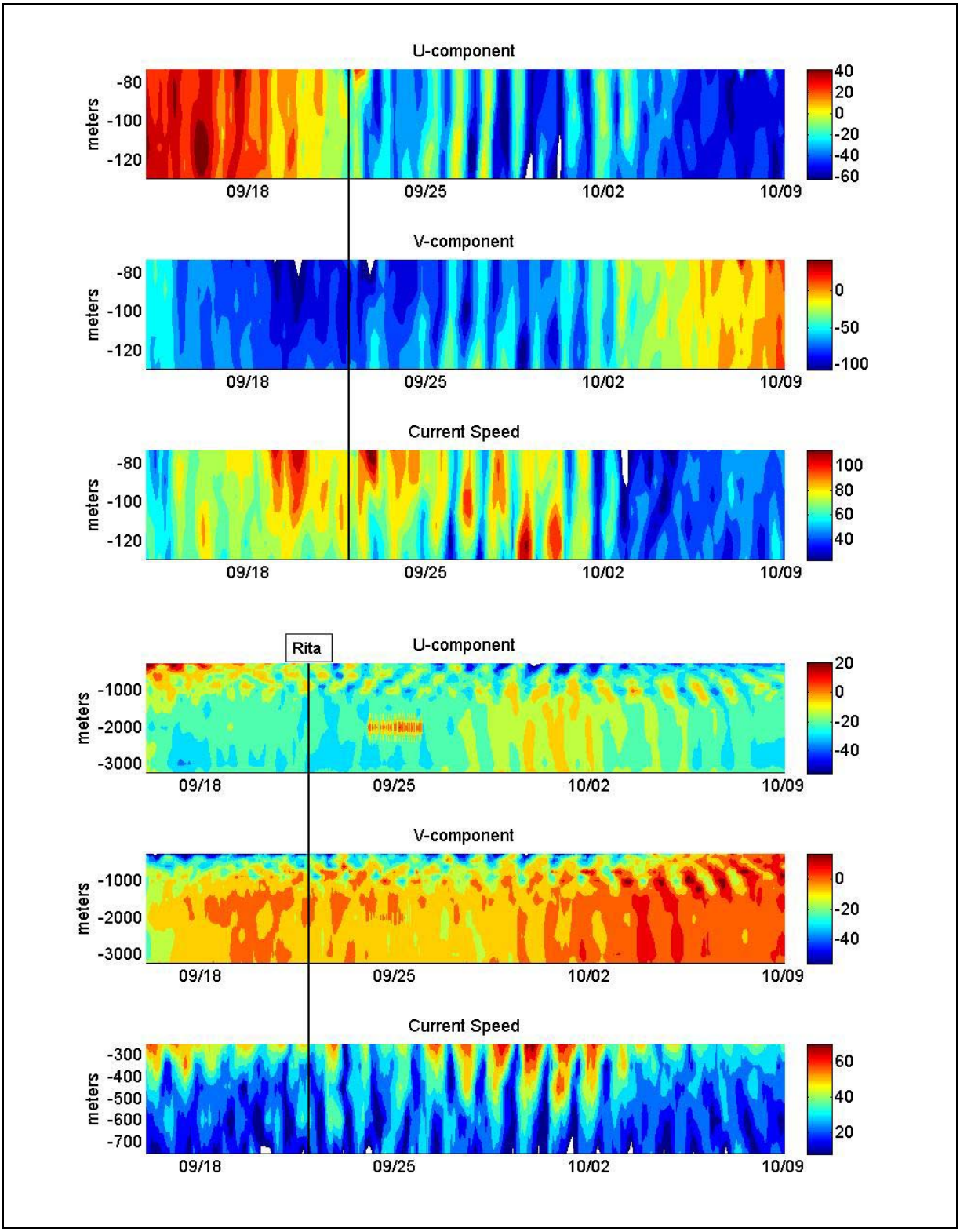

Figure 4-26. Contours of the U-component, V-component, and magnitude of velocity for the upper 140 m from ADCP (top) and for the water column below 250 m from current meters (bottom).

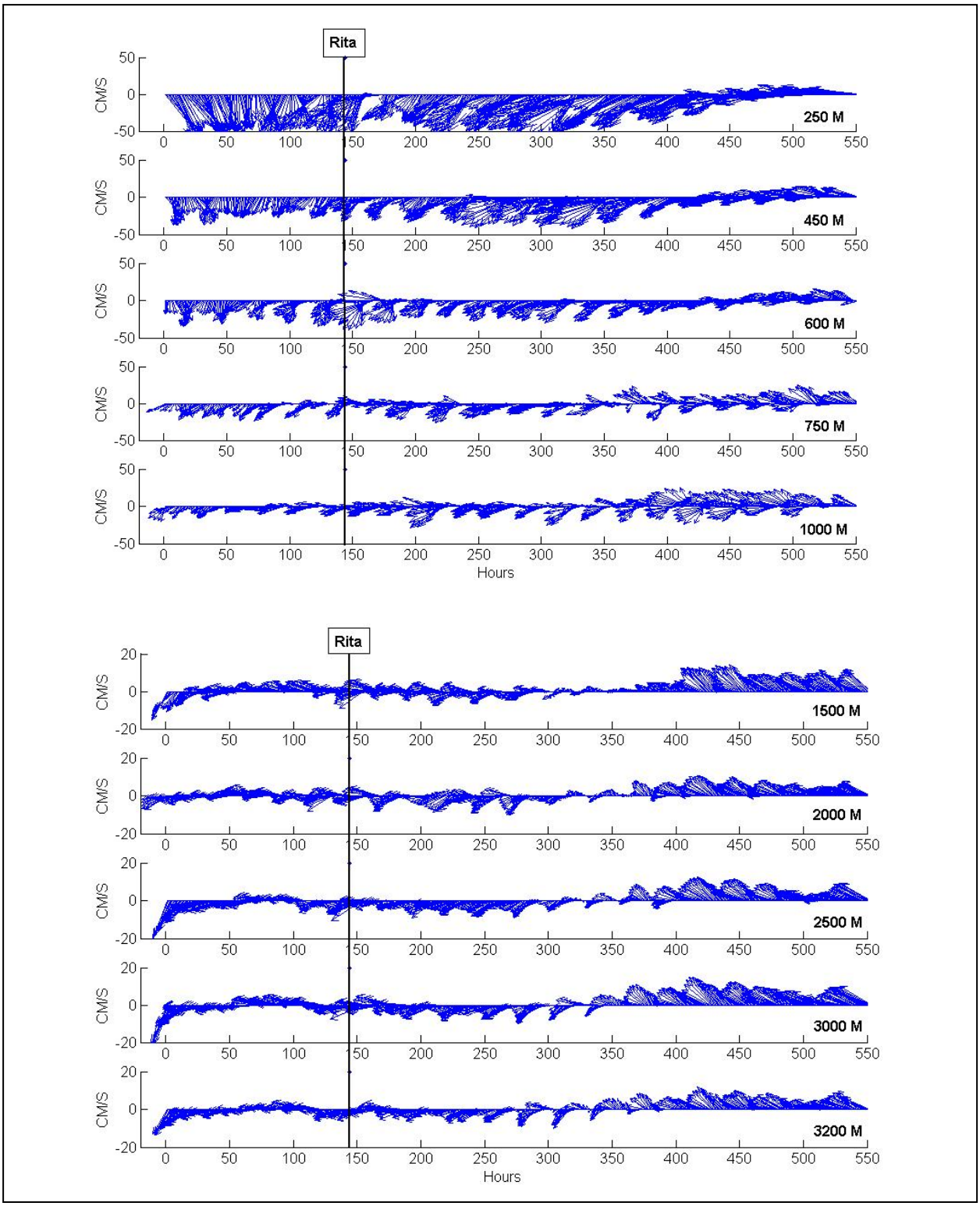

Figure 4-27. Upper (top) and lower (bottom) layer velocity vectors at the depths indicated for the same time period shown in Figure 4-17. Note the change of scale between upper and lower layers. The largest vectors are truncated in each panel.

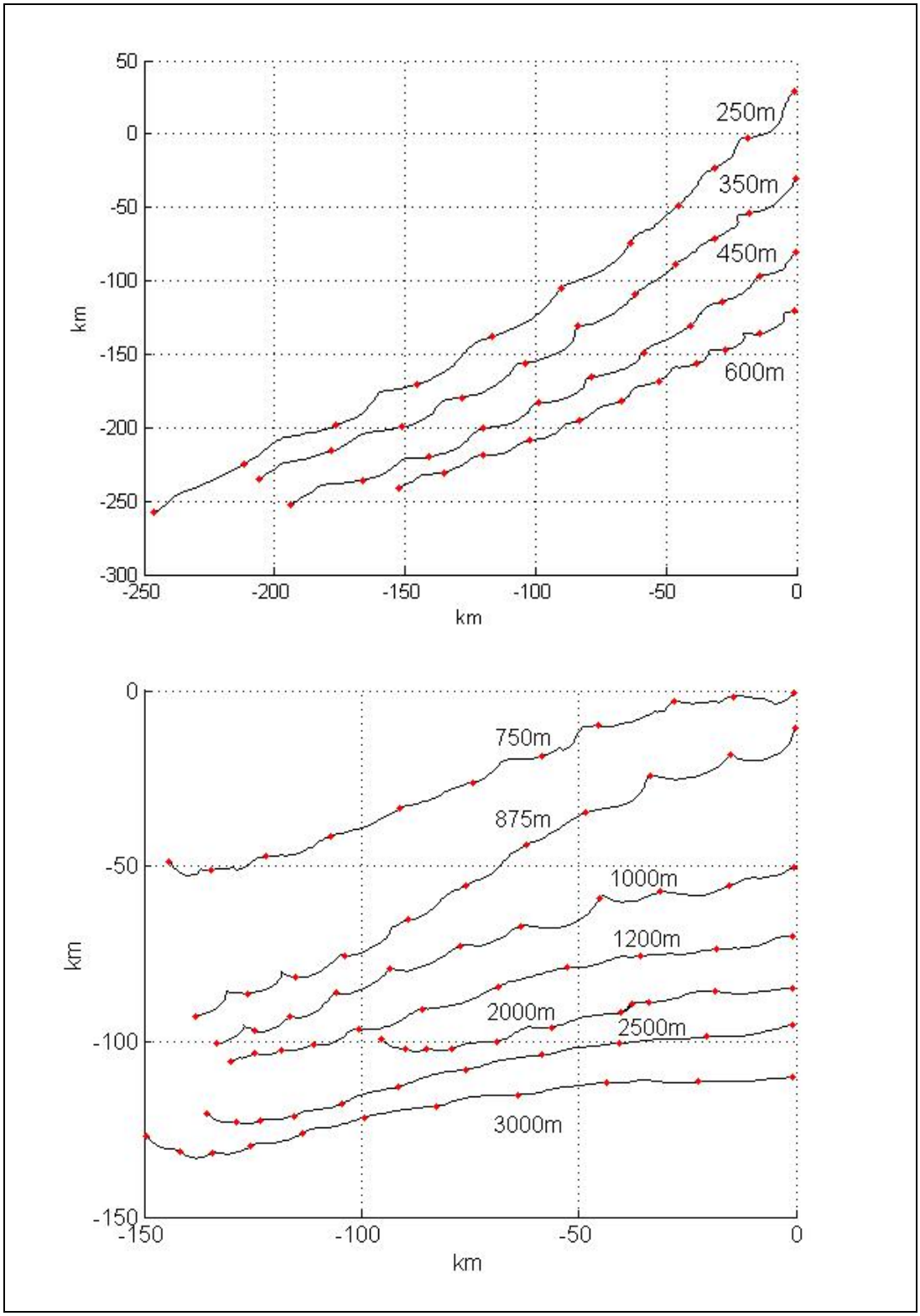

Figure 4-28. Progressive vector diagrams from the U- and V-components for 10 days from September 22, 2005, at 00:00 to October 2, 2005, at 00:00. The red '·' marks each 24hour segment.

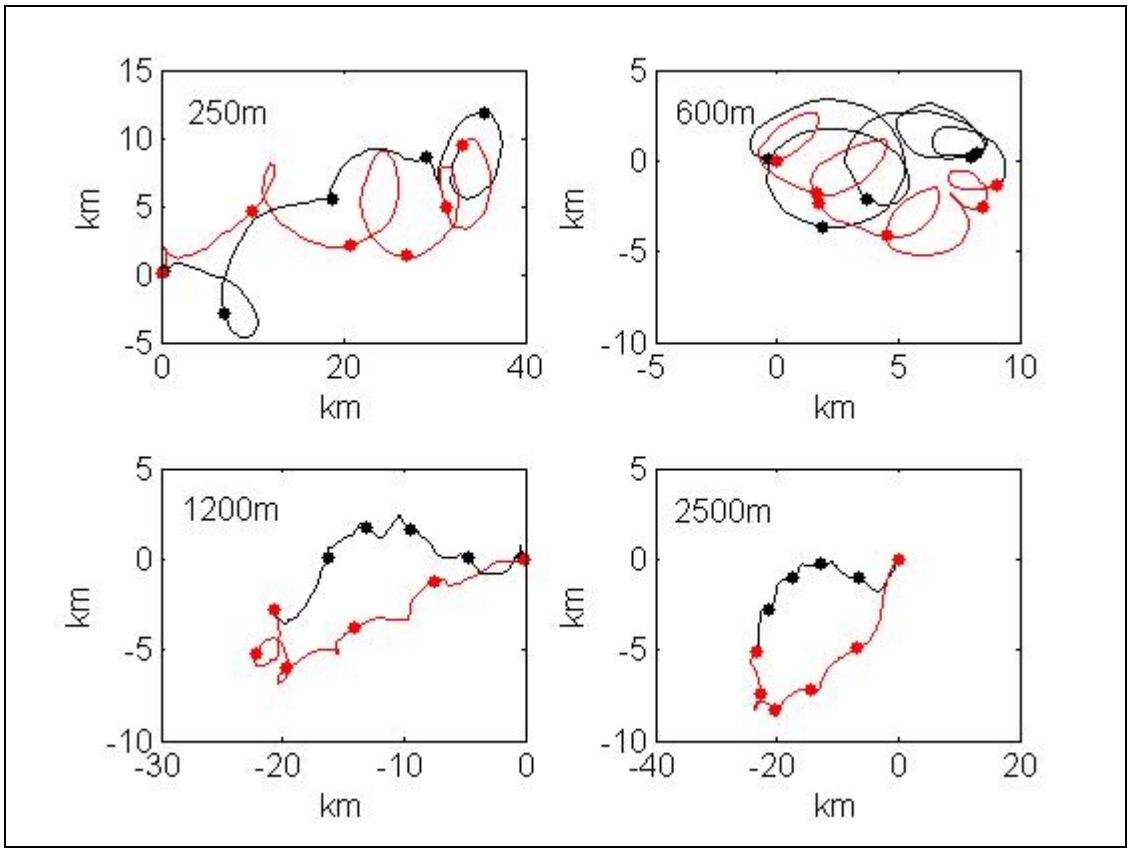

Figure 4-29. Progressive vector diagrams from demeaned time series of the U- and V-components. The dots mark each 24hour segment. The first 5 days are represented by a black line and the last 5 days are red.

4.3 Summary

Hurricanes Arlene (June 10), Dennis (July 10), Katrina (August 28), and Rita (September 22) have something in common - they all strengthened as they approached the mooring. Although Arlene was only a tropical storm, its winds increased from 60 mph to 70 mph as it neared the mooring. Dennis strengthened from a category 1 to a category 3 after entering the GOM on the north side of Cuba and Wilma strengthened from a category 2 to a category 3. The strengthening of Katrina and Rita is discussed above. The most significant factor in the strengthening of these storms is the reservoir of warm water associated with the LC in the southeast portion of the GOM. But it is also the LC that makes it difficult to isolate the effect of these storms on the water column at the mooring location. This is because for most of the hurricane season, the mooring was located within the strong upper layer flow associated with the LC (Figures 4-6 and 4-25). Hurricane Katrina was near enough and strong enough to have a measurable impact on the entire water column. It appears that the observed strong deep water response to Hurricane Katrina was the result of barotropic oceanic response to the elevated sea surface within the hurricane's eye wall. As previously noted, due to the presence of warm water in the LC and LCEs, GOM is a region preferred by tropical storms (Lewis and Hsu, 1992) and extra-tropical storms (Hsu, 1993). Those tropical and extra-tropical storms could force significant barotropic oceanic response in deep water all the way to the bottom within the paths of those storms. Although the width of footprint of each storm is limited, simply due to the large number of tropical and extra-tropical storm occurrences within GOM, this could represent another important mechanism by which to transmit significant energy to deep water in the GOM, thus contributing to deep water energetics and its well-mixed deep water conditions.

CHAPTER 5

SUMMARY AND CONCLUSIONS

5.1 Summary of Observations and Modeling

A total of five deployments of a deep water mooring at the center of the eastern GOM have produced the first observations of manifestations of the LC and LCEs in the eastern GOM away from the rough topographic region of the northern GOM. The mooring location turned out to be ideal in monitoring the LC in the eastern GOM. For most of the time the mooring remained in side the LC. Moreover, the mooring appears to be able to capture signal associated with every LCEs formed during the duration of the deployments. The observed flow field at the mooring site can be characterized as a two-layer system with the upper-layer flow dominated by the LC and LCEs the lower-layer flow dominated by smaller-scale deep water eddies. As a result, predominant time-scales of energy peak in the upper-layer are 50-120 days associated with migration of the LC in the eastern GOM, while the lower-layer showed energy peaks between 20 and 40 days. Current ellipses in deep water are more isotropic compared to those in the upper-layer, suggesting that the observed shorter-duration current variability in deep water is manifestation of smaller-scale deep water eddies. The interface between the upper- and lower-layers appears to be located between 800 m and 1000 m. Strongest near-surface currents peaked > 3.5 knots coinciding with the passage of the frontal jet in the LC. Upper-layer currents exhibit strong current shear reflecting the current structure within the LC. In contrast, lower-layer currents are nearly barotropic throughout the lower layer with typical current speeds averaging ~11 cm s^{-1}. However, short-duration current bursts in deep water were observed lasting a few days with maximum currents exceeding 30~40 cm s^{-1}. The strongest current burst in deep water with maximum currents exceeding 1 knot was observed during Deployment 3. Throughout the five deployments, deep water currents exhibited northward drift, suggesting that on average currents at the mooring site drift northward at speeds of 2-4 cm s^{-1}. Mean upper-layer currents displayed significant year-to-year variability, reflecting changing location of the mooring relative to the LC that is dominated by the LC ring formation with significant power near 5, 9, and 11 months (Sturges and Leben 2000; Leben 2005). It appears that the mooring was located west of the LC frontal jet during Deployments 1, 2 and 5 while it was located east of the LC frontal jet during Deployments 3 and 4.

Decoupling of the upper- and lower-layer currents was typical while occasional coupling between the two layers was observed. In particular, strong northward flowing barotropic currents were observed at the time of extreme northward extension of the LC preceding the formation of LCEs. Those short-duration events lasted only a few days. However, the observed barotropic currents penetrated all the way to the bottom. The observed current variability and its associated T & S variability in deep water suggest that the idea of “a modon pair” in deep water appears to fit the observations at the mooring site, deep water currents driven by the vertical excursion of the interface between the upper- and lower-layers associated with the formation of LCEs. This appears to be the primary mechanism by which to transmit energy from the upper-layer to deep water especially below the sill depths at the Yucatan Channel (1900 m). This appears to drive smaller-scale deep water eddies. The observed smaller scales associated with deep water eddies are a result of eddy-topographic interaction as well as eddy-eddy interaction in

deep water. In this respect, the presence of the topographic constriction located in the central GOM is crucial in that it prohibits free propagation of eddies from the eastern GOM toward the west, thus contributing toward cascading of eddy energy toward smaller scales.

Fortunately Deployment 4 resulted in the discovery of another mechanism by which to transmit energy into deep water in the GOM. During its close encounter with Hurricane Katrina, the mooring detected significant deep water response to the passage of the hurricane. Similar response was not observed during the passage of Hurricane Rita. It appears that the observed energetic deep water response to Hurricane Katrina was the result of barotropic oceanic response to the elevated sea surface in accordance with the lower pressure distribution within the eye wall of the hurricane. It is noted that primarily due to the presence of warm water associated with the LC and LCEs throughout the year, the conditions in the GOM are favorable for the formation of tropical (Lewis and Hsu 1992) as well as extra tropical storms (Hsu 1993). Those tropical and extra-tropical storms could force notable barotropic oceanic response in deep water all the way to the bottom within the paths of those storms. Although the footprints of those storms are limited, simply due to the large number of those storm occurrences within GOM, this could represent another important mechanism by which to transmit significant energy to deep water in the GOM, thus contributing to its well-mixed deep water conditions.

These latest model simulations featuring very high horizontal (.075^{o}) and vertical (100 levels) resolution allowed more realistic representation of the bottom topography including the gentle rise and the steep escarpments. Consequently, it resulted in more realistic simulation of deep water currents in the eastern GOM, i. e., more energetic deep water and more chaotic eddy field in deep water, consistent with the observation at the mooring site. It appears that the small grid spacing in both the horizontal and vertical are necessary to resolve deep eddy interaction with the bathymetry in the GOM. The resulting eddy-eddy and eddy-topography interaction give rise to the observed energetic and chaotic flow field deduced from the mooring data, making clear identification of “a modon pair” in deep water in the eastern GOM problematic. This is consistent with the conclusions of Chérubin et al. (2005) who used the MICOM model to study the deep circulation in the eastern GOM.

The high resolution model clearly suggests that the cold and salty inflowing Caribbean water over the Yucatan sill sinks and manifests itself as a cold and salty tongue characteristic of the cyclonic deep circulation flowing along the periphery of deep water in the GOM. Eddy-eddy and eddy-topography interaction in the eastern GOM often removes the cold and salty water and advects it toward the interior region of the eastern gulf and further mixing with the ambient water tales place. The mooring was able to pick up signals associated with the advection of cold and salty water.

5.2 Conclusions

It appears that the LC and LCEs drives deep water currents in the eastern GOM. A modon pair forms underneath the LC when the LC makes northward extension prior to the formation of an LCE. However, eddy-eddy and eddy-topography interaction due to the topographic constriction in the central gulf and the limited size of the eastern basin make clear

identification of "a modon pair" problematic. The observations of currents and water mass characteristics at the mooring site appear to be consistent with the Cushman-Roisin et al. (1990) mechanism for the generation of the deep anticyclone-cyclone pair beneath the LC. This mechanism is based on the conservation of potential vorticity in the lower layer underneath the LC as the LC moves on a β plane. As the LC moves, anticyclonic vorticity develops underneath the eddy due to the squeezing of the lower layer while cyclonic vorticity develops toward the trailing edge of the eddy as the lower layer is being stretched. It should be noted that Hurlburt and Thompson (1980) demonstrated that in their two-layer model of GOM, barotropic instability plays a crucial role in the formation of anticyclone-cyclone pair in the lower layers. Chérubin et al. (2005) suggested that a combination of the two mechanisms (Cushman-Roisin et al. (1990) and Hurlburt and Thompson (1980)) is involved in the LC ring formation in the eastern GOM. It is very likely that barotropic instability plays a part in the formation of modons in deep water in the eastern GOM in addition to the Cushman-Roisin et al. (1990) mechanism. Regardless of the formation mechanism, the mooring observations appear to fit the modon pair formation underneath the LC. Another mechanism to transmit significant energy to deep water in the GOM is barotropic oceanic response to elevated sea surface near the center of tropical and extra-tropical storms often observed in the GOM. Simply due to the large number of those storm occurrences within GOM, this could represent another important forcing mechanism to transmit significant energy to deep water in the GOM, thus contributing to deep water energetics and the well-mixed deep water conditions.

The formation of modons as the interface moves up and down with the northward penetration of the LC and subsequent shedding of LC rings was clearly visible in the coarse resolution models. As the model grid resolution increases, so does the eddy-eddy interaction and the eddy-topographic interaction. How do we know that the process of modon formation is occurring in the high resolution model when the eddy field is so crowded and chaotic? As long as the surface expression of the LC ring remains far enough off the slope, the boundary between the anticyclonic and cyclonic circulation remains nearly fixed relative to the leading edge of the LC ring until the LC ring is in the western GOM. The boundary between the regions of anticyclonic and cyclonic flow is characterized as a southward jet. In all of the models with varying grid sizes, after a LC ring has migrated into the western GOM, the leading deep anticyclone dissipates first and the circulation becomes dominated by the deep cyclone. The effect of the westward migration of the deep eddy field is the net transport of vorticity into the western basin.

CHAPTER 6

REFERENCES

Bettway, M. 2006. NASA Technology Captures Massive Hurricane Waves. Goddard Space Flight Center, Greenbelt, MD. Internet website: http://www.nasa.gov/mission_pages/hurricanes/archives/2006/hurricane_waves.html.

Blake, E.S., E.N. Rappaport, and C.W. Landsea. 2007. The deadliest, costliest, and most intense United States tropical cyclones from 1851 to 2006 (and other frequently requested hurricane facts). NOAA Technical Memorandum NWS TPC-5. National Hurricane Center, National Weather Service, Miami, Florida. 43 pp. Internet website (last updated Apr 15, 2007): www.nhc.noaa.gov/Deadliest_Costliest.shtml.

Bryan, K. 1969. A numerical model for the study of the world ocean. J. Comput. Phys. 4:347-376.

Bunge, L., J. Ochoa, A. Badan, J. Candela, and J. Sheinbaum. 2002. Deep flows in the Yucatan Channel and their relation to changes in the Loop Current extension. J. Geophys. Res. 107:3233, doi:10.1029/2001JC001256.

Chang, S.W. 1985. Deep ocean response to hurricanes as revealed by an ocean model with free surface. Part I: Axisymmetric case. J. Phys. Oceanogr. 15:1847-1858.

Cherubin, L.M., W. Sturges, and E.P. Chassignet. 2005. Deep flow variability in the vicinity of the Yucatan Straits from a high-resolution numerical simulation. J. Geophys. Res. 110:C04009, doi:10.1029/2004JC002280.

Cione, J.J. and E.W. Ulhorn. 2003. Sea surface temperature variability in hurricanes: implications with respect to intensity change. Mon. Wea. Rev., 131:1783-1796.

Conkright, M.E., S. Levitus, T. O'Brien, T.P. Boyer, C. Stephens, D. Johnson, L. Stathoplos, O. Baranova, J. Antonov, R. Gelfeld, J. Burney, J. Rochester, and C. Forgy. 1998. *World Ocean Database 1998* documentation and quality control. National Oceanographic Data Center, Silver Spring, MD.

Cox, M.D. 1984. A primitive equation three-dimensional model of the ocean, Tech. Rep. 1, GFDL, NOAA, Princeton Univ., Princeton, N.J.

Cushman-Roisin, B., E.P. Chassignet, and B. Tang. 1990. Westward motion of mesoscale eddies. J. Phys. Oceanogr., 20:758-768.

DeHaan, C.J., and W. Sturges. 2005. Deep cyclonic circulation in the Gulf of Mexico. J. Phys. Oceanogr., 35:1801-1812.

Elliot, B.A. 1982. Anticyclone rings in the Gulf of Mexico. J. Phy. Oceanogr., 12:1292-1309.

Gordon, A.L. 1967. Circulation of the Caribbean Sea. J Geophys. Res., 72(4): 6207-6223.

Hellerman, S., and M. Rosenstein. 1983. Normal monthly wind stress over the world ocean with error estimates. J. Phy. Oceanogr., 13:1093-1104.

Hsu, S.A. 1993. The Gulf of Mexico – A breeding ground for winter storms. Marine Weather Log, Spring 1993. Pp. 4-11.

Hurlburt, H.E. and J.D. Thompson. 1980. A numerical study of Loop Current intrusions and eddy shedding. J. Phys. Oceanogr. 10:1611-1651.

Inoue, M., S.E. Welsh, L. J. Rouse, Jr., and E. Weeks. 2008. Deepwater currents in the Eastern Gulf of Mexico: Observations at 25.5°N and 87°W. U.S. Dept. of the Interior, Minerals Management Service, Gulf of Mexico OCS Region, New Orleans, LA. OCS Study MMS 2008-001. 86 pp.

Johns, W.E., T.L. Townsend, D.M. Fratantoni, and W.D.Wilson. 2002. On the Atlantic inflow to the Caribbean Sea. Deep-Sea Res. I 49:211-243.

Knabb, R.D, J.R. Rhome, and D.P. Brown. 2006. Tropical cyclone report: Hurricane Katrina 23-30 August 2005. National Hurricane Center, Miami, FL. Internet website: http://www.nhc.noaa.gov/pdf/TCR-AL122005_Katrina.pdf.

Kundu, P.K. 1986. A two-dimensional model of inertial oscillations generated by a propagating wind field. J. Phys. Oceanogr. 16:1399-1411.

Leben, R.R. 2005. Altimeter-derived Loop Current metrics. In: Sturges, W. and A. Lugo-Fernandez, eds. Circulation in the Gulf of Mexico: Observations and models. Geophys. Monogr., Vol. 161, Amer. Geophys. Union. Pp.181-201.

Leben, R.R, G.H. Born, and M. Srinivasan. 2006. Satellite altimetry outreach during Hurricane Rita: Lessons learned. 15 years of progress in radar altimetry progress. Ocean surface topography science team (OSTST) meeting. International Doris Service (IDS) Workshop. ARGO Workshop. Venice 13-18 March 2006. Internet website: http://earth.esa.int/workshops/venice06/participants/995/paper_995_leben.pdf.

Lewis, J.K. and S.A. Hsu. 1992. Mesoscale air-sea interactions related to tropical and extra-tropical storms in the Gulf of Mexico. J. Geophys. Res., 97(C2):2215-2228.

Maul, G.A., D.A. Mayer, and S.R. Baig. 1985. Comparison between a continuous three-year current meter observation at the sill of the Yucatan Strait, satellite measurements of the Gulf Loop Current area, and regional sea level. J. Geophys. Res. 90:9089-9096.

McLellan, H.J. and W.D. Nowlin. 1963. Some features of the deep water in the Gulf of Mexico. J. Mar. Res. 21:233-245.

Morey, S.L., M.A. Bourassa, D.S. Dukhovskoy, and J.J. O'Brien. 2006. Modeling studies of the upper ocean response to a tropical cyclone. Ocean Dynamics DOI 10.1007/s10236-006-0085-y.

Morozov, E.G. and M.G. Velarde. 2008. Inertial oscillations as deep ocean response to hurricanes. J. Oceanography. 64:495:509.

Oey, L.-Y. 1996. Simulation of mesoscale variability in the Gulf of Mexico: Sensitivity studies, comparison with observations, and trapped wave propagation. J. Phys. Oceanogr. 26:145-175.

Oey, L-Y., T. Exer, and H.-C. Lee. 2005. Loop current, rings and related circulation in the Gulf of Mexico: A review of numerical models and future challenges. In: Sturges, W. and A. Lugo-Fernandez, eds. Circulation in the Gulf of Mexico: Observations and models. Geophys. Monogr., Vol. 161, Amer. Geophys. Union. Pp. 31-56.

Oey, L.-Y., M. Inoue, R. Lai, X.-H. Lin, S.E.Welsh, and L. Rouse, Jr. 2008. Stalling of near-inertial waves in a cyclone. Geophys. Res. Lett. 35:L12604, doi:10.1029/2008GL034273.

Pacanowski, R., K. Dixon, and A. Rosati. 1991. The GFDL Modular Ocean Model users guide version 1.0, GFDL Ocean Group Tech. Rep. 2, Princeton, NJ.

Price, J.F. 1981. Upper ocean response to a hurricane. J. Phys. Oceanogr. 11:153-173.

Rivas, D., A. Badan, and J. Ochoa. 2005. The ventilation of the deep Gulf of Mexico. J. Phys. Oceanogr. 35:1763-1781.

Romanou, A. and E.P. Chassignet. 2004. Gulf of Mexico circulation within a high-resolution numerical simulation of the North Atlantic Ocean. J. Geophys. Res. 109:C01003, doi:10.1029/2003JC001770.

Schmitt, R.W. 1981. Form of the temperature-salinity relationship in the Central Water: Evidence for double-diffusive mixing. J. Phys. Oceanogr. 11:1015-1026.

Schmitt, R.W. 1990. On the density ratio balances in the Central Water. J. Phys. Oceanogr. 20:900-906.

Schmitt, R. W., J. R. Ledwell, J.M. Toole, and K.L. Polzin. 2002. Initial results of the salt finger tracer release experiment. EOS. Transactions of American Geophysical Union 83(4):OS181.

Shay, L.K., P.G. Black, A.J. Marano, J.D. Hawkins, and R.L. Elsberry. 1992. Upper ocean response to Hurricane Gilbert. J. Geophys. Res. 97:20,227-20,248.

Smith, W.H.F. and D.T. Sandwell. 1997. Global sea floor topography from satellite altimetry and ship depth soundings. Science 277:1956-1962.

Stern, M.E. 1967. Lateral mixing of water masses. Deep-Sea Res. 14:747-753.

Sturges, W. 2005. Deep-water exchange between the Atlantic, Caribbean, and Gulf of Mexico. In: Sturges, W. and A. Lugo-Fernandez, eds. Circulation in the Gulf of Mexico: Observations and models. Geophys. Monogr., Vol. 161, Amer. Geophys. Union. Pp. 263-278.

Sturges, W., E. Chassignet, and T. Ezer. 2004. Strong mid-depth currents and a deep cyclone in the Gulf of Mexico. U.S. Dept. of the Interior, Minerals Management Service, Gulf of Mexico OCS Region, New Orleans, LA. OCS Study MMS 2004-040. 76 pp.

Sturges, W. and R. Leben. 2000. Frequency of ring separation from the Loop Current in the Gulf of Mexico: A revised estimate. J. Phys. Oceanogr. 30:1814-1819.

Sturges, W., J.C. Evans, S. Welsh, and W. Holland. 1993. Separation of warm-core rings in the Gulf of Mexico. J. Phys. Oceanogr. 23:250-268.

Welsh, S.E. 1996. A numerical modeling study of the Gulf of Mexico during present and past environmental conditions. Ph.D. dissertation, Louisiana State University, Baton Rouge, LA.

Welsh, S.E. and M. Inoue. 2000. Loop Current rings and the deep circulation in the Gulf of Mexico. J. Geophys. Res. 105(C7):16,951-16,959.

Welsh, S.E. and M. Inoue. 2002. Lagrangian study of the circulation, transport, and vertical exchange in the Gulf of Mexico: Final report. U.S. Dept. of the Interior, Minerals Management Service, Gulf of Mexico OCS Region, New Orleans, LA. OCS Study MMS 2002-064. 51 pp.

Worthington, L.V. 1977. On the North Atlantic circulation. Baltimore, MD:Johns Hopkins University Press. 110 pp.

Wust, G. 1964. Stratification and circulation in the Antillean-Caribbean Basins, Vol. 1. New York, NY:Columbia University Press. 201 pp.

APPENDIX A

HIGH-RESOLUTION MODEL DESCRIPTION

The general ocean circulation model used in this study was originally referred to as the "Bryan-Cox Model" and was formulated over 40 years ago (Bryan 1969; Cox 1984). As computer architecture and operating systems have evolved, so has the Bryan-Cox Model. The first version written for use with a UNIX system was The Modular Ocean Model version 1.0 (MOM1) (Pacanowski et al., 1991) was chosen for this project, although it did not feature the calculation of surface pressure and an implicit free-surface which were available in later versions. The model is able to simulate the dynamics of the LC system and the current-bathymetric interaction in the deep water, which are the physical processes of interest in this project.

The model grid was derived from the Global Sea Floor Topography with 2 minute horizontal resolution (Smith and Sandwell 1997). In order to simulate realistic deep cyclones, it was necessary to resolve important small-scale bottom topographic features, such as a narrow deep channel connecting the eastern and the central basins. The model grid has .075° horizontal resolution and 100 vertical levels that were scaled to feature higher resolution on the shelf and slope, while retaining adequate vertical spacing in deeper water. The vertical resolution is 20 m over the shelf and 40 m from the 200-m isobath to the bottom. Very fine horizontal resolution and equally-spaced vertical grid levels greatly reduce the potential for topographically-induced numerical noise in the model fields. The model domain extends outside the GOM and includes the entire Caribbean (Figure A-1).

The model was initialized with the World Ocean Atlas 2001 (WOA01) temperature and salinity fields (Conkright et al. 1998) over the entire model domain. The temperature and salinity in the surface level are also relaxed to climatology. The surface wind stress fields were interpolated from the Hellerman and Rosenstein (1983) monthly climatology. The seasonal cycle of freshwater inflow of the Mississippi is attained by relaxing the surface salinity to WOA01 monthly means. A natural inflow condition through the Yucatan Channel is accomplished by forcing the flow through the western Caribbean to acquire the observed seasonal variation in the shear and geostrophic transport of the Caribbean Current. The temperature and salinity are relaxed to WOA01 monthly climatology along a north-south cross-section centered at 66.5ºW. A constant is added to the u-component of velocity to adjust the total transport to reflect the inflow from the Lesser Antilles and the Anegada Passage. To the east of the geostrophic forcing region, the same method of inducing geostrophic flow is implemented at the Mona Passage and the Windward Passage. The model domain does not extend far enough outside of the Caribbean to be able to simulate the North Atlantic gyre or the thermohaline contribution from the South Atlantic. Therefore it was necessary to force flow into the Caribbean through the Mona and Windward passages to prevent leakage. The target transports through these passages were based on values reported by Johns et al. (2002). The 5-year average transport through the Yucatan Channel was 28.12 Sv. The 5-year average transport through the Windward Passage was 3.60 Sv, which is within the range of 3-9Sv (Johns et al. 2002). The 5-year average transport through the Mona Passage was 9.10 Sv, which was larger than desired, but was necessary to balance the

flow through the Yucatan Channel. Reduced transport in the Mona Passage resulted in lower than normal transport through the Yucatan Channel.

The model was spun-up for 9 years and then run another 4 years for analyses. The timestep was 90 minutes and the viscosity and diffusivity were each 60 m^2 s^{-1}. The coefficient for surface relaxation of temperature and salinity was 8 weeks and the coefficient for relaxing the T and S along the inflow cross-sections is 4 weeks. A snapshot of all model variables was saved every month. The horizontal temperature, salinity, velocity, and stream function were saved every day for every 10^{th} vertical grid level. Animations of the model fields may be viewed on a CD that accompanies the digital copies of this report.

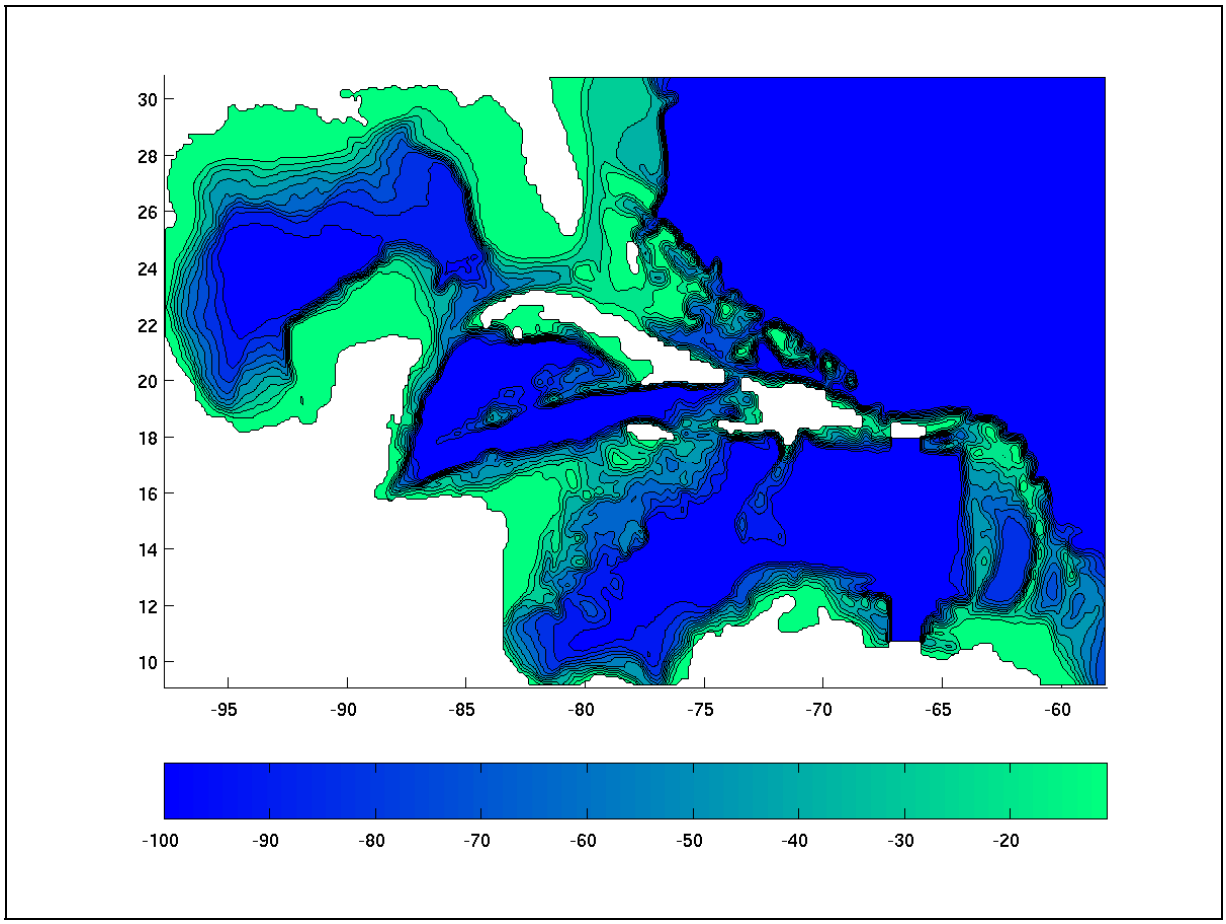

Figure A-1. High-resolution model grid of the Gulf of Mexico and Caribbean using 0.075° horizontal grid spacing and 100 vertical levels. The 10 solid contour lines excluding the coastline represent every 10th vertical grid level.

APPENDIX B

MONTHLY SSH MAPS OF THE GULF OF MEXICO FOR DEPLOYMENTS 4 AND 5

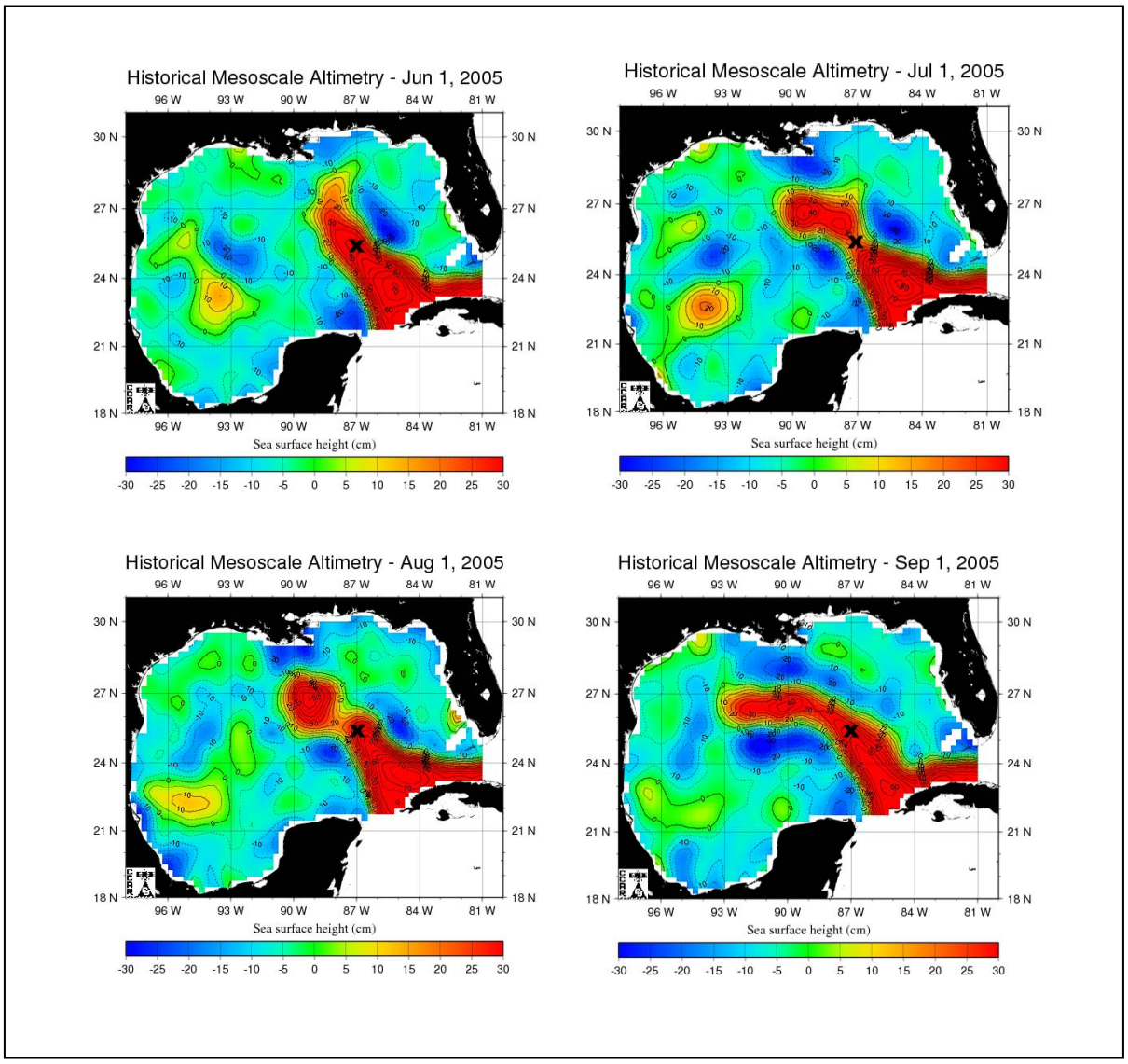

Figure B-1. Sea surface height maps for each month during Deployments 4 and 5 plotted from mesoscale altimetry data archived by Dr. Robert Leben at the University of Colorado.

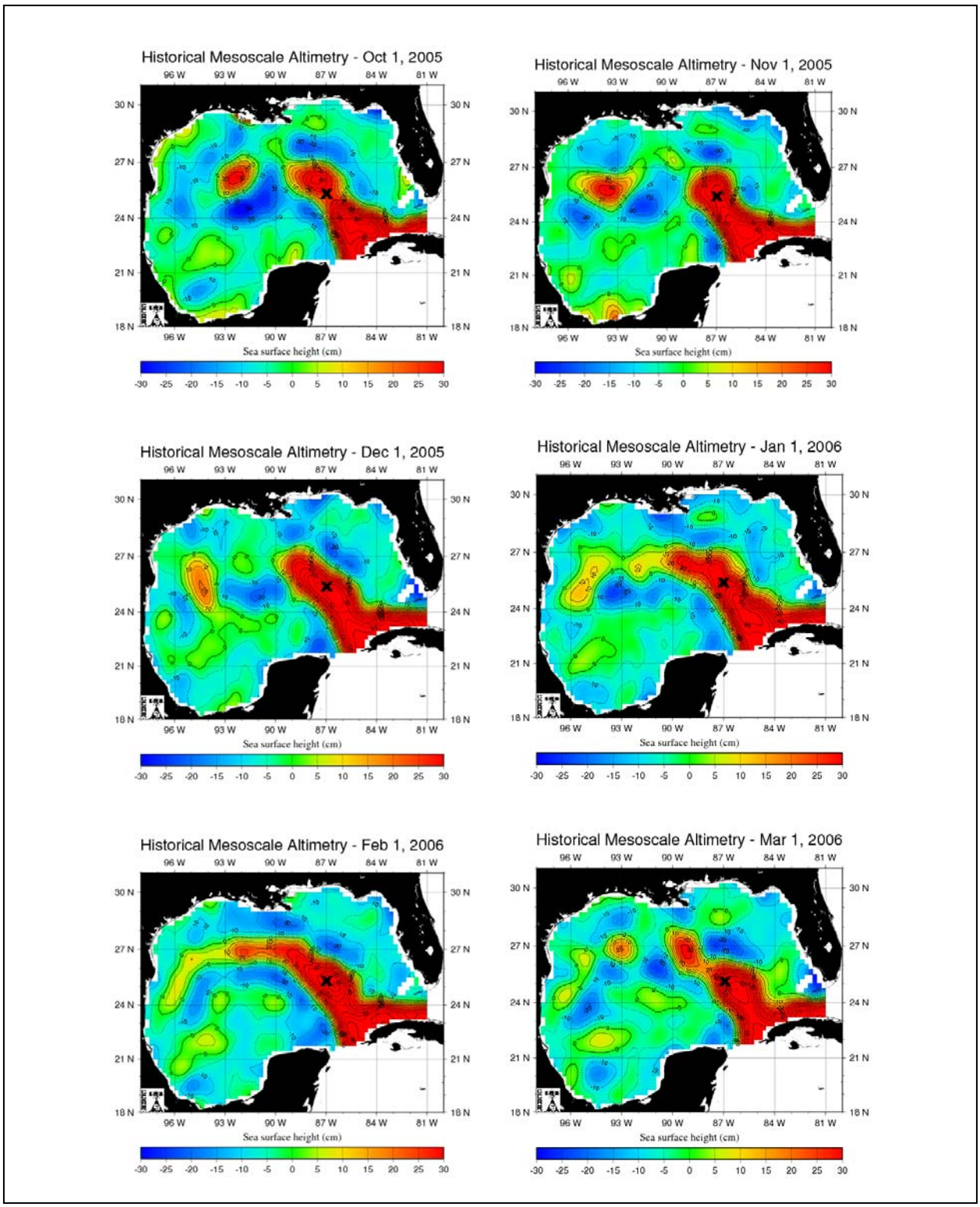

Figure B-1. Sea surface height maps for each month during Deployments 4 and 5 plotted from mesoscale altimetry data archived by Dr. Robert Leben at the University of Colorado (continued).

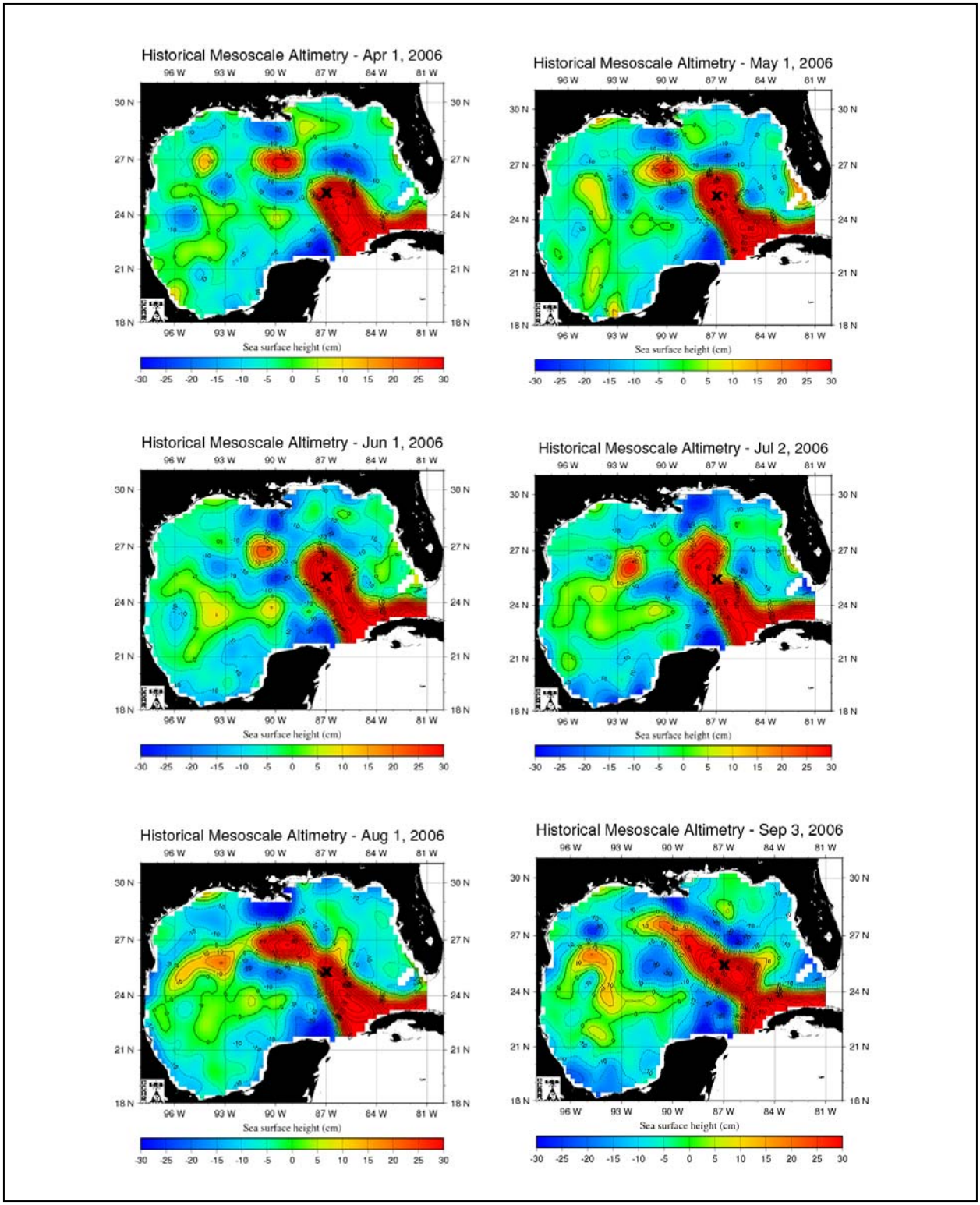

Figure B-1. Sea surface height maps for each month during Deployments 4 and 5 plotted from mesoscale altimetry data archived by Dr. Robert Leben at the University of Colorado (continued).

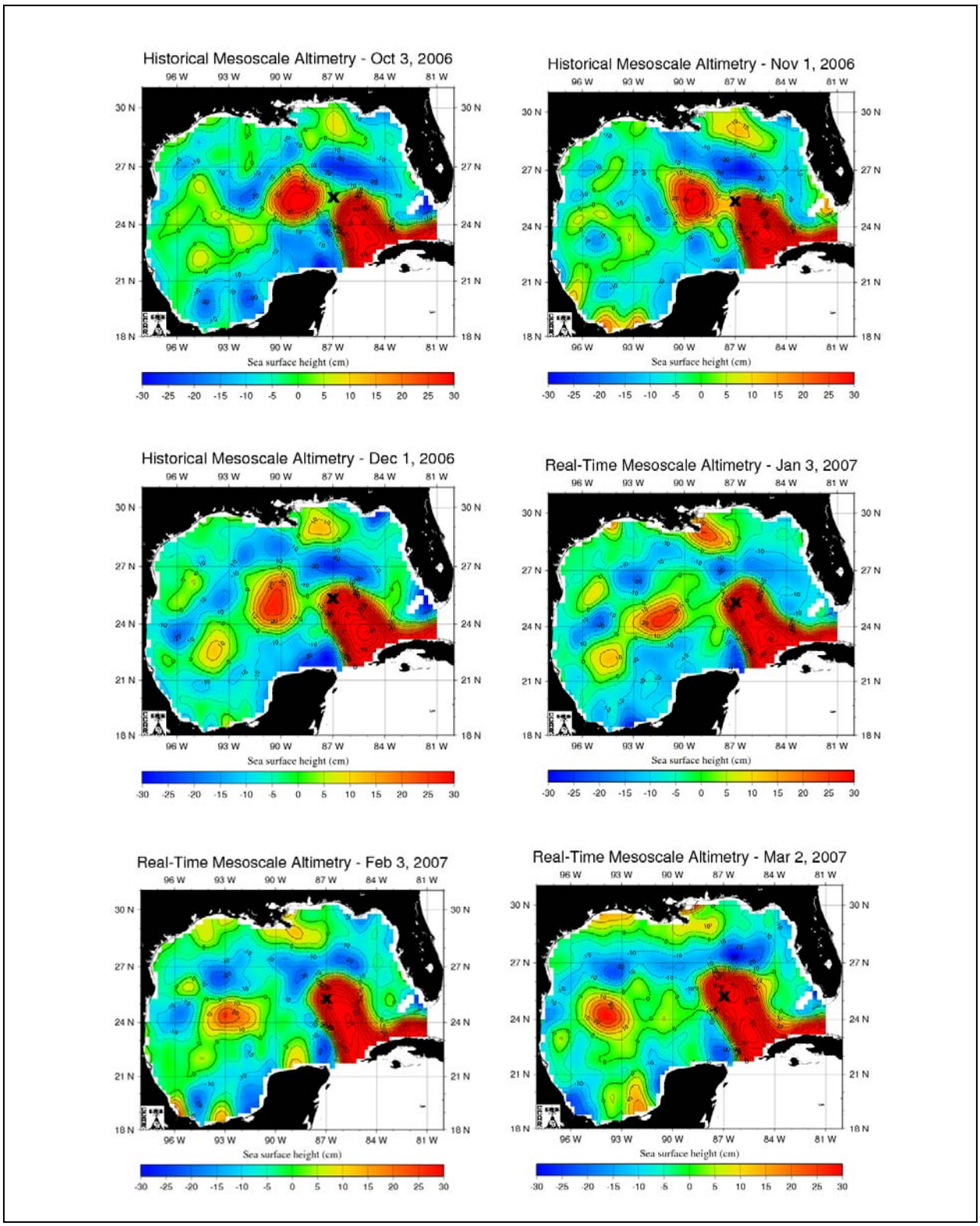

Figure B-1. Sea surface height maps for each month during Deployments 4 and 5 plotted from mesoscale altimetry data archived by Dr. Robert Leben at the University of Colorado (continued).

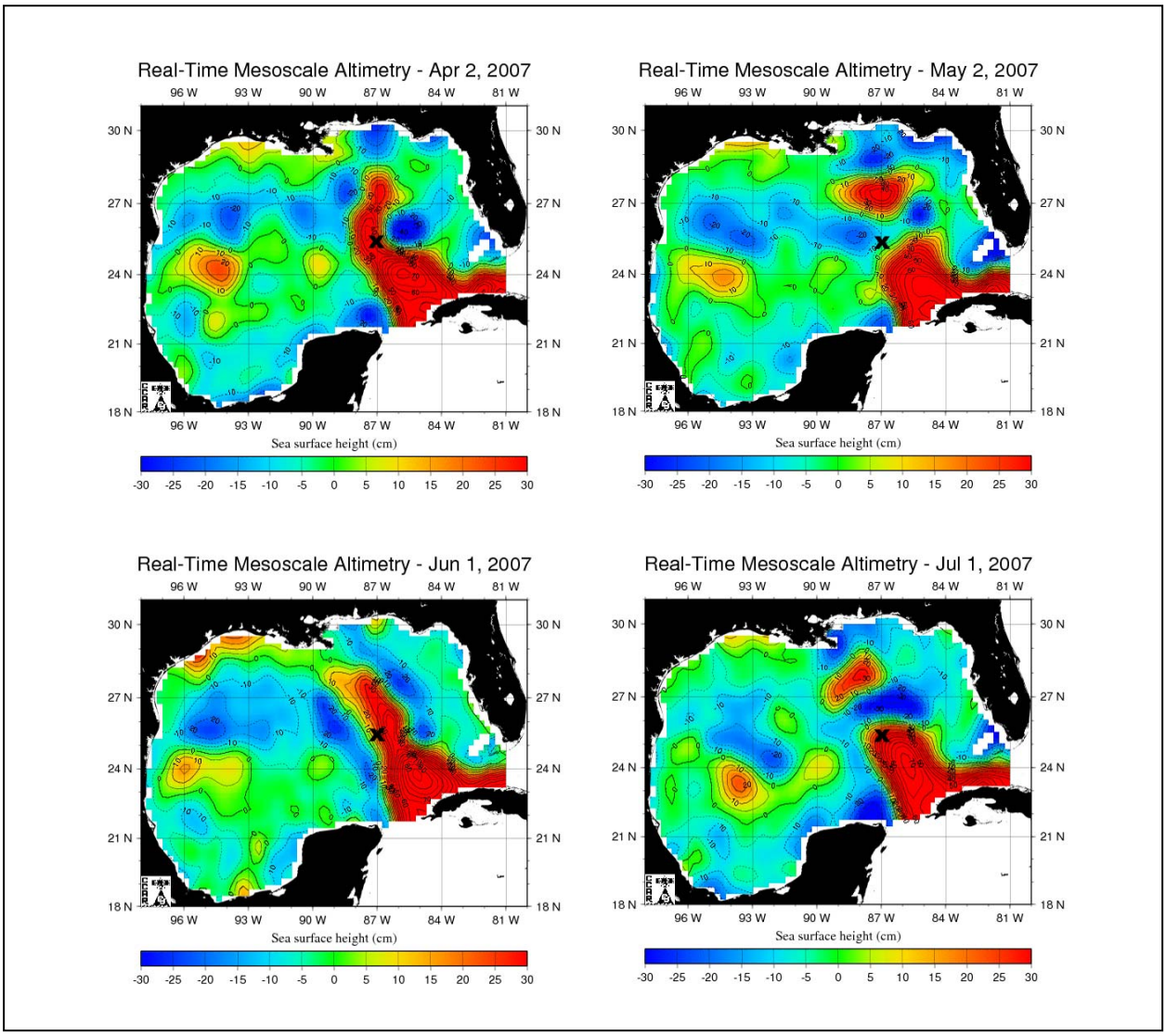

Figure B-1. Sea surface height maps for each month during Deployments 4 and 5 plotted from mesoscale altimetry data archived by Dr. Robert Leben at the University of Colorado (continued).

APPENDIX C

DEPLOYMENT 5 HIGH-SPEED CURRENT EVENT

During the 5th Deployment two floats broke lose from the mooring during March 2007 resulting in the detachment of the ADCP at 140 m, one Microcat at 142m, and a current meter at 250 m. The pressure sensor on current meter CM10258 was unreliable, which gave us misleading clues as to when and what caused the floats to break loose. CM10258 was located on the wire immediately above Microcat 1332A, which recorded a depth of ~350 m below the surface. Although CM10258 was slightly shallower, the pressure sensor fluctuated between 390 mb and 840 mb (387 m and 832 m, respectively) for the majority of the deployment before the floats broke free. From March 20 at 16:00 to March 25 at 03:00, CM10258 recorded pressures between 630 mb and 712 mb. Between 03:00 and 21:00 on March 25, CM10258 recorded pressures starting at 396 mb, dropping to 685 mb, and back up to 400 mb. None of the other instruments recorded these short term fluctuations in depth, including Microcat 1332, which was immediately below CM10258. There appears to have been a single catastrophic event that resulted in the loss of the instruments. This event occurred on March 25, 2007 between 20:00 and 21:00 hours as recorded by all of the instruments that were recovered.

The configuration of the mooring before and after the catastrophic event is illustrated in Figure C-1. The loss of the floats and instruments was likely due to wire fatigue in the upper portion of the mooring in response to a surge in the currents. A break in the wire appears to have occurred between 250 m and 350 m, which resulted in the loss of the uppermost float along with the ADCP and Microcat at 140 m. The small float at 450 m did not detach and as a result, the wire above it folded over so that the current meter (CM10258) and Microcat (1332A) at 350 m hung ~100m below the float. Current meter CM12701 was initially just below the small float at a depth of 451 m and another current meter, CM12701, was initially at 600 m. A large float was attached to the wire at 759 m. The float at 450 m was not buoyant enough to support the weight of the instruments initially above it (CM12058 and 1332A) and the instruments below it (CM12701 and CM12700). This entire group of instruments sunk below the large float at 750 m, causing another fold in the wire. The Microcat (2425A) that was initially just above the float at 750 m also dropped below 750 m when the wire folded over and came to rest about 7 m below its initial depth. The wire must have folded over twice resulting in the vertical distribution of instruments illustrated in Figure C-1. The large float at 750 m was buoyant enough to keep all of the instruments below it near their initial depths. All of the instruments above 1000 m most likely became entangled in the three sections of wire that were now overlapping and the data after the accident is not considered reliable.

As stated above, the true cause of the mooring accident is not known, but we do know enough about the currents at the time to speculate. The magnitude of the velocity for each of the top five current meters is shown in Figure C-2. Although the pressure sensor was malfunctioning on CM10258, we do not have any reason to suspect that there were any problems with the current direction or magnitude. Prior to March 20, the mooring was located in the center of an extended branch of the LC (Figure C-3). The currents were extremely slack over the entire mooring. Then on March 20, the current speed began to increase in the upper 750 m of the water column (Figure C-2). On March 23 the current speed picked up at 1500 m and later that

day, the speed began to increase at 2000 m. On March 25 between 20:00 hours and 21:00 hours, the speed at the upper three current meters dropped off precipitously. As discussed above, the depth of these three current meters and a Microcat also changed dramatically at this same time (Figure C-2), which explains the drastic decrease in current speed. The current meters at 1500 m and 2000 m appeared to be unaffected by the changes in the upper part of the mooring and continued to record the southward surge that extended through the entire water column. The currents at 1500 m and 2000 m peaked on April 1, which was accompanied by the maximum blow over of the mooring at these depths (Figure C-2). The degree of blow over of the mooring in the upper water column can not be determined, since several buoys broke loose and the cable folded over. The topmost instrument to survive the incident was the downward-looking ADCP at 740m, which experienced a blow over of 148 m. In the deep water the maximum blow over measured by the pressure sensor at 1500 m was nearly 125 m.

The extraordinarily strong southward flow was associated with a cyclonic eddy, which formed to the east of the LC, moved westward and became situated directly over the mooring location. The cyclone became visible in SSH images on March 20 and strengthened as it moved westward between March 25 and March 30 (Figure C-3). Strong southward currents persisted at the mooring until April 6, after which the current speed briefly decreased and then increased again along with a shift in the current direction toward the southwest. The magnitude of the geostrophic current can be estimated from maps of sea surface velocity from the Near Real Time Velocity Viewer for the Gulf of Mexico on the CCAR Near Real-Time Altimetry Data Homepage (http://argo.colorado.edu/~realtime/welcome) (Figure C-3). The peak geostrophic current speed was greater than 2.5 knots (1.3 m/s) during this event. The change in SSH along a segment connecting the SSH maximum associated with the LC to the SSH minimum in the cyclone was approximately 90 cm over a distance of ~90 nm (Figure C-4). Using the equation for geostrophic velocity, this change in SSH would result in a current of 84.5 cm/s. This extreme current event was corroborated by evidence from NDBC. Buoy 42408, located at 25.41N, 86.8W, was approximately 22 km from the Deep Sea Mooring and it went out of service on March 31, 2007.

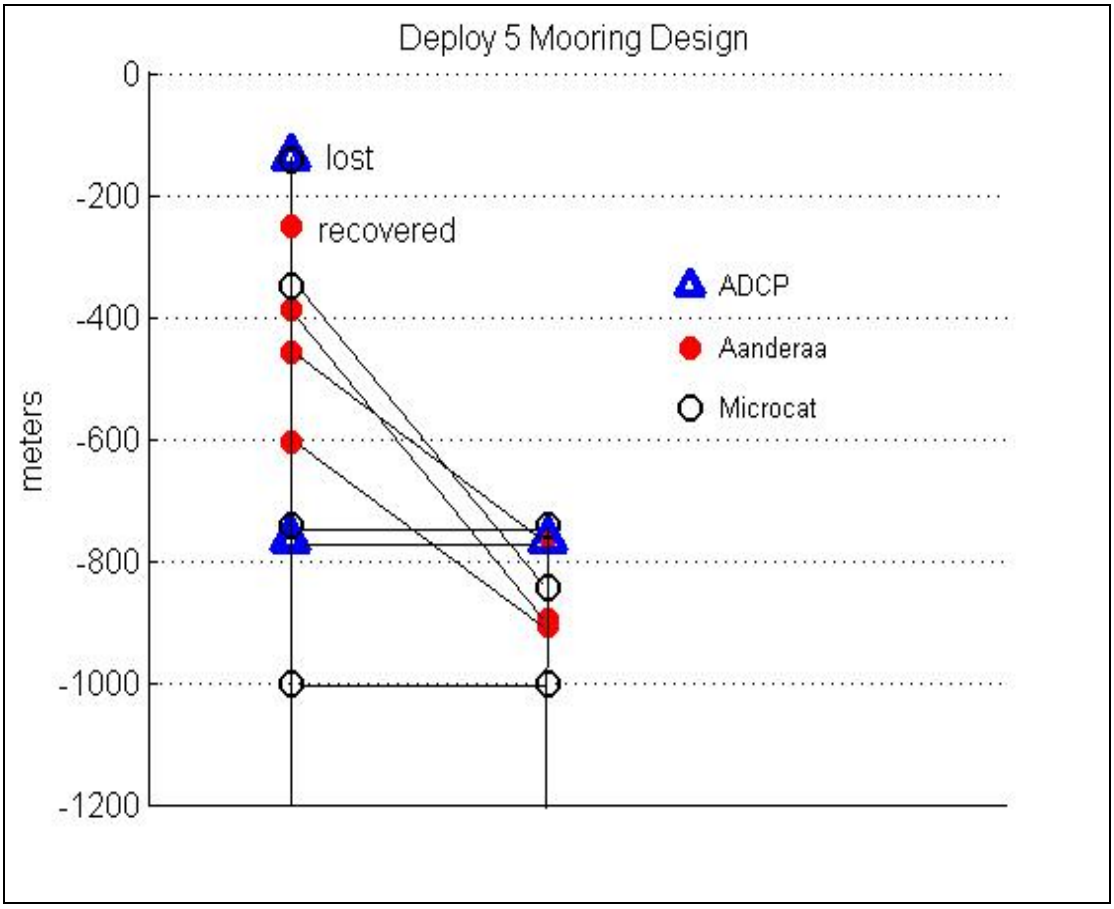

Figure C-1. Instrument depths on the deep-sea mooring before (left) and after (middle) the cable break.

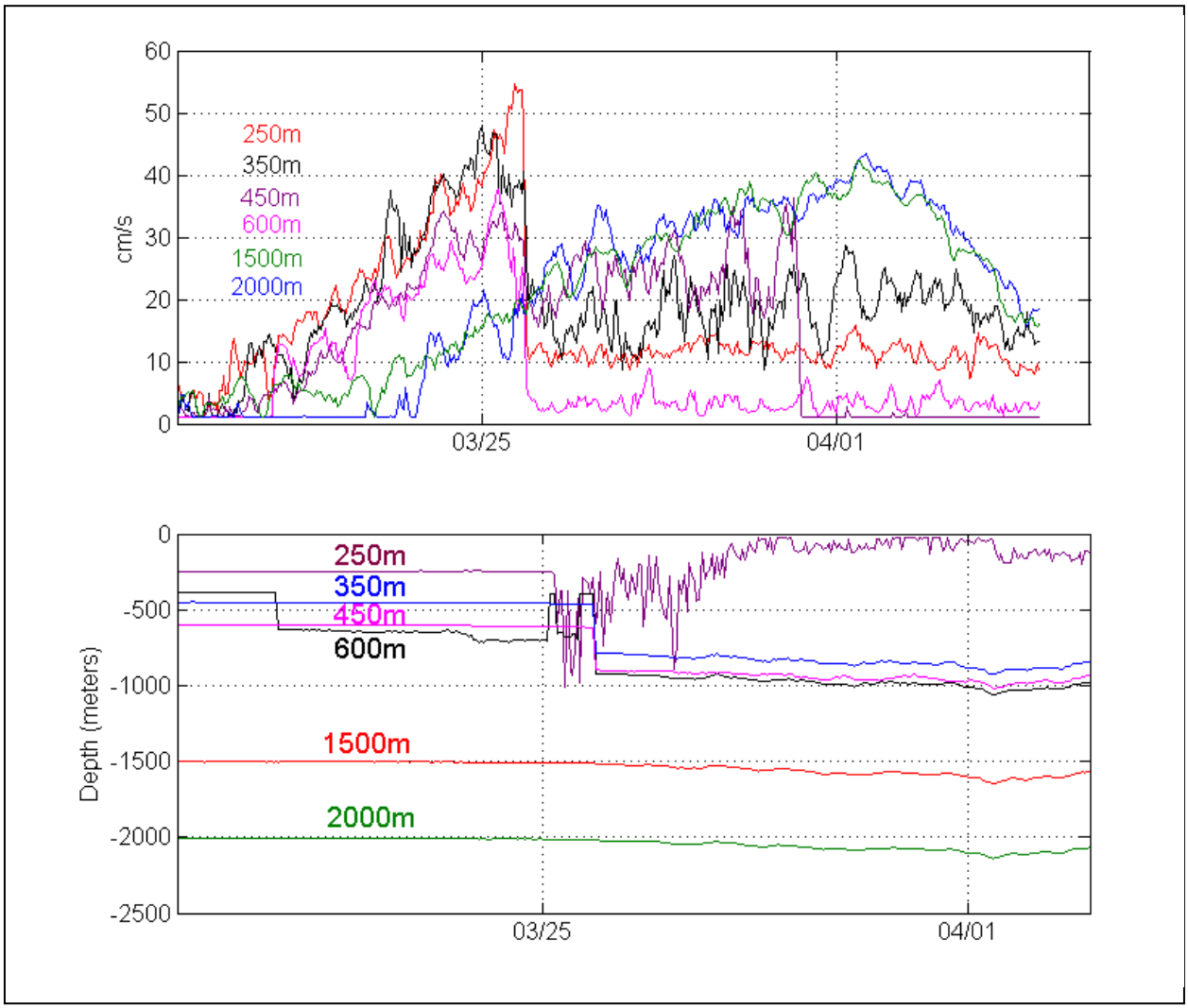

Figure C-2. Current speed (top) and depth (bottom) for the top 5 currents meters.

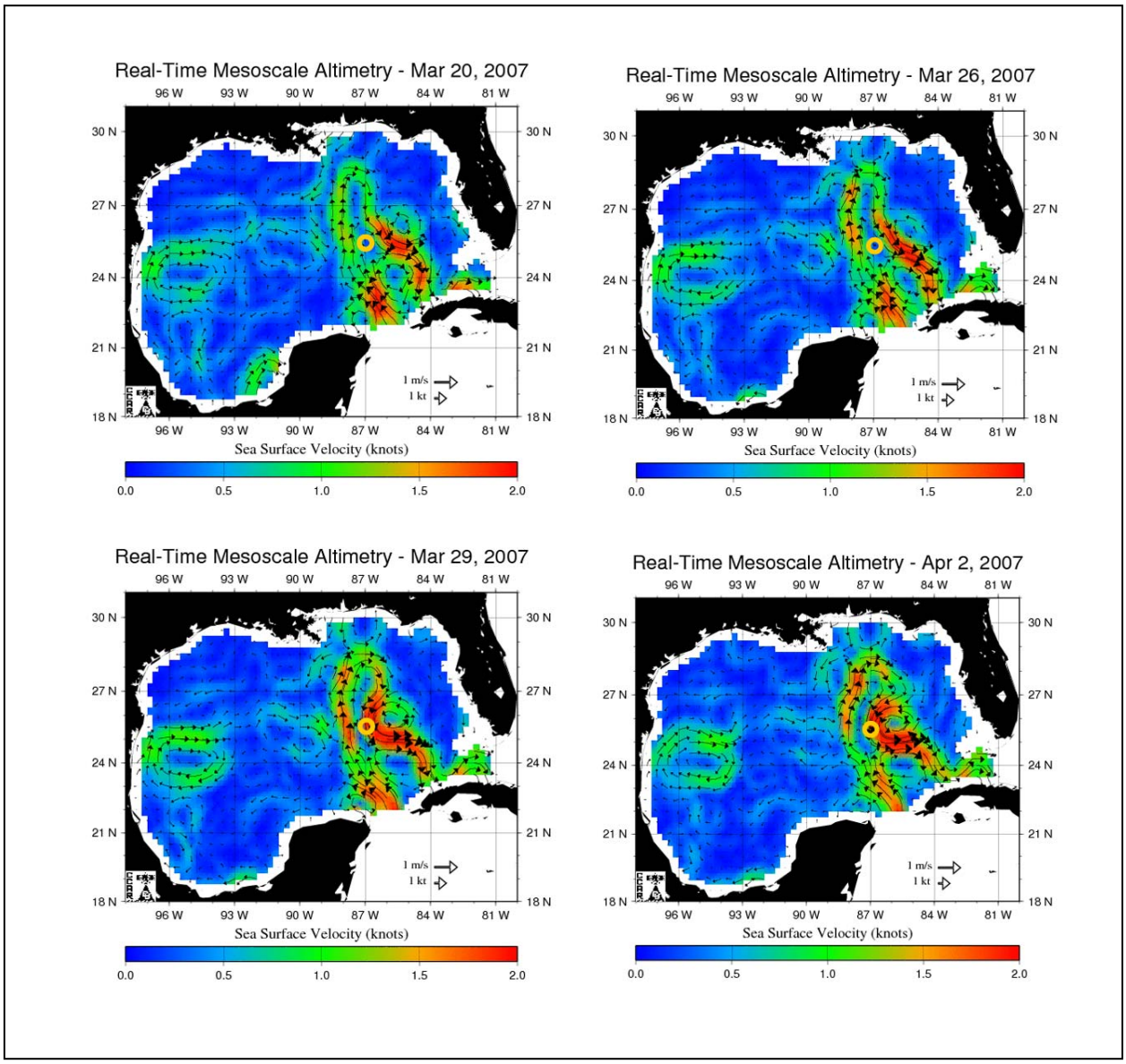

Figure C-3. Geostrophic velocity vectors from historical mesoscale altimetry data archived by Dr. Robert Leben at the University of Colorado. The mooring location is indicated by a yellow ‘o’.

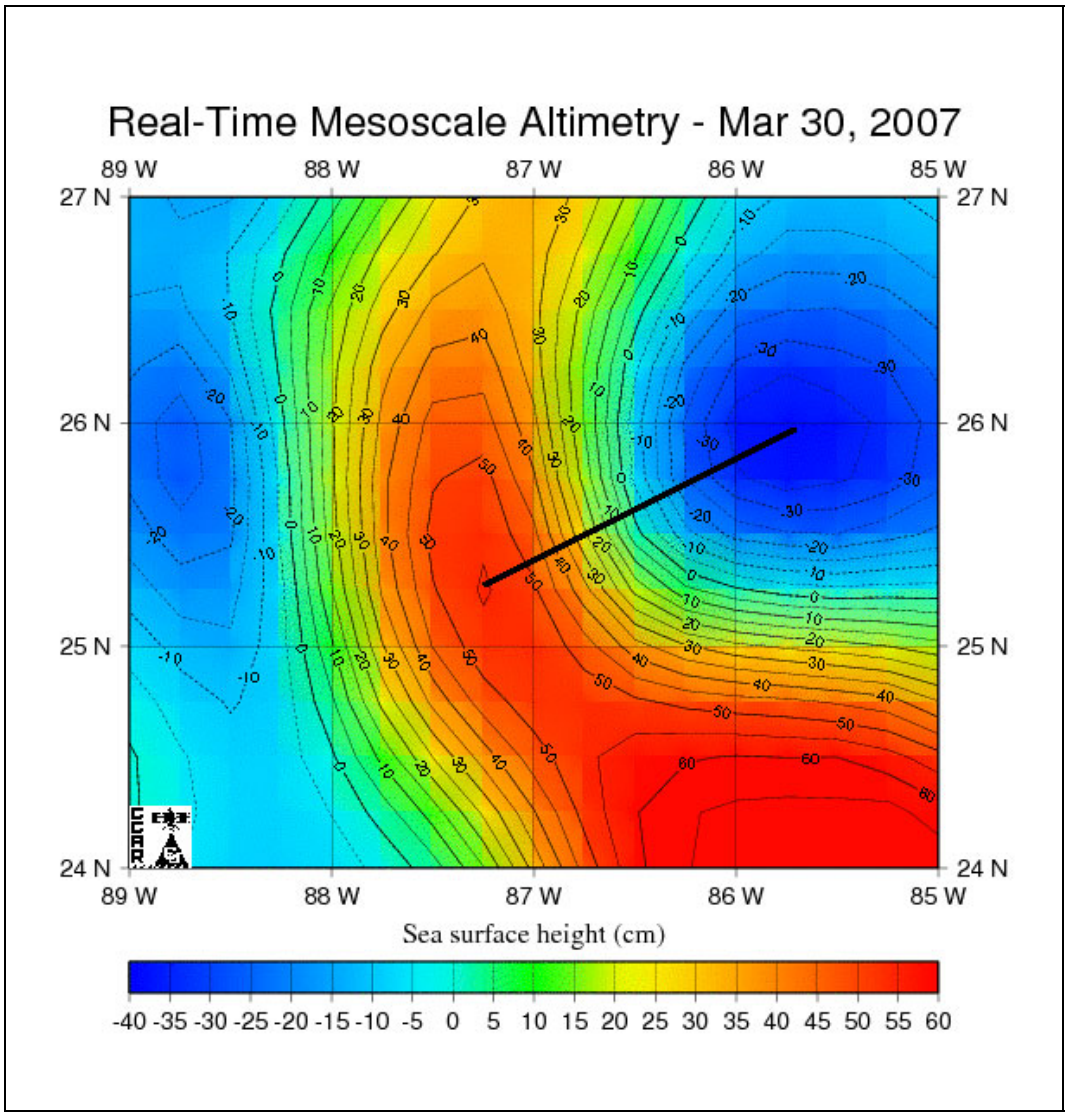

Figure C-4. Sea surface height (cm) from altimetry for March 30, 2007, replotted from historical mesoscale altimetry data archived by Dr. Robert Leben at the University of Colorado. The line connects the highest and lowest values of SSH.

The Department of the Interior Mission

As the Nation's principal conservation agency, the Department of the Interior has responsibility for most of our nationally owned public lands and natural resources. This includes fostering sound use of our land and water resources; protecting our fish, wildlife, and biological diversity; preserving the environmental and cultural values of our national parks and historical places; and providing for the enjoyment of life through outdoor recreation. The Department assesses our energy and mineral resources and works to ensure that their development is in the best interests of all our people by encouraging stewardship and citizen participation in their care. The Department also has a major responsibility for American Indian reservation communities and for people who live in island territories under U.S. administration.

The Minerals Management Service Mission

As a bureau of the Department of the Interior, the Minerals Management Service's (MMS) primary responsibilities are to manage the mineral resources located on the Nation's Outer Continental Shelf (OCS), collect revenue from the Federal OCS and onshore Federal and Indian lands, and distribute those revenues.

Moreover, in working to meet its responsibilities, the **Offshore Minerals Management Program** administers the OCS competitive leasing program and oversees the safe and environmentally sound exploration and production of our Nation's offshore natural gas, oil and other mineral resources. The MMS **Minerals Revenue Management** meets its responsibilities by ensuring the efficient, timely and accurate collection and disbursement of revenue from mineral leasing and production due to Indian tribes and allottees, States and the U.S. Treasury.

The MMS strives to fulfill its responsibilities through the general guiding principles of: (1) being responsive to the public's concerns and interests by maintaining a dialogue with all potentially affected parties and (2) carrying out its programs with an emphasis on working to enhance the quality of life for all Americans by lending MMS assistance and expertise to economic development and environmental protection.